EUROPEAN ORGANIZATION FOR NUCLEAR RESEARCH

CERN-EP/89-64
5 May 1989

ENERGY MEASUREMENT OF ELEMENTARY PARTICLES

C.W. Fabjan and R. Wigmans

CERN, Geneva, Switzerland

ABSTRACT

We review the techniques used to measure the energy of elementary particles. The methods discussed span more than 20 orders of magnitude in energy, ranging from a small fraction of an electronvolt, where relic remainders of the Big Bang are being looked for, to the $10^{\sim 20}$ eV domain, where the highest-energy cosmic rays can be found. The emphasis is, however, on techniques employed in particle physics for studying collision processes at accelerators in the GeV–TeV range.

(Submitted to Reports on Progress in Physics)

1. INTRODUCTION AND SCOPE OF THE REVIEW

Experimental particle physicists study the fundamental structure of matter with a variety of approaches, which may be subdivided in two classes: accelerator and non-accelerator experiments. Accelerator experiments have the advantage of well-controlled experimental circumstances, non-accelerator experiments offer the possibility of studying processes that are not accessible to the available accelerator technology.

Accurate energy measurements are a prime tool for increasing the knowledge of the constituents of matter, and the forces by which they interact. Three examples may illustrate this. The fundamental nature of the cosmic background radiation emerged when it was realized that the energy spectrum corresponded to that of a black body radiating at a temperature of 3K. On the high-energy side of the scale, the elementary particles are unstable; without exception, the known ones were discovered by a kinematical reconstruction from their decay products, the quality of which is closely linked to the accuracy of the particle energy measurement. And finally, the crucial question whether the neutrino rest mass is different from zero needs an extremely accurate comparison between energy and momentum in order to be answered.

The energy of elementary particles is measured with instruments that are generally called *calorimeters*. There is a wide variety of them. The principle is simple. Basically, a calorimeter is a block of matter in which the particle to be measured interacts and transforms (part of) its energy into a measurable quantity. The resulting signal may be electrical, optical, thermal or acoustical. It is of course important that the signal be proportional to the energy that one wants to measure, which is not always easy to achieve.

In this review, we will mainly concentrate on the calorimeters that are used in high-energy physics, i.e. on the detectors used for measuring particle energies in the GeV range and above. However, a short description will be given of emerging techniques employed in searching for low-energy fundamental particles, such as neutrinos and hypothetical species.

In high-energy physics, we have seen in the last 15 years a clear trend by which experiments changed from *electronic bubble chambers*, aiming for a precise measurement of the 4-vectors of all individual reaction products with spectrometric

methods, to configurations with increasing emphasis on calorimetric particle detection. Some major discoveries, e.g. the existence of the intermediate vector bosons W and Z, became possible as a result of this development.

The reasons why calorimeters have emerged as the key detectors in almost any experiment in particle physics, can be divided into two classes. Firstly, there are reasons related to the *calorimeter properties*:

a) Calorimeters are sensitive to both charged and neutral particles.

b) Owing to differences in the characteristic shower patterns, some crucial particle identification is possible.

c) Since calorimetry is based on statistical processes, the measurement accuracy *improves* with increasing energy, in contrast to what happens for other detectors.

d) The calorimeter dimensions needed to contain showers increase only logarithmically with the energy, so that even at the highest energies envisaged it is possible to work with rather compact instruments (cost!).

e) Calorimeters do not need a magnetic field for energy measurements.

f) They can be segmented to a high degree, which allows accurate measurements of the direction of the incoming particles.

g) They can be fast -response times better than 100 ns are achievable- which is important in a high-rate environment.

h) The energy information can be used to trigger on *interesting* events with very high selectivity.

Secondly, there are reasons related to the *physics* to be studied. Here, the emphasis has clearly shifted from track spectroscopy to measuring more global event characteristics, indicative for interesting processes at the constituent level. These characteristics include missing (transverse) energy, total transverse energy, jet production, multijet spectroscopy, etc. Calorimeters are extremely well suited for this purpose.

In this review, we have decided to discuss in considerable detail developments that took place during the last five years and to complement in this way earlier reviews[1,2] . In Section 2 we describe the various processes by which particles lose their energy when traversing dense matter and by which they eventually

get absorbed. We discuss shower-development phenomena, the effects of the electromagnetic and strong interactions, and the consequences of differences between these interactions for the calorimetric energy measurement of electrons and hadrons, respectively.

In Section 3, the performance of calorimeter systems is described. The section starts with a discussion of the so-called compensation mechanism, its relevance for the performance of hadron calorimeters, and the methods to achieve compensation in calorimeters. In a following subsection, the factors that determine and limit the energy resolution of different calorimetric detectors are discussed. The rest of the section describes in some detail the performance of existing and planned devices in terms of energy and position resolution, particle identification, and signal processing. The section is concluded with an overview of the most important calorimetric detectors currently, or about to be, employed.

Section 4 gives conclusions, and an outlook to further developments of this important experimental technique.

2. ABSORPTION MECHANISMS OF PARTICLES

When a particle traverses matter, it will generally interact and lose (a fraction of) its energy in doing so. The medium is excited in this process, or heated up, hence the word calorimeter. The interaction processes that play a role depend on the energy and the nature of the particle. They are the result of the electromagnetic, the strong and, more rarely, the weak forces reigning between the particle and the medium constituents. In this section, we will describe the various mechanisms by which particles may lose their energy and eventually be absorbed.

2.1 ELECTROMAGNETIC ABSORPTION

The best known energy-loss mechanism contributing to the absorption process is the electromagnetic (e.m.) interaction experienced by charged particles that traverse matter. The charged particles ionize the medium, if their energy is at least sufficient for releasing the atomic electrons from the e.m. nuclear field. This process forms also the principle on which many detectors are based, since the liberated electrons may be collected by means of an electric field, and yield an electric signal.

The e.m. interaction may manifest itself, however, in many other ways. Charged particles may excite atoms or molecules without ionizing them. The de-excitation from these metastable states may yield (scintillation) light, which is also fruitfully used as a source of calorimeter signals. Charged particles travelling faster than the speed of light characteristic for the traversed medium lose energy by emitting Čerenkov light. At high energies, knock-on electrons (δ-rays) and bremsstrahlung are produced, and even nuclear reactions induced by the e.m. interaction may occur.

The e.m. field quantum, the photon, is affected by three different processes. First, there is the photoelectric effect, in which the photon transfers all its energy to an atomic electron. In the Compton process, only part of the energy is transferred in this way. At energies larger than twice the electron rest mass, the photon may convert into an electron-positron pair. The relative importance of these three processes depends strongly on the photon energy and the electron density ($\sim Z$) of the medium.

Except at the lowest energies, the *absorption* of electrons and photons is a multistep process, in which particle multiplication may occur (*shower development*). This phenomenon, which leads to the absorption of high-energy particles in relatively small volumes, is extensively discussed in the next subsections. The other particles subject to only the e.m. interaction, the muons, do not show such behaviour up to very high energies (100 GeV). They lose their energy primarily through ionization and δ-rays. These mechanisms account for an energy loss of typically $1 - 2\,\mathrm{MeV}\,/\mathrm{g.cm}^{-2}$ and, therefore, it takes very substantial amounts of material to absorb high-energy muons (1 TeV muons may penetrate several kilometres of the Earth's crust).

2.1.1 The 0 to 10 MeV range

Already at fairly low energies, relatively simple showers may develop. Let us consider as an example the γ's of a few MeV characteristic of nuclear de-excitation. The sequence of processes through which γ's of a particular energy are absorbed may be very different from event to event. An example of such a sequence is given in fig. 1. A 3370 keV γ enters the detector and converts into an electron- positron pair. Both particles get a kinetic energy of 1174 keV (point A), the remaining energy is needed for the mass of the e^+ and e^-. The electron

loses its kinetic energy through ionization of the detector material and so does the positron. When the positron is stopped, it annihilates with an electron, thus releasing the energy $E = M_{e^+e^-}$ in the form of two γ's of 511 keV each (B). These γ's undergo Compton scattering (C,D), in which part of the energy is transferred to an electron and part to a new γ. The electrons lose their energy as described; the γ's may undergo either another Compton scattering (F), or photoelectric effect in which their full energy is transferred to an electron (E,G).

In this example, which is only one out of an infinite number of different possibilities, the energy of the original γ is absorbed through ionization of the detector medium by one positron and six different electrons. Events for which the whole sequence has taken place inside the sensitive volume of the detector will yield a signal peak at 3370 keV. In small detectors, leakage phenomena may occur (fig. 1). Either one or both 511 keV γ's may escape from the detector. This leads to peaks at energies lower by 511 and 1022 keV, respectively. And if *they* do not escape, some of the tertiary or higher-order γ's might, leading to a continuous background.

At these low energies, a modest role may also be played by photonuclear reactions, e.g. γn, γp or photo-induced nuclear fission. However, the cross-sections for these processes usually do not exceed 1% of the cross-sections for the processes mentioned before and may therefore, in general, be neglected.

2.1.2 From 10 MeV to 100 GeV

Most of the energy-loss mechanisms relevant to high-energy shower development were already mentioned in the previous subsection: Ionization for electrons and positrons, pair production, Compton scattering, and the photoelectric effect for photons. There is one more, be it crucial mechanism that contributes at higher energies: *bremsstrahlung.*

In their passage through matter, electrons and positrons may radiate photons as a result of the Coulomb interaction with the nuclear electric field. These photons have an exponentially falling energy spectrum that, in principle, extends to the electron energy, but in general the emitted photon carries only a small fraction of this energy. In this process, the electron itself undergoes a (usually small) change in direction (multiple or Coulomb scattering). The deviation depends on the angle and the energy of the emitted photon, which in turn depend on the

strength of the Coulomb field, i.e. on the Z of the absorber medium.

Bremsstrahlung is by far the principal source of energy loss by electrons and positrons at high energies. As a consequence, high-energy e.m. showers are quite different from the ones discussed in the previous subsection, since an important multiplication of shower particles occurs. A primary GeV-type electron may radiate on its way through the detector thousands of photons. The ones faster than 5-10 MeV will create e^+e^- pairs. The fast electrons and positrons from this process may in turn lose their energy by radiation as well, etc, etc. The result is a shower that may consist of thousands of different particles, electrons, positrons, and photons. The overwhelming majority of these particles is very soft. The *average* energy of the shower particles is obviously a function of the age of the shower, or the depth inside the detector: the further the shower has developed, the softer the spectrum of its constituents becomes.

The energy-loss mechanisms are governed by the laws of quantum electrodynamics (QED)[3] . They primarily depend on the electron density of the medium in which the shower develops. This density is roughly proportional to the (average) Z of the medium, since the number of atoms per unit volume is within a factor of ~ 2 the same for all materials in the solid state.

The results of calculations on the energy-loss mechanisms for photons and electrons are shown in fig. 2, as a function of energy, in three materials with very different Z-values: carbon ($Z = 6$), iron ($Z = 26$), and uranium ($Z = 92$)[4,5] . At high energies, above $\sim 100\,\mathrm{MeV}$, pair production by photons and energy loss by radiation dominate in all cases, but at low energies the differences between the various materials are considerable. Both the energy at which Compton scattering starts dominating pair production, and the energy at which ionization losses become more important than bremsstrahlung, are strongly material-dependent and are roughly inversely proportional to Z.

These conditions determine the so-called *critical energy* (ϵ_c), i.e. the point where no further particle multiplication occurs in the shower. Above this energy, γ's produce on average more than one charged particle (pair production), and electrons lose their energy predominantly by creating *new* γ's. Below ϵ_c, γ's produce only *one* electron each, and these electrons do not produce new γ's themselves.

Figure 2 also shows that the contribution of the photoelectric effect is extremely Z-dependent ($\sigma \sim Z^5$). In carbon, it plays a role only at energies below a few keV, while in uranium it is the dominating process below 0.7 MeV.

The approximate shape of the longitudinal shower profile can be deduced from figure 2. If the number of e^+ and e^- were to be measured as a function of depth in the detector, one would first find a rather steep rise due to the multiplication. This continues up to the depth at which the average particle energy equals ϵ_c. Beyond that point no further multiplication will take place and, since more and more electrons are stopped, the total number of remaining particles slowly decreases.

The positrons will predominantly be found in the early shower part, *i.e.* before the maximum is reached. Showers in high-Z materials will contain *more* positrons than in low-Z materials, because positron production continues until lower energies. The *average* energy of the shower particles is also lower in high-Z materials, since radiation losses dominate until lower energies. These effects will turn out to have interesting consequences.

Owing to the fact that the underlying physics is well understood and simple, e.m. shower development can be simulated in great detail by Monte Carlo techniques. One program, EGS4[6] has emerged as the world-wide standard for this purpose. It is extremely reliable, and in the following sections several results of it will be shown.

2.1.3 Above 100 GeV

At very high energies new effects will influence the absorption of electrons and photons in a block of matter. In the TeV region, the cross-sections for the e.m. and weak interactions become comparable and, therefore, processes involving hadron and/or neutrino production are no longer negligible.

Another, purely e.m. effect was first pointed out by Landau and Pomeranchuk[7] and treated quantitatively by Migdal[8] . They showed that at energies beyond 10 TeV, multiple scattering of the participating particles may lead to a significant decrease of the cross-sections for bremsstrahlung and pair production. Such effects will obviously change the gross behaviour of the shower development. The experimental information on these phenomena is scarce and, because of their limited practical relevance at present, we will not discuss them further.

2.1.4 Electromagnetic shower characteristics

Since the e.m shower development is primarily determined by the electron density in the absorber medium, it is to some extent possible, and in any case convenient to describe the shower characteristics in a material-independent way. The units that are frequently used to describe the characteristic shower dimensions are the *radiation length* (X_0) for the longitudinal development and the *Molière radius* (ρ_M) for the transverse development.

The radiation length is defined as the distance over which a high-energy (> 1 GeV) electron loses on average 63.2% ($1 - 1/e$) of its energy to Bremsstrahlung. The average distance that very high energy photons travel before converting into an e^+e^- pair equals $9/7\ X_0$. The Molière radius is defined by the ratio of X_0 and ϵ_c, where ϵ_c is the electron energy at which the losses through radiation and ionization are the same. For approximate calculations, the following relations hold:

$$X_0 \approx 180A/Z^2\ (\mathrm{g/cm^2}) \text{ and } \rho_M \approx 7A/Z\ (\mathrm{g/cm^2})\ .$$

Expressed in these quantities, the shower development is approximately material-independent. Figure 3 shows the longitudinal development of a 10 GeV electron shower in Al, Fe, and Pb, as obtained with EGS4 simulations. The profile is as expected from the discussion in section 2.1.2. Globally, it scales indeed with X_0. The differences between the various materials can be understood as well. The radiation length is defined for GeV-type particles and, therefore, does not take into account the peculiarities occurring in the MeV region. The shift of the shower maximum to greater depth for high-Z absorbers is a consequence of the fact that particle multiplication continues until lower energies; the slower decay beyond this maximum is due to the fact that lower-energy electrons still radiate.

The figure shows that it takes $\sim 25X_0$ to absorb at least 99% of the shower energy. This corresponds to 14 cm Pb, 44 cm Fe, or 220 cm Al. If the energy is increased, only very little *extra* material is needed to achieve the same containment. A 20 GeV photon will travel on average 9/7 radiation length before converting into an e^+e^- pair of 10 GeV each. It therefore takes only an extra $1.3\,X_0$ to contain twice as much energy.

The radiation length is, strictly speaking, defined for infinite energy and has no meaning in the MeV energy range. We just showed that ~ 15 cm lead absorb

20 GeV photon showers for more than 99%, whereas it takes *more* than that to make a proper shielding for a strong ^{60}Co source that emits 1.3 MeV γ's. The reason for this is clear from fig. 2 . The total cross-section around the region where Compton scattering takes over from pair production is considerably lower than at very high energies, particularly in high-Z materials. As a consequence, the mean free path in lead of photons of a few MeV is ~ 3 cm, or $\sim 5X_0$!

The *lateral spread* of an e.m. shower is caused by two effects:

a) Electrons move away from the axis by multiple scattering.

b) In the energy region where the total cross section is minimal, bremsstrahlung photons may travel quite far from the shower axis, in particular if they are emitted by electrons that themselves travel under a considerable angle with this axis.

The first process dominates in the early stages of the shower development, while the second process is predominant beyond the shower maximum, particularly in high-Z media. Figure 4 shows the lateral distribution of the energy deposited by an e.m. shower in lead, at various depths[9] . The two components can be clearly distinguished (note the logarithmic ordinate). The radial profile shows a pronounced central core surrouded by a *halo*. The central core disappears beyond the shower maximum. Similar calculations in aluminium showed that the radial profile, expressed in ρ_M units, is indeed narrower than in lead. Like the radiation length, also the Molière radius does not take into account the peculiarities occurring in the MeV region.

Figure 4 shows that e.m. showers are very narrow, especially in the first few radiation lengths. The Molière radius of lead is ~ 1.7 cm. With a sufficiently fine-grained calorimeter, the showering particle can therefore be localized with a precision of ~ 1 mm (see section 3.3).

2.1.5 Energy loss by muons

Muons passing through matter lose their energy also through e.m. processes. Compared to electrons, however, the cross-sections for higher-order QED processes, such as bremsstrahlung or e^+e^- pair production are suppressed by a factor of $(m_\mu/m_e)^2 \approx 40000$. The critical energy is, for example, at least 200 GeV. At energies below 100 GeV, the energy loss by muons will, therefore, be dominated by ionization processes.

The mean energy loss per unit path length for these processes, $< dE/dx >$, is given by the well-known Bethe-Bloch formula[10] . For relativistic muons, $< dE/dx >$ falls rapidly with increasing β, reaches a minimum value near $\beta = 0.96$ (minimum-ionizing particles), then undergoes what is called the relativistic rise, to level off at values of 2 - 3 MeV/g.cm^{-2} in most materials.

In practical calorimeters, the total energy loss $\Delta E/\Delta x$ may differ quite a bit from the value calculated from $< dE/dx >$. This is because of the relatively small number of collisions with atomic electrons, and of the very large fluctuations in energy transfer that may occur in such collisions. Therefore, the energy loss distribution will in general be peaked at values below the ones calculated from $< dE/dx >$ and have a long tail toward large energy losses, the so-called Landau tail[11] . Only for very substantial amounts of matter, at least 100 m of water equivalent, will the energy-loss distribution become approximately Gaussian.

Figure 5 shows some recent experimental results on muon energy loss, measured in the HELIOS calorimeter[12] , which consists essentially of $\sim$ 1 m of uranium. The figure clearly shows the asymmetric distribution of energy losses. It also shows that at increasing energies, and in particular at 200 GeV, higher-order QED processes such as bremsstrahlung start dominating over ionization losses, since the distribution of energy losses is shifted by a considerable amount to higher values.

2.2 STRONG-INTERACTION PROCESSES

The absorption of particles subject to the strong interaction (hadrons) in a block of matter proceeds in a way that is very similar, in many respects, to the one described for electromagnetically interacting particles, although in detail the particle-production mechanisms are substantially more complicated. When a high-energy hadron penetrates a block of matter, it will at some point interact with one of its nuclei. In this process, mesons are usually produced (π, K, etc.). Some other fraction of the initial particle energy is transferred to the nucleus. The excited nucleus will release this energy by emitting a certain number of nucleons and, at a later stage, low-energy γ's, and lose its kinetic (recoil) energy by ionization. The particles produced in this reaction (mesons, nucleons, γ's) may in turn lose their kinetic energy by ionization and/or induce new reactions, thus causing a shower to develop.

Some of the particles produced in this cascading process interact exclusively electromagnetically (e.g. π^0, η). Therefore, hadron showers contain in general a component that propagates electromagnetically. The fraction of the initial hadron energy converted into π^0's and η's may strongly vary from event to event, depending on the detailed processes occurring in the early phase of the shower development, i.e. the phase where production of these particles is energetically possible.

On average, approximately one third of the mesons produced in the first interaction will be π^0's. In the second generation of interactions, the remaining π^+, π^-, etc. may produce π^0's as well, if they are sufficiently energetic, and so on. And since production of π^0's by hadronically interacting mesons is an irreversible process, the average fraction of the initial hadron energy converted into π^0's increases (logarithmically) with the energy.

Although the shower development by hadrons and electrons shows many similarities, there exist some characteristic differences which turn out to have crucial consequences.

2.2.1 Shower dimensions

Firstly, the hadronic shower development is (for an important part) based on nuclear interactions and, therefore, the shower dimensions are governed by the *nuclear interaction length* λ_{int}. The nuclear interaction probability is determined by the fraction of a two-dimensional plane occupied by atomic nuclei; since the number of atoms per unit volume is to first order material-independent, λ_{int} will scale with the nuclear radius, i.e. as $A^{1/3}$.

Existing experimental data indicates that the longitudinal and lateral profiles of hadronic showers scale roughly with λ_{int}. Figure 6 shows the results of measurements that give a good impression of the longitudinal and lateral development of 300 GeV showers in uranium[13] . The profiles look very similar to e.m. showers (figs. 3,4), albeit on a very different scale. It takes about 80 cm of uranium to contain the 300 GeV π^- showers at the 95% level, while 10 cm would be sufficient for electrons at the same energy.

The leakage as a function of the detector depth is shown in fig. 7, for hadron energies ranging from 5 to 210 GeV. It turns out that the detector size needed

to contain, for instance, more than 99% of the shower energy, increases only very slightly with the energy, from $6\lambda_{int}$ at 5 GeV to $9\lambda_{int}$ at 210 GeV[14] .

One may use the differences in characteristic energy deposit for particle identification. Since λ_{int} scales with $A^{1/3}$ and X_0 with A/Z^2, the separation between electromagnetically interacting particles (e, γ, π^0) and hadrons works best for high-Z materials, where the ratio λ_{int}/X_0 may reach values larger than 30 (see section 3.4).

2.2.2 Invisible energy

A second crucial difference between the shower development by high-energy electrons and by hadrons concerns the fact that, in the latter case, a certain fraction of the energy is dissipated in undetectable (*invisible*) form. Apart from neutrinos and high-energy muons, which may be generated in the hadronic shower-development process and which will generally escape the detector, we refer mainly to the energy needed to release nucleons from the nuclear field that keeps them together. Some fraction of this nuclear binding energy loss may be recuperated when neutrons get captured by other nuclei. The protons, α's, and heavier nucleon aggregates released in nuclear reactions will, however, only lose their *kinetic energy*, by ionization.

The fraction of invisible energy can be quite substantial, up to 40% of the energy dissipated in non-e.m. form[15] .

At low energies (< 2 GeV) the probability that charged hadrons lose their kinetic energy *without* causing nuclear interactions, i.e. by ionization alone, increases rapidly. In this case, as for muons and e.m. showers, there are no invisible-energy losses. As a consequence, hadron calorimeters suffer in general from signal non-linearities at low energy[16] (see section 3.2).

2.2.3 Non-relativistic shower particles

A third difference, which has important consequences for the calorimetric energy measurement of elementary particles, results from the fact that a large fraction of the energy deposited in *hadronic* showers is carried by (extremely) non-relativistic particles, *i.e.* protons and neutrons. We mention three consequences:

i) Many protons produced in the shower-development process have a specific ionization $< dE/dx >$ that is 10 to 100 times the minimum-ionizing value, depending on the Z of the traversed medium. As a consequence, the fraction of the energy of such particles detected by sampling calorimeters consisting of alternating layers of absorber and active material that usually have very different Z-values, may be considerably different from the fraction detected for minimum-ionizing particles. This is illustrated in fig. 8 .

ii) Some frequently used active calorimeter media show a strongly non-linear behaviour in their response to densely ionizing particles. They suffer from saturation (scintillator)[17] or recombination effects (liquid argon[18] , room-temperature liquids[19]). Such effects may suppress the response, i.e. the signal per unit deposited energy, by as much as a factor 5 for this shower component[20] . These effects are much smaller, or absent, when gases or silicon are used as the active calorimeter medium.

iii) Neutrons, which lose their kinetic energy *exclusively* through strong interactions may travel quite long distances before being finally absorbed. In calorimeters where the neutrons contribute significantly to the signal, this may lead to a considerable prolongation of the pulse duration for hadronic signals, compared with e.m. ones. Typical time constants for the neutron contribution to the calorimeter signal amount to 10 ns for the release of kinetic energy, and 0.5 μs for the γ's created in the thermal-neutron capture process. These phenomena may be exploited for particle identification, and in particular for e/π separation (see section 3.4.1).

2.2.4 The role of neutrons

Regarding calorimetric applications, perhaps the most crucial difference between e.m. and hadronic shower development comes from the fact that a considerable fraction of the energy is carried by *non-ionizing* particles, i.e. the soft (few MeV) neutrons from the nuclear evaporation processes.

Since these neutrons lose their kinetic energy exclusively through collisions with atomic nuclei, their contribution to the signal of *sampling* calorimeters is completely dependent on the nuclear peculiarities of the materials composing the calorimeter. It is well-known that in particular hydrogen is very efficient in slowing down neutrons.

It was shown both experimentally[13] and theoretically[15,21,22] that in calorimeters with hydrogenous active material, the neutrons generated in the shower development may deposit a large fraction of their kinetic energy in the active layers, while charged particles are only sampled at the few per cent level. This effect is an important tool for making so-called *compensating* calorimeters.

3. PERFORMANCE OF CALORIMETER SYSTEMS

In this section, we will discuss the performance of calorimeters, these instrumented blocks of dense matter in which the particles interact and get absorbed through the processes described in the previous section, yielding signals from which the particle properties (energy, direction, type) can be derived.

Historically, one may distinguish between calorimeters, according to the purpose that they serve, as e.m. and hadronic shower detectors. Nowadays, there is a growing tendency to combine both functions in one instrument.

Another distinction that may be made concerns their composition: homogeneous, fully sensitive devices as opposed to sampling calorimeters. The latter consist of a passive absorber with active material embedded into it, most frequently in the form of a sandwiched layer structure. In this way only a small fraction of the initial particle energy, ranging from 10^{-5} for gas calorimeters to a few percent for solid or liquid readout media, is deposited in the active layers.

Although additional fluctuations, affecting the energy resolution, are caused by the fact that only a fraction of the energy is deposited in the active material, the sampling technique is becoming more and more popular, particularly in accelerator-based experiments, for the following reasons:

i) Since very dense absorber materials can be used, calorimeters can be made extremely compact. Even at the highest energies envisaged today, 2 m of lead or uranium is sufficient to contain all showers at the 99% level (see fig. 7).

ii) At increasing energies, the energy resolution tends to be dominated by *systematic* effects; therefore, the effects of sampling fluctuations become less important.

iii) Contrary to fully sensitive devices, sampling calorimeters can be made *compensating*.

Before discussing in detail actual devices, we will first elaborate on the latter point, which is crucial for the performance of hadron calorimeters.

3.1 COMPENSATION

3.1.1 The role of the e/h signal ratio

In a given calorimeter, hadron showers are detected with an energy resolution that is worse than for e.m. ones. This is mainly because, in hadronic showers, fluctuations occur in the fraction of the initial energy carried by ionizing particles. Losses in nuclear binding energy (see section 2.2.2) may consume up to 40% of the incident energy, with large fluctuations about this average.

As a consequence, the signal distribution for monoenergetic pions is wider than for electrons at the same energy, and has in general a smaller mean value ($e/\pi > 1$). The calorimeter response to the e.m. (e) and non-e.m. (h) components of hadron showers shows a similar difference ($e/h > 1$). Since the event-to-event fluctuations in the fraction of the energy spent on π^0 production (f_{em}) are large and non-Gaussian, and since $< f_{em} >$ increases (logarithmically) with energy, the following effects have to be expected if $e/h \neq 1$:

i) The signal distribution for monoenergetic hadrons is non-Gaussian.

ii) The fluctuations in f_{em} give an additional contribution to the energy resolution.

iii) The energy resolution σ/E does not improve as $E^{-1/2}$ with increasing energy.

iv) The calorimeter signal is *not* proportional to the hadron energy (non-linearity).

v) The measured e/π signal ratio is energy dependent.

Because of the latter effect, we prefer to use the energy-independent quantity e/h. In practice, the difference between e/h and e/π is small, and it vanishes at low energies and for e/h close to 1. All these effects have been experimentally observed[12,24,25] (fig. 9) and can be reproduced with a simple Monte Carlo.

At increasing energies, deviations from $e/h = 1$ (the *compensation condition*) rapidly become a dominating factor for the (lack of) calorimeter performance, e.g. for the energy resolution σ/E (fig. 9a). Signal non-linearities of $\sim 20\%$ over

one order of magnitude in energy have been observed, both in overcompensating ($e/h < 1$) and undercompensating ($e/h > 1$) calorimeters (fig. 9b). But perhaps the most disturbing drawback of a non-compensating calorimeter, especially in an environment where high trigger selectivity is required, is the non-Gaussian response (fig. 9c), which may cause severe problems if one wants for example to trigger on (missing) transverse energy: it will be very difficult to unfold a steeply falling E_T distribution and a non-Gaussian response function. Moreover, severe trigger biases are likely to occur: if $e/h < 1$ (> 1) one will predominantly select events that contain little (a lot of) e.m. energy from π^0's.

There is general agreement that hadron calorimeters for future applications at high energy should be compensating. It should be emphasized that other sources of experimental uncertainty, such as calibration errors, will produce effects similar to the ones caused by deviations from $e/h = 1$. Therefore, it is not necessary that e/h be exactly 1. It has been estimated[15] that $e/h = 1 \pm 0.05$ is adequate to achieve energy resolutions at the 1% level.

3.1.2 Methods to achieve compensation

Because of the invisible-energy phenomenon, *i.e.* the nuclear binding energy losses typical for (the non-e.m. part of) hadronic showers, one might naïvely expect the e/h signal ratio to be larger than 1 for all calorimeters. This is, however a tremendous oversimplification. Based on our present understanding of hadron calorimetry[15,21,22] , it may be expected that a large variety of very different structures can actually be made compensating. A wealth of available experimental data supports the framework of this understanding, and explicit predictions were experimentally confirmed.

The response of a sampling calorimeter to a showering particle is a complicated issue that depends on many details. This is particularly true for hadronic showers. It has become clear that showers can by no means be considered as a collection of minimum ionizing particles that distribute their energy to absorber and active layers according to $< dE/dx >$. The calorimeter signal is, to a very large extent, determined by very soft particles from the last stages of the shower development, simply because these particles are so numerous. Many observations support this statement.

Simulations of high-energy e.m. showers in lead or uranium sampling calorimeters show that about 40% of the energy is deposited through ionization by

electrons softer than 1 MeV[15] . Measurements of pion signals in fine-sampling lead/plastic-scintillator calorimeters revealed that there is almost no correlation between the particles contributing to the signal of consecutive active layers[26,27] This proves that the particles that dominate the signal travel on average only a very small fraction of a nuclear interaction length indeed.

For a correct evaluation of the e/h signal ratio of a given calorimeter, the last stages of the shower development must therefore be understood in detail, *i.e.* the processes at the nuclear and even the atomic level must be analysed. The particles that decisively determine the calorimeter response are *soft photons* in the case of e.m. showers, and *soft protons and neutrons* from nuclear reactions in non-e.m. showers. Since most of the protons contributing to the signal are highly non-relativistic, the saturation properties of the active material for densely ionizing particles are of crucial importance (see section 2.2.3).

There are many other factors that affect the signals from these shower components, and thus e/h. Among these, there are *material* properties, such as the Z values of the active and passive components, the hydrogen content of the active media (see section 2.2.4), the nuclear-level structure and the cross-section for thermal-neutron capture by the absorber; and there are the *detector* properties, such as the size, the signal integration time, the thickness of the active and passive layers, and the ratio of these thicknesses.

In order to achieve compensation, three different phenomena may be exploited:

i) The non-e.m. response may be selectively boosted by using depleted uranium (^{238}U) absorber plates. The fission processes induced in the non-e.m. part of the shower development yield extra energy, mainly in the form of soft γ's and neutrons[26] . This phenomenon also leads to the commonly used terminology, since the extra energy released in ^{238}U fission *compensates* for the nuclear binding energy losses.

ii) One may selectively suppress the e.m. response by making use of the peculiarities of the energy deposit by the soft-photon component of e.m. showers. Below 1 MeV, the photoelectric effect is an important energy loss mechanism. Since the cross-section is proportional to Z^5, soft photons will interact almost exclusively in the absorber layers of high-Z sampling calorimeters. They will only contribute to the signal if the interaction takes place sufficiently close to the boundary layer, so that the photoelectron can

escape into the active material. This effect may lead to a considerable suppression of the em response[15] . It may be enhanced by shielding the active layers by thin sheets of passive low-Z material[20,23,28,29] .

iii) The most important handle on e/h is provided by the neutron response, in particular for calorimeters with hydrogenous active material (see section 2.2.4). In this case, the fraction of the neutron's kinetic energy transferred to recoil protons in the active layers varies much more slowly with the relative amounts of passive and active material than does the fraction of the energy deposited by charged particles. Therefore, the relative contribution of neutrons to the calorimeter signal, and hence e/h, can be varied by changing the sampling fraction[15,21] . A small sampling fraction enhances the relative contribution of neutrons. It is estimated that in compensated lead- or uranium-scintillator calorimeters, neutrons make up $\sim 40\%$ of the non-e.m. signal, on average[22,23] . The lever arm on e/h provided by this mechanism may be considerable. It depends on the energy fraction carried by soft neutrons (favouring high-Z absorbers), on the hydrogen fraction in the active medium, and on the signal saturation for densely ionizing particles.

Apart from these methods, which aim at achieving $e/h = 1$ as an *intrinsic* detector property, a completely different approach has been applied, in order to reduce the mentioned disadvantages of an intrinsically non-compensating detector by means of off-line corrections to the measured data[24,30] . In this approach, which requires a very fine-grained detector, one tries to determine the π^0 content on a shower-by-shower basis, and a weighting scheme is used to correct for the different calorimeter responses to the π^0 and non-π^0 shower components.

An example of the results of calculations on e/h for uranium calorimeters is shown in fig. 10[15] . For hydrogenous readout materials (plastic scintillator, warm liquids) the e/h value sensitively depends on the relative amount of active material, and in any case configurations can be found with $e/h = 1$.

Experimental results clearly confirm the tendency predicted for plastic scintillator readout[12,25,31] . For non-hydrogenous readout, mechanism *iii)* does not apply. Here the neutron response, and hence the e/h ratio, can be affected through the signal integration time, taking more or less advantage of the considerable energy released in the form of γ's when thermal neutrons are captured

by nuclei, a process that occurs at a time scale of 1 μs. Experimental results obtained so far seem to confirm the prediction that it will be hard to achieve *full* compensation with liquid-argon (LAr) readout[32,33,34] . In U/Si detectors, a full exploitation of mechanisms *i)* and *ii)* might yield a compensating calorimeter, since there are no saturation effects[20,28,29] . Detectors with gaseous readout media offer a convenient way to tune e/h to the desired value, i.e. through the hydrogen content of the gas mixture. This has been demonstrated experimentally by the L3 Collaboration[35] .

The curves for TMP calorimeters given in fig. 10 are based on the assumption that the signal saturation in this liquid is equal either to LAr or to PMMA plastic scintillator. Preliminary experimental data indicate that the signal suppression in warm liquids is considerably larger, and that it depends, perhaps, on the electric-field strength and on the particle's angle with the field vector[36] . Figure 11 shows how sensitively the e/h signal ratio depends on the saturation properties. The UA1 Collaboration recently reported having measured an e/h value smaller than 1.1 with their first uranium-TMP calorimeter module[37] .

In summary, compensation is *not* a phenomenon restricted to uranium calorimeters, nor is the use of uranium absorber a guarantee for achieving compensation. It has become clear that both the readout medium and the absorber material determine the e/h value. Compensation is easier to achieve with high-Z absorbers because of the large neutron production and the correspondingly large leverage on e/h. But even materials as light as iron allow compensation, if used in combination with, for instance, plastic scintillator, albeit with impractically thick absorber plates[15] .

The neutron production in lead is considerably smaller than in uranium. In order to bring e/h to 1.0 for lead/scintillator detectors, the neutron signal has therefore to be more enhanced relative to charged particles than for uranium/scintillator calorimeters. As a consequence, the optimal sampling fraction is smaller for lead. The calculations[15] predicted e/h to become 1.0 for lead plates about 4 times as thick as the scintillator, while for uranium plates a thickness ratio of 1:1 is optimal. This prediction was experimentally confirmed by the ZEUS Collaboration[38] . They found $e/h = 1.05 \pm 0.04$, a hadronic energy resolution scaling with $E^{-1/2}$ over the energy range 3 - 75 GeV, and no deviations from a Gaussian line shape.

The mechanisms described above,which make compensating calorimeters possible, only apply to *sampling* calorimeters. They are based on the fact that only a small fraction of the shower energy is deposited in the active part of the calorimeter; thus, by carefully choosing the parameter values, one may equalize the response to the e.m. and non-e.m. shower components. This does *not* work for *homogeneous* devices, where, in the non-e.m. shower part, losses will inevitably occur that cannot be compensated for. Measurements performed so far with homogeneous hadron detectors support this conclusion, for what concerns the e/h ratio[39] , as well as the resulting non-linearity, the non-Gaussian response, and the poor energy resolution[40] .

3.2 ENERGY RESPONSE AND RESOLUTION

3.2.1 Fluctuations in the energy measurement

The detection of particle showers with calorimeters is based on *statistical* processes: the production of ionization charge, scintillation or Čerenkov photons, phonons, or electron-hole pairs in semiconductors. The energy resolution for particle detection is therefore determined, among other factors, by fluctuations in the number of primary, uncorrelated processes n. The width of the signal distribution σ_S for detection of monoenergetic particles with energy E will therefore relate to n as $\sigma_S/S \sim \sqrt{n}/n$, which leads for linear calorimeters to the familiar relation $\sigma_E/E = c/\sqrt{E}$.

It has become customary to give a value of c for expressing calorimetric energy resolutions, where E is given in units of GeV. Because of the statistical nature of calorimetry, the relative energy accuracy σ_E/E *improves* with increasing energy. This very attractive feature is one of the reasons why these instruments have become so popular.

Fluctuations in the number of primary processes constituting the calorimeter signal form the ultimate limit for the energy resolution. In most detectors, the energy resolution is dominated by other factors. We mention two exceptions. Firstly, there are the semiconductor nuclear-γ detectors, such as Ge, Ge(Li), and Si(Li) crystals. It takes very little energy to create one electron-hole pair in these crystals, only 2.9 eV in Ge. The signal of a 1 MeV γ fully absorbed in the detector will therefore consist of some 350,000 electrons. The fluctuations in this number lead to an energy resolution of $\sigma_E/E = 0.17\%$ (at 1 MeV!).

Owing to correlations in the production of consecutive electron-hole pairs (the so-called Fano factor), the limit of the energy resolution given by fluctuations in the number of primary processes will be somewhat larger. In practice, resolutions of $\sim$ 2.0 keV at 1 MeV are indeed achieved with such detectors.

A second example are lead-glass e.m. shower counters. They are based on the detection of the Čerenkov light produced by the electrons and positrons from the shower. Particles travelling at a velocity lower than the velocity of light in the absorber will *not* emit this light, and therefore the lead-glass is only sensitive to electrons with a kinetic energy larger than $\sim$ 0.7 MeV. This means that at maximum only $1000/0.7 \sim 1400$ particles can produce Čerenkov light, per GeV of shower energy, and that the resolution σ_E/E cannot become better than $\sim$ 3% at 1 GeV because of fluctuations in this number. The best lead-glass detector systems have reached $\sigma_E/E \approx 5\%$ for e.m. showers in the 1 - 20 GeV energy range[41] .

More frequently, the energy resolution is determined by factors *other* than the fluctuations in the number of primary processes. These factors may concern statistical processes with a Gaussian probability distribution, or be of a different nature. In the latter case, their contribution to the energy resolution will cause deviations from the $E^{-1/2}$ scaling law. Such deviations are of course most apparent at high energies.

As an example, we mention homogeneous scintillation counters(e.g. NaI(Tl), CsI, BGO). Compared to what happens with the semiconductor crystals discussed before, the following complications arise:

i) The scintillation photons are not monoenergetic.

ii) Only a fraction of the photons reach the light-detecting element. The rest is either absorbed or refracted. These effects strongly depend on the detector geometry and on the position where the light is produced.

iii) The sensitivity of photocathodes or photodiodes depends on the wavelength.

Measurements with NaI(Tl) crystals on 8 keV X-rays yielded $\sigma_E/E \approx 15\%$. If we assume that this result is dominated by fluctuations in the primary processes, this means that on average $\sim$ 40 photoelectrons are observed. Based on this result, one would then expect resolutions of $\sigma_E/E \approx 1.5\%$ at 1 MeV. Yet, the best

resolutions obtained at this energy are only about 5%. For e.m. shower detection one finds resolutions $\sigma_E/E \approx 1\%$ at 1 GeV, while a factor 30 improvement should be expected when extrapolating the 1 MeV results with the $E^{-1/2}$ scaling law. For this reason, it is incorrect to express resolutions as $c/\sqrt{E}$ for such detectors.

Other factors which will cause deviations from $E^{-1/2}$ scaling are instrumental: noise and pedestal contributions to the signal, uncertainties coming from calibration and non-uniformities, or incomplete shower containment.

The energy resolution of *sampling* calorimeters is frequently dominated by the very fact that the shower is sampled[42] . The nature of these sampling fluctuations is purely statistical and, therefore, they contribute as $c/\sqrt{E}$ to the final energy resolution. A major contribution comes from fluctuations in the *number* of *different* shower particles contributing to the calorimeter signal. In some devices (e.g. gas or Si readout), also the fluctuations in the energy that the individual shower particles deposit in the active calorimeter layers have to be taken into account. In calorimeters with *dense* active material (plastic scintillator, LAr), the contribution of sampling fluctuations to the energy resolution tends to scale as $\sigma_{samp}/E = \sqrt{t_{abs}/E}$, for a particular combination of passive and active material, a fixed thickness of the active planes and a thickness t_{abs} of the passive planes. The sampling fluctuations depend also on the thickness t_{act} of the active planes. Photon conversions in these planes contribute a term which scales like $c\sqrt{1/t_{act}}$, for fixed t_{abs} [16] . The relative contribution of this term depends on the Z values of the active and passive calorimeter layers. For Fe/LAr, one finds that σ_{samp}/E scales approximately like $t_{act}^{-1/4}$, for fixed t_{abs}.

When detecting electrons and hadrons with the same calorimeter, sampling fluctuations for the latter particles are considerably larger. First of all, the number of *different* shower particles contributing to the hadronic signal is smaller, because

i) Individual shower particles may traverse many planes.

ii) The average energy deposited by individual particles in the active layers is larger (soft protons!)

Moreover, the spread in the dE/dx loss of individual shower particles in the active layers is much larger.

The contribution of sampling fluctuations to the energy resolution can be measured in a straightforward way, by comparing energy resolutions measured with different fractions of the active calorimeter channels[26,27] .

In hadronic shower detection, two additional sources of fluctuation play a role, which have no equivalent for e.m. calorimeters, and which tend to dominate the energy resolution of practically all hadron calorimeters constructed up to now. Firstly, there are the effects of the non-Gaussian fluctuations in the π^0 shower component (section 3.1.1); these contribute a constant term to the energy resolution, which only vanishes for compensating detector structures.

Secondly, there are *intrinsic* fluctuations, in the fraction of the initial energy that is transformed into ionizing shower particles (the *visible* energy, see section 2.2.2). These form the ultimate limit for the energy resolution achievable with hadron calorimeters. In general one may therefore write (ignoring instrumental contributions such as shower leakage, calibration, etc.)

$$\sigma_{had}/E \;=\; \sqrt{\frac{c_{int}^2 + c_{samp}^2}{E}} \;+\; a$$

This formula shows that at high energy one will want to have a as small as possible (compensation); moreover, it is useless to make the sampling much finer than the limit set by the intrinsic fluctuations.

It turns out that calorimeters with hydrogenous readout are not only advantageous for achieving compensation: they may also yield considerably lower values for c_{int} than other detectors[15] . The intrinsic resolution is largely dominated by fluctuations in the nuclear binding energy losses. Since most of the released nucleons are neutrons in the case of high-Z target material, there is a correlation between this invisible energy and the kinetic energy carried away by neutrons. Efficient neutron detection therefore *reduces* the effect of the intrinsic fluctuations on the energy resolution.

Recently, the ZEUS Collaboration measured the intrinsic-resolution limit for compensating uranium- and lead-scintillator calorimeters to be $19\%/\sqrt{E}$ and $11\%/\sqrt{E}$, respectively[27] . This difference, which means that in principle better energy resolutions can be achieved with lead calorimeters than with uranium ones, can be explained as follows[43] . The extent to which the mechanism described above works depends on the *degree* of correlation between the nuclear

binding energy losses and the kinetic neutron energy. This correlation is expected to be better in lead than in uranium, since in the latter case many of the neutrons come from fission processes. These fission neutrons are less strongly correlated to the nuclear binding energy losses.

3.2.2 Performance of electromagnetic calorimeters

The best energy resolutions for e.m. shower detection are obtained with homogeneously sensitive detectors and they remain the method of choice when ultimate performance is needed. While detectors based on NaI(Tl) have been in use for decades, delivering consistently energy resolutions of $\sigma/E \sim 0.02E^{-1/4}$ [44] there are several recent developments providing alternative, sometimes even superior, performance characteristics. Particularly noteworthy are

i) The use of CsI(Tl), which offers similar performance but better mechanical properties compared with NaI(Tl)[45] .

ii) The use of BGO, which allows the construction of very compact detectors due to its short radiation length[46] .

iii) The use of BaF_2 crystals, which have a very fast (rise-time $\approx$ 500 ps) ultraviolet scintillation light component, and promise very high rate capability and good radiation resistance[47,48,49,50] .

iv) Studies on homogeneously sensitive noble-liquid (Ar, Kr, Xe) e.m. calorimeters[51,52,53,54,55] , which are evaluated to provide energy resolution in the NaI-range combined with ultimate radiation hardness.

When σ/E drops below 1%, the resolution tends to become dominated by systematic effects such as calibration uncertainties. This is generally true for all calorimeters.

The energy resolution reported for lead-glass e.m. shower counters varies between $5\%/\sqrt{E}$ [41] and $12\%/\sqrt{E}$, depending among others on the shower containment.

Achieving a sufficient degree of shower containment is usually no problem for the much cheaper sampling calorimeters. With calorimeters based on plastic-scintillator or LAr readout, energy resolutions are usually found to be in the range from $7\%/\sqrt{E}$ [56] to $\sim 20\%/\sqrt{E}$. With gaseous readout media the energy resolution is usually worse, because of the additional effects of fluctuations in the

energy that individual shower particles deposit in the active layers (path length, Landau fluctuations).

A very fine shower sampling can be obtained when scintillating plastic fibres are used as the active material. Energy resolutions as low as $8\%/\sqrt{E}$ (for 0.5 mm thick fibres) have been achieved with this technique[57] .

Signal *linearity* is usually no problem for e.m. shower detection. Only calorimeters with gas gain readout operating in a digital mode (streamer, Geiger) may suffer from non-linearities at high energy, because of the increased density of particles in the core of the shower, leading to a saturation in the gas gain.

3.2.3 Performance of hadron calorimeters

As pointed out in section 3.1.1, the energy resolution σ/E does in general *not* scale as $E^{-1/2}$ for hadron calorimeters. Only for devices with e/h sufficiently close to 1.0 is such scaling observed down to values of $\sigma/E \sim 1\% - 2\%$, where instrumental effects start dominating the results.

The energy resolution of *homogeneous* detectors is dominated by their non-compensating nature. The value of σ/E does not improve below $\sim 10\%$, even at energies as high as 150 GeV[39,40] .

Most *sampling* calorimeters currently employed as hadron detectors use iron as the absorber material, with active layers consisting of plastic scintillator, LAr, or wire chambers. None of these detectors has achieved energy resolutions better than $55\%/\sqrt{E}$ (at 10 GeV), while rapid deviations of $E^{-1/2}$ scaling occur at higher energies.

Efforts to determine the π^0 content on a shower-by-shower basis and to correct the signal by means of a weighting scheme[24] did result in a restoration of the $E^{-1/2}$ scaling for detection of single pions of known energy; these weigthing algorithms may, however, introduce signal non-linearities, and doubts remain about the applicability of such a scheme for detecting jets of unknown composition and energy[23,30] .

With compensating calorimeters, considerably better energy resolutions have been obtained. For uranium/plastic-scintillator detectors, values of $\sim 35\%/\sqrt{E}$ were reported by the HELIOS[12] and ZEUS Collaborations[31] , scaling with $E^{-1/2}$ up to $\sim$ 200 GeV. ZEUS also measured $44\%/\sqrt{E}$ for a compensating Pb/plastic-scintillator sandwich detector (10 mm Pb/2.5 mm scintillator)[38] . Because of the dominating contribution of sampling fluctuations to the latter result, val-

ues of $30\%/\sqrt{E}$ or better may be expected for the fine-sampling compensating Pb/scintillating-fibre detector that is being developed at CERN[43] .

The overcompensating U/scintillator calorimeter built by WA78 showed an energy resolution behaviour similar to the one measured for the undercompensating iron calorimeters mentioned before: $\sigma/E \sim 52\%/\sqrt{E}$ at 10 GeV, rapidly degrading at higher energies[25] .

The deviations from the $E^{-1/2}$ scaling are less dramatic in U/LAr calorimeters, which have e/h values closer to 1. The energy resolution obtained by D0 amounts to about $60\%/\sqrt{E}$ at 10 GeV[32] ; SLD found a similar value in their initial prototype studies[33] . HELIOS have recently found resolutions around $45\%/\sqrt{E}$[34] .

First results obtained with the new UA1 uranium-TMP calorimeter modules show an energy resolution for pion detection of $45.7\%/\sqrt{E} + 7\%$[37] .

The best absolute values for σ/E were reported by HELIOS, 1.9% for 3.2 TeV ^{16}O ions[12] , 1.0% for 6.4 TeV ^{32}S ions[34] . Figure 12 shows the results of calorimetric measurements on the 3.2 TeV ^{16}O beam from the CERN SPS, dumped in their U/plastic-scintillator calorimeter. The good energy resolution allows a detailed study of the spectrum of the contaminating lower-mass ions.

The effects of non-compensation on the *signal linearity* were already discussed in section 3.1.1 and experimental results were shown in fig. 9b. Signal non-linearities of $\sim 20\%$ over one order of magnitude in hadron energy are commonplace in non-compensating calorimeters like the WA1 and WA78 ones shown in this figure.

The weighting procedure mentioned before did *not* eliminate these non-linearities, particularly below $\sim$ 30 GeV. Therefore, a jet composed of 10 particles of 10 GeV will yield a signal that is considerably different from a 100 GeV pion signal and the resolution improvement is likely to be considerably smaller for jet detection.

At low energies, below $\sim$ 2 GeV, a different kind of non-linearity occurs, also for compensating calorimeters. At these low energies, charged hadrons may lose their energy *without* undergoing strong interactions and the corresponding nuclear binding energy losses. In that case, they deposit their energy through ionization alone, like muons. The hadronic response h will go up, and the e/h ratio down. The response to hadrons thus *increases* at low energies. This is

clearly confirmed by experimental data. Figure 13 shows the measured e/π signal ratio as a function of energy, for various calorimeter configurations. A clear decrease in this ratio, i.e. an *increase* in the hadronic response, is observed below ~ 2 GeV.

3.3 POSITION AND ANGULAR RESOLUTION

The position and the angle of incidence of particles can be obtained with calorimeters, using measurements of the transverse and longitudinal shower distribution.

The localization of e.m. (σ_x^e) and hadronic (σ_x^h) showers is derived from the center of gravity of the transverse distributions, which are narrowest in the early part, before the shower maximum. Given adequate transverse granularity, the resolution σ_x^e or σ_x^h is determined by the signal/noise ratio and, therefore, improves with increasing particle energy E, approximately as $E^{-1/2}$.

In the narrow early part, more than 90% of an e.m. shower is contained in a cylinder of radius $r \approx 0.5X_0$ and hence millimetre accuracies for σ_x^e are readily obtained, even with rather coarse (*i.e.* few $X_0\times$ few X_0) granularity. As an example, mm-resolution is quoted for few-GeV showers in a lead-glass array of 3.5×3.5 cm^2 granularity[58] , reaching submillimeter accuracy for 100 GeV showers[59,60] . Even higher spatial resolutions are obtained if a high-resolution detector, such as a Multiwire Proportional Chamber[61] or a Si-strip array[62] , is inserted into the calorimeter at a depth of $\sim 5X_0$. With such techniques, the position of a 100 GeV e.m. shower may be measured with an accuracy of ~ 100 μm!

Similar considerations apply to the localization of hadronic showers, which consist of a very narrow core surrounded by a *halo* of particles extending to several times the core diameter[13,63,64] (fig. 6). Measurements of the spatial resolution of the impact point[12,31,65,66] may be parameterized in the form

$$\sigma_x^h \text{ [cm]} \leq 0.2\ \lambda_{eff}\text{[cm]}/\sqrt{E\text{[GeV]}}$$

In compact calorimeters, where the effective nuclear interaction length λ_{eff} may be as low as 20 cm, spatial resolutions in the range of a few cm at 1 GeV are

achievable, reaching a few mm for $E \sim 100$ GeV. The resolution σ_x^h as a function of the transverse segment length $d(\lambda)$ has been evaluated[67] and a dependence of $\sigma_x^h \sim \exp(2d)$ may be derived, suggesting a limit on the useful transverse segmentation of $d \approx 0.1\lambda$.

The measurement of the **angular** resolution for e.m. (σ_θ^e) and hadronic showers (σ_θ^h) has been carefully studied for several calorimeters used to investigate neutrino scattering[65,68,69,70] and, more recently, for 4π calorimeter facilities at future hadron colliders[62] .

While the parametrization of the observed performance shows typically a $1/\sqrt{E}$ improvement of the angular resolution, the achieved values depend critically on the design of the apparatus. Typical results are quoted:

$$\sigma_\theta^e[\text{mrad}] \leq 20/\sqrt{E[\text{GeV}]} \text{ (refs. 69,70).}$$
$$\sigma_\theta^e[\text{mrad}] \simeq 3.5 + 53/E[\text{GeV}] \text{ (ref. 68).}$$

For carefully optimized hadronic angular resolution (achieved by choosing a material in which e.m. and hadronic showers have approximately the same spatial dimensions, *i.e.* $\lambda \approx 3X_0$), a value σ_θ^h [mrad] $\approx 160/\sqrt{E[\text{GeV}]} + 560/E[\text{GeV}]$ was reported[65,68,71] .

3.4 PARTICLE IDENTIFICATION

Hadronic calorimeters provide identification of a class of particles that are not readily identified by other methods and that are studied more and more often in very topical experiments (see Table I). In the following, we discuss in some detail the identification of electrons, muons, and neutrinos.

3.4.1 Discrimination between electrons (photons) and hadrons

Most frequently, discrimination is based on the spatial differences in the shower profiles, accentuated in absorber materials with very different radiation and absorption lengths, i.e. at high Z (see fig. 14). High-Z materials (lead, tungsten, uranium) are most frequently used to optimize the electron-hadron discrimination.

The principal physics limitation to this technique is the charge-exchange reaction $\pi^- p \rightarrow \pi^0 n$ (or $\pi^+ n \rightarrow \pi^0 p$), which may simulate an e.m. shower. For

few-GeV pions the cross-section for this reaction is at the 1% level of the total inelastic cross-section, and it decreases logarithmically with increasing energy[72] . Consequently, typical values for e/π discrimination are of the order of 10^{-2} in the 1 - 10 GeV range and 10^{-3} beyond 100 GeV[73,74,75,76,77] . A further improvement by a factor of 3 to 5 can be obtained if information on the transverse shower profile is available[78] .

The quoted rejection factors are based solely on the use of shower profile analysis. With additional momentum information, e.g. from magnetic momentum analysis, a further improvement in rejection of typically an order of magnitude is obtained.

A novel method, based on the differences in the time development of e.m. and hadronic showers, was recently tested successfully[79] (fig. 15). Using this technique, an e/π discrimination of 10^{-2} could be achieved for particles at 150 GeV, without using any information on the shower profile.

One of the most challenging detection problems, and of increasing importance for modern particle-physics experimentation, is the identification of electrons close to the core of high-momentum jets. One proposed solution[62] is based on a detailed three-dimensional measurement of energy deposit, through which e.m. showers appear as relatively energetic deposits, concentrated in a very small volume compared with the extension of the hadronic showers from the majority of the jet particles.

A related technique will be used by the ZEUS Collaboration, who will embed in their hadron calorimeter at a depth of $4X_0$ and $7X_0$ a layer of 40000 silicon detectors, each one having an active area of several cm^2. Pulse-height measurements in these Si elements will allow them to discriminate between high-particle-density e.m. showers and the relatively wide hadron showers, permitting electron identification in the presence of hadrons[80,81] .

3.4.2 Muon identification

Several calorimetric methods exist for discriminating between muons and hadrons, all based on the very large differences of energy deposit:

i) Calorimeters with fine longitudinal segmentation: energetic muons are clearly recognized as isolated, minimum-ionizing tracks, possibly ranging far beyond the tracks from hadronic showers. This is the technique used

in experiments on incident neutrinos, but also some of the highly granular collider detectors are expected to offer this identification potential.

ii) Muon penetration through active or passive absorbers: hadrons are adequately absorbed, so that the 'punch-through' probability of pions ($P \sim \exp[-d/\lambda]$) is sufficiently small. The absorber thickness d measured in *detectable* absorption lengths (λ), was found to agree closely with tabulated values for relatively thin absorbers[82,83,84] ($d \leq 10\lambda$), but shows significant deviations for absorber thicknesses $d > 10 - 15\lambda$[85,86] .

The detailed rejection power against hadrons depends critically on the experimental precautions taken; it may be improved by

a) reducing the background from π and K decay in front of the calorimeter,

b) measuring the muon momentum after the calorimeter, for instance in magnetized iron[87,88] or a precision spectrometer[89] ,

c) correlating the direction or the momentum of muon candidates before and after the absorber.

Very good muon identification will continue to be emphasized when considering experiments for future hadron colliders. In these experiments, accurate muon-momentum measurements will be mandatory because they will exploit *missing-energy* signatures in the search for new physics phenomena.

3.4.3 Neutrino identification

Apparent *missing energy* or *missing momentum* has become a powerful technique to infer the presence of neutrinos among the collision products:

a) Missing energy relies on a measurement of the total energy using 4π calorimetric coverage for all particles (charged, neutral, muons). This can in practice be achieved for collisions at e^+e^- storage rings or in fixed-target experiments. Neutrino production is inferred whenever the measured energy is lower than the total available energy and incompatible with the resolution function of the detector. A total-energy measurement is *not* practical at hadron colliders, because a considerable fraction of the total energy is produced at angles too close to the colliding beams, and hence inaccessible for calorimetric measurements. In this case it is advantageous to implement

b) A *missing-transverse-momentum* measurement, where neutrino production is signalled by $\Sigma \mathbf{p}_{\perp,i} \neq 0$, incommensurate with detector resolution. The intrinsic quality of such measurements was estimated to be $\sigma(\mathbf{p}_{\perp,miss}/\mathbf{p}_{total}) \approx 0.3/\sqrt{\mathbf{p}_{total}}$ [90] , considerably better than the values achieved up to now: $\sigma(\mathbf{p}_{\perp,miss}/\mathbf{p}_{total}) \approx 0.7/\sqrt{\mathbf{p}_{total}}$ [91,92,93] or $\sigma(\mathbf{p}_{\perp,miss} \approx 0.6\mathbf{p}_{\perp}{}^{0.43}[\mathrm{GeV}]$ [94] .

3.5 CALORIMETRIC SPECTROSCOPY OF MULTI-JET SYSTEMS

During the last decade, physics emphasis has been shifting from measurements of single particles to the analysis of jets of hadrons, which are the experimental manifestation of high-energy quarks and gluons. At future colliders, the spectroscopy of particles in the 0.1 - 1 TeV mass range will be pursued and will rely on the invariant-mass determination of multi-jet systems [95,96] .

Two distinct contributions affect this invariant-mass distribution. Firstly, unlike single particles, jets are *not* unambiguously defined objects, but have to be reconstructed with some algorithm [97] (fig. 16). Secondly, the calorimeter performance, and in particular the momentum response to different particles, will contribute to the mass resolution (fig. 17). This is also shown conceptually in fig. 18 for two different calorimeters. At high energies, $E \geq 50$ GeV, the jet resolution is dominated by the relative electron/hadron response. But even for ideal devices the jet definition based on a jet algorithm will introduce a measurement error. At very high energies, according to ref. 62, this will contribute to the total energy (and mass) resolution at the level of $2 - 4\%$.

3.6 SIGNAL PROCESSING

3.6.1 Readout systems for sampling calorimeters

A great number of different readout systems have been developed, reflecting the desire to tailor the systems performance to a physics application [1,2] .

Light-collecting techniques based on coupling scintillators to a photon detector have been used for two decades [98] . In recent years, the elegant technique of coupling the individual scintillator slabs through a wavelength shifter to the photon detector has permitted the compact, highly subdivided construction of rather uniformly sensitive calorimeters [99] .

Many modern detectors for storage ring experiments have built on this principle. The relative ease of the technique has to be weighted against some of the operational difficulties characteristic of the optical readout. The light collection is inherently non-uniform and deviations from uniform response at a level of $\sim$ 5% are typical for a well-constructed device. The optical system is also prone to significant long-term changes in the light-detection efficiency, limiting the systematic accuracy of the energy measurement (see section 3.6.2).

Charge-collection readout is the second widely used method, measuring the ionization charge liberated in gases, liquids and solids. Typical of these schemes is the easy segmentation, and the capability of operating in a magnetic field.

Charge collection in gases, usually followed by some degree of internal amplification, forms the basis for many rather diverse systems. The internal amplification facilitates the electronic signal processing, but is at the same time the source of an important systematic error, caused by non-uniformities in the gas gain of such detectors[100] .

Better control of systematic effects in the readout is usually found in the *ion-chamber* calorimeters, collecting the charge in a dielectric liquid (noble liquids, in particular liquid argon, room-temperature liquids such as tetramethylsilane and similar ones). These readout techniques may offer uniformity of response at the fractional per cent level, ease in fine-grained segmentation, good long-term stability, and high radiation resistance. Recent interest has focused on room-temperature liquids[37] , because these don't need the cryogenics which may introduce considerable insensitive areas in a 4π detector.

Another recent development concerns the use of silicon detectors as active elements. This technique has the attraction of the ion-chamber readout, without the need of a cryogenic system, nor the severe purity requirements characteristic for room-temperature liquids.

3.6.2 Calibration of the calorimeter response

In the previous chapters we argued that modern understanding of calorimeter performance permits energy measurements with few per cent precision for high-energy ($>$ 100 GeV) particles. This intrinsic excellent performance is, however, only achieved in large experimental facilities -frequently comprising several tens

of thousands of independent signal channels- if extraordinary care is taken to calibrate the absolute and relative energy scale, and to monitor all components of such a detector with a precision approaching or exceeding the 1% accuracy level. The success of existing or planned facilities depends on extensive, frequently redundant, sometimes ingenious monitoring systems, which need to be designed into the detector system from the very start and become an integral part of it. These monitor systems differ considerably depending on the type of calorimeter (photon- or charge-collection) and are particularly complex for scintillator-based devices.

In general, the following steps must be taken to establish and maintain the absolute and relative energy scale:

i) A number of calorimeter modules have to be exposed to muons, electrons, pions, and protons at different momenta. This procedure establishes the absolute energy scale, the relative response to hadrons and electrons, the energy resolution, and the linearity. Some groups have chosen not to expose *all* calorimeter cells to such a test-beam procedure[66,101,102] , but rather to rely on adequately tight construction tolerances (thickness of scintillator and absorber plates, uniformity of optical components), combined with a cosmic-ray muon calibration of all the detector cells to set the absolute energy scale. Other groups have chosen to expose all units to a test-beam calibration[103,104] .

ii) A monitoring system has to provide a reference signal for the transfer of the energy scale from the test-beam measurements to the experimental facilities and to maintain the long-term stability. For calorimeters with photon-collecting readout, the signal transfer standard is conceptually a light source whose stability is guaranteed by design (e.g. a ^{241}Am radioactive source embedded in a NaI scintillator) or whose light output is controlled with an adequate instrument. Such a stable light source is automatically provided in scintillator calorimeters using ^{238}U as their passive absorber. By a suitable choice of the signal integration time (ADC gate width), the number of photons induced by the radioactive ^{238}U decay can be made equivalent to the light generated by hadrons of 5 to 10 GeV[12,66,101] . Instead of or in addition to such light sources, many modern calorimeter facilities are using a complex system of light flashers, distributed from a light source (e.g. a N_2 laser) to the individual photomultipliers via a fibre-optics system[101,103,105,106]

In addition, remotely controlled, small radioactive sources scan the active calorimeter components (scintillator, wavelength shifters) and provide information on (possibly non-uniform) long-term changes[101,107] . Another alternative, frequently proposed, is the use of very stable particle accelerators providing low-energy particle beams of precisely known energy[108,109]

An example of a system used in practice is shown in fig. 19 , combining the use of U radioactivity, external radioactive sources, and a light-pulsing system.

The success of such attention to detail is demonstrated by the results shown in fig. 20 : it is possible to maintain long-term stability at the $1-2\%$ level[93] .

Calibration systems for calorimeters based on *proportional-gain wire-chamber readout* have to cope with both the inherent, comparatively large, gain variations between different wires, and the long-term global variations (changes in gas composition, pressure or temperature).

Adequate uniformity in gas-gain calorimetry can be achieved by controlling the mechanical tolerances. Such a dependence is minimized by using a rectangular tube geometry, a solution adopted for the majority of modern detectors. In very carefully constructed devices, gain variations of $\sigma \sim 5\%$[110,111] to 10%[112] are reported. Averaging of non-uniformities over the dimensions of the shower will reduce these gain variations to a level that should in most cases not affect the performance of these devices. The global gain variations due to gas composition, temperature and pressure are conveniently monitored with a suitable number of reference chambers[113,114] ; these calibration signals are sometimes used in a feedback circuit, adjusting the chamber HV to maintain constant global gain[113]

For charge-collecting calorimeters of the ion-chamber type (room-temperature liquids or LAr) excellent uniformity of response is ensured by controlling mechanical tolerances, and long-term stability is monitored by controlling the quality of the liquid medium. It is therefore sufficient to establish the absolute energy scale for a fraction of the modules of a detector and to transfer and maintain this scale with a precision charge measurement. This is conveniently done by injecting, with a precision pulse generator, a calibration charge into a precision calibration capacity of adequate stability (see also section 3.6.2).

3.6.3 Signal electronics

With increasing demands on the performance of calorimeters, the associated

electronics has developed into the most advanced and complex analog signal processing circuitry in instrumentation for particle physics. The electronics has to process the signal charge - delivered from a photomultiplier, a proportional wire chamber or an ionization chamber - and should therefore fulfil the following specifications:

a) A very large dynamic range: it should span the signals originating from minimum-ionizing particles (muons) to TeV-energy deposits of hadrons or relativistic ions. A dynamic range larger than 10^4 with 15- to 16-bit effective ADC resolution is required.

b) Low-level precision measurements of calibration signals (e.g. radioactive sources) must be possible.

c) Frequently, timing information is required.

d) An adequate time response (96 ns bunch crossing at HERA, 16 ns or faster at the SSC or LHC) imposes sometimes stringent constraints.

e) Information for the first-level trigger must be provided within $\approx 1\mu$s after a collision.

f) It must be adapted to system organization for 10^4 to 10^5 signal channels.

We illustrate the state-of-the-art in calorimetry front-end electronics with two examples. The functional analog readout for a *scintillator-based* calorimeter is shown in fig. 21 for the case of the ZEUS calorimeter, comprising $\sim$ 13000 photomultiplier (PM) channels[115] . Each PM output is resistively split into low- and high-gain shapers (to cover the required dynamic range), to a trigger sum, to a circuit for measuring the noise from the depleted uranium, and to a termination. The low- and high-gain channels are sampled individually every 96 ns, permitting both an amplitude and a timing measurement of the PM signal. The analog sample and pipeline is a custom VLSI chip based on switched-capacitor techniques. A 5 μs analog delay provides adequate time for trigger decisions before signal processing is continued.

Signal processing from *ion-chamber calorimeters* has to cope with two additional specific problems:

i) The detector capacitance C_D for practical devices is substantial ($\sim$ 1 to $\sim$ 100 nF), while the amplifier input capacitance C_A of typical low-noise FETs is $\sim$ 10 pF. If it is connected directly, the preamplifier 'sees' only a fraction of the produced charge in the ratio C_A/C_D.

ii) The detector capacitance C_D and the cable inductance L_C connecting the detector to the preamplifier limit the charge-transfer time $t_c \sim 3.5\sqrt{L_C C_D}$ and hence the speed of the detection process and detector.

In the classical approach[116] , in order to solve problem *i*) and to optimize the signal/noise ratio (S/N), a transformer is used to match C_D to C_A, as is shown in fig. 22. Coupling with such a $(n:1)$ transformer reduces the source capacitance by n^2, while the charge is reduced only by n, resulting in an S/N improvement of the factor n. The detailed analysis, using optimal bipolar pulse shaping of length λ, gives for the equivalent noise charge ENC due to the series-noise[116,117] $ENC \sim \sqrt{[C_D/\lambda]}$.

While the use of transformer matching results in optimal noise performance, it has two considerable practical drawbacks:

i) Transformers are quite bulky.

ii) Transformers use ferrite cores, which do not tolerate magnetic fields in access of ~ 0.01 T without external shielding.

These reasons, combined with the modern trend towards very high granularity and hence smaller detector capacitance, have led groups to circumvent the transformer matching problem by making the individual channel capacitance rather small ($C_D \approx 1$ nF) and accepting a certain degradation in S/N[118,119] . A typical block diagram of a single channel of ion-chamber electronics is shown in fig. 23[118] .

3.6.4 High-rate operation

In recent years the physics discovery potential of very high energy hadron colliders ($\sqrt{s} = 20 - 40$ TeV) was extensively discussed[120] . Such machines permit the study of physics approaching the 1 TeV mass scale, provided operation of the collider and of the associated experiments is performed at luminosities $L \approx 10^{33} - 10^{34}$ cm^{-2}s^{-1}, to compensate for the extremely small production cross-sections of the interesting reactions.

Precision calorimetry is expected to be the instrument of choice at these machines, prompting several studies on the feasibility of calorimeter operation at rates of $10^8 - 10^9$ collisions per second[121,122] . The average time between interactions will therefore be considerably shorter than the integration time for a hadronic shower measurement, which is typically ≈ 50 ns or longer. There are,

however, two reasons why calorimetry still performs well:

i) A collision may produce $\sim$ 100 secondary particles, depositing energy in perhaps 10% of the solid angle of a 4π detector. Measurement times on a particular readout channel may therefore extend over several collisions.

ii) At these very high luminosities, rare phenomena, revealed by very energetic jets of particles are searched for. The typical *average* inelastic collision deposits over an order of magnitude less energy, and may therefore be considered as *physics noise* affecting, but not necessarily masking, the measurement of the energetic events under study.

Several readout techniques can be considered for potential devices[20] :

a) Scintillator calorimeters are in principle the fastest detectors, particularly if the light is measured directly, without conversion in wavelength shifters[79]

b) Ionization-chamber calorimetry, although intrinsically slower, may also offer adequate time response. Certain dielectric liquids, such as tetramethyl silane, are particularly interesting in this respect, since the drift time in small gaps may approach values as low as 20-30 ns[123] .

The performance of ion-chamber calorimeters in a high-rate environment has been the subject of several studies. Crucial to such operation is the choice of bipolar-pulse shaping[124] , so that the pile-up of several events within the sensitive time of the detector does *not* on average produce a net shift in the measurement of a large signal. For such signal shaping (with total length λ of the bipolar weighting function), it can be shown that the pile-up of minimum-bias events with average energy E_b occurring at a rate of n per second will result in a pile-up noise contribution of $\sigma_{pileup} \approx E_b \sqrt{n\lambda}/3$.

The range of acceptable values of the product $n\lambda$ will therefore depend on the ratio of the energy E_s of interesting signals compared to the background E_b. More detailed estimates were done[121,122] , on which fig. 24 is based.

Consider, as an example, high-p_T jet spectroscopy, for which an acceptance of $\Delta\Omega \approx 1$ sr is required. With state-of-the-art LAr calorimetry ($\lambda \approx 200$ ns) and interaction rates of $n \approx 10^8$ s^{-1}, the pile-up noise is estimated to be as small as $\sigma_{pileup} \approx 1.5$ GeV, surely acceptable for jet physics at the multi-hundred GeV scale.

Such studies have indicated that there appears to be no *fundamental* limitation to adequate calorimeter spectroscopy, even at the very high luminosities considered. However, a long list of formidable technical challenges, such as construction problems, trigger bias, radiation damage, etc., will obviously require the most careful attention.

The dependence of the *electronic noise* on the signal shaping time, as achieved in practical devices, is also shown in fig. 24 . Again, for jet spectroscopy requiring 1 sr acceptance, and for rather short shaping times ($\lambda \approx 100$ ns), an electronics noise contribution of 2.5 - 5 GeV is measured, depending on the drift velocity in the liquid medium, which is comparable to the noise contribution from pile-up. These relatively short response times are achievable, provided attention is given to two overriding engineering considerations[124] :

i) The drift velocity of the ionization charge, which determines the induced current, must be adequately fast ($v_D \geq 1$ cm/μs).

ii) The time t_c to transfer the charge from the electrodes to the amplifier, which ultimately limits the response of the ionization chamber, must be adapted to the system.

An analysis has shown[124] that it may be t_c which imposes the most stringent requirements on the calorimeter construction: $t_c \approx 3.5(L_c.C_{det})^{1/2}$ and $\lambda \geq 5t_c$, where L_c is the cable inductance and C_{det} the detector capacitance. This very stringent limit on the cable inductance implies that the cable length l should be shorter than 1 m to achieve the required value of t_c.

Compared with the relatively long shaping times required for accurate energy measurement, the achievable *timing resolution* on a high-energy event is much smaller. Timing resolutions of $\sigma \approx 3 - 4$ ns have been measured for energy deposits of a few GeV, improving as $E^{-1/2}$[66] , and $\sigma \approx 1$ ns on 100 GeV energy deposits should be achievable with such calorimeters.

3.6.5 Trigger processors

The energy information from calorimeters is usually available in a rather short time interval, typically 50 to 500 ns after the particle impact. This important feature is, therefore, extensively used to select or *trigger* on interesting collisions, based on the pattern of the energy deposit.

The required selectivity depends on the type of collision under study. At today's hadron colliders, with collision rates of $\sim$ 1 MHz, the typical trigger selectivity approaches 1:10^5 or better. Considerably larger rejection factors (1:10^8) will be required at future colliders, where collision rates will approach or exceed 100 MHz.

The choice of the trigger scheme is probably the most delicate and critical ingredient for successful experimentation at hadron colliders. While very high selectivity is required, novel or unexpected event topologies must obviously not be rejected in this selection process. It is thus not surprising that triggering at the future colliders is emerging as one of the main concerns in the preparation of experiments[125.126.127.128].

The selection of events usually proceeds through a sequence of trigger levels of increasing restrictivity and refinement. As an example we describe the decision flow of the trigger processor development for the UA1 calorimeter, representative of the many modern trigger systems[129]. The flow-diagram is shown in fig. 25.

For the fast, first-level decision, signals from the very finely segmented calorimeter are summed to a certain degree, reducing the total number of 20000 channels to 1066 (548) trigger channels carrying e.m. (hadronic) energy information. These signals are encoded with Flash ADCs. The digital information is presented to memory look-up tables, from which the transverse energy E_T, the total energy E, and $E_T\sin\phi$ and $E_T\cos\phi$ are extracted.

At the first stage, information about e.m. clustering (for electron identification) is obtained. If any of the mentioned quantities exceeds a preset threshold, the event is presented to the second-level trigger for more refined analysis. The rejection of the first level typically exceeds $1 : 10^3$ and is executed in less than 4 μs.

At the second stage, selectivity is increased by searching for two-dimensional patterns in e.m. energy deposit (localizing electrons) and improving the jet definition. Such information is the basis of the final trigger criteria.

The range of selection criteria is further enlarged with signals from detectors external to the calorimeter, such as the momentum of muon candidates from the muon detector, or the momentum of electrons from the central tracking detector. Typical decision times at the second level amount to $\sim$ 1 ms and a rejection of 1:10 is achieved.

In the final, third level, a *farm* of several fast processors allows detailed event verification in $\sim$ 10 ms, with a further reduction of a factor of 10.

3.7 MONTE CARLO STUDIES OF CALORIMETRY.

The development of calorimeters from crudely-instrumented hadron absorbers to finely-tuned precision instruments owes much to a number of cascade simulation codes.

The relative simplicity of the physics governing the electromagnetic showers has facilitated early Monte Carlo simulation. The present-day world-wide *de facto* standard, EGS, has undergone a series of revisions and refinements. The current version, EGS4[6] , allows to track the shower electrons to zero kinetic energy and photons down to $\sim$ 10 keV. It has successfully passed many detailed tests[130] including one that may well be the ultimate, that of evaluating the absolute energy response to electrons within a few per cent in sampling calorimeters.

The physics, and consequently its simulation, is considerably more complex for hadronic showers. Over the last decade several programs have been developed, with the aim of simulating in all relevant detail the processes taking place in a hadronic cascade[131,132,133] . As an example, the flow-chart of one of these detailed codes is shown in fig. 26[134] .

These programmes continue to provide guidance to modern calorimetry development[22,135] . A recent example of a simulation summarizes results on the possible compensation in U-calorimeters read out with Si diodes (fig. 27).

Besides these very detailed codes, which probe the fundamental properties of particle cascades and detectors, there is need of a second category of codes, involving *fast* shower simulation for studies requiring a large number of particles, such as trigger efficiencies, acceptance calculations, etc. These approaches are usually based on global parametrizations[136] , parametric representation of hadronic interactions, evaluating individual π^0's, energetic charged π's and the low-energy nuclear cascades[137] , or other fast sampling techniques[138] .

3.8 CALORIMETER SYSTEMS

In the following discussion of calorimeter systems, we aim to show the great diversity of solutions adopted in the search of the 'best' solution adapted to a

specific physics application. Besides experimental considerations, the operating conditions of accelerators will influence the instrumental choices. We will explain these criteria, indicate strong points and weaknesses, and evaluate the trend in calorimetric approaches. Examples are selected of facilities in operation, in construction, or under preliminary evaluation.

3.8.1 Calorimeter facilities for fixed-target programmes

Among the largest facilities (considering the instrumented volume), we find detectors for neutrino studies, of which a recent version[139] is shown in fig. 28 . The design choices for this detector were driven by the need to achieve the best possible *angular* resolution for electrons (see section 3.3), a readout system allowing very good electron/hadron separation and muon-momentum measurement.

New high-granularity devices have also been constructed for experiments studying the hadronic production of jets[34,140,141,142] and high-resolution missing energy[142] . Choice of LAr readout allowed very-high-granularity detectors without any dead space, thus permitting a very good total-energy measurement. In one case uranium was chosen for best energy resolution up to very high energies. The studies of very rare events implied excellent measurement capabilities in the presence of rather high particle fluxes[34] (see section 3.6).

Interesting and novel techniques are being applied in the very low-energy physics programme at LEAR. The kinematics of $\bar{p}$-nucleus collisions produces events which are best detected by a 4π geometry reminiscent of storage ring devices. One such detector uses CsI crystals as a high-quality photon detector[143] These crystals have a very high light output, permitting detection with photodiodes, which can operate in strong magnetic fields[107] . Compared with NaI, the choice of CsI was suggested by the shorter radiation length, allowing a more compact spectrometer construction and better mechanical properties, without incurring higher costs (per X_0^3!).

The parameters of these facilities are summarized in Table II.

3.8.2 Calorimeter facilities at colliders

The calorimeter facilities devised during the last decade to be used in colliders, demonstrate the increasing importance of calorimetry and reflect a constant adaptation of techniques to the collider and physics environment[103,144] .

The original calorimeter facilities at the CERN $p\bar{p}$ Collider have undergone major improvement programmes. The UA1 Collaboration are at present preparing an extremely advanced device, based on the use of the room-temperature liquid TMP in an ion-chamber mode[145] . The group aims at good hermeticity, high granularity, good and uniform energy resolution, and good long-term stability.

Similar goals, but using conventional scintillator techniques, are pursued by the UA2 Collaboration[103] . The CDF Collaboration, at the FNAL Tevatron collider, have chosen scintillator readout for the central coverage and proportional-gas-gain technology for the end-caps[112,146] .

The D0 Collaboration are constructing a U/LAr calorimeter facility to be operated at the FNAL collider. It aims at good energy resolution ($e/h \leq 1.1$) for electrons and hadrons, and good granularity. The detector is housed in three independent cryostats, which introduces cracks in the 4π coverage and results in some loss of hermeticity[32,147] .

For the new generation of e^+e^- facilities (see Table II) a number of hadron-calorimeter facilities have been constructed, although most of these do not emphasize state-of-the-art performance. Emphasis is rather given to e.m. shower measurements with good granularity. The very low collision rates allow technically simpler, slow readout systems.

The CLEO Collaboration has adopted an innovative solution to precision e.m. calorimetry, using an array of $\sim$ 7000 CsI crystals, which permits an energy resolution of $\sim 2\%$ at 1 GeV[148] .

The TRISTAN e^+e^- collider, now operating at $\sqrt{s} \leq 55$ GeV, will ultimately reach $\sqrt{s} \approx 65$ GeV if it is equipped with superconducting cavities. Three major experiments are operational. AMY is a very compact detector, which has pioneered very-high-field ($B \sim 3\ T$) tracking[149] . The TOPAZ detector[150,151] also has e.m. calorimetry based on gas-readout in the end-caps, and uses a cylindrical lead-glass array in the $30^o < \theta < 150^o$ region, while the VENUS calorimeter uses both LAr and lead-glass e.m. calorimetry[152,153] .

At Stanford, the linear accelerator has been ingeniously transformed into the Stanford Linear Collider (SLC), providing e^+e^- collisions at $\sqrt{s} \leq 100$ GeV. The MARK II detector[154] has been upgraded and is at present installed at the SLC.

A very ambitious detector, SLD[155] , is being completed and could move into the collision hall by the end of 1989.

All four LEP experiments have chosen proportional-wire-chamber readout techniques for their hadron calorimetry and have pushed the performance of this technique to new heights[100] , particularly the ALEPH Collaboration[156] . The solutions chosen for the e.m. calorimetry are mechanically and electrically different from those for the hadron detector. DELPHI[157] , L3[158] , and OPAL[41] have adopted particularly performant technologies for their e.m. calorimetry.

We conclude from this short discussion on calorimeter facilities at existing e^+e^- colliders that state-of-the-art hadron calorimetry has not been vigourously implemented. High-precision jet-physics needing the best possible resolution was not considered a high-priority topic. Recent successes using the missing-energy technique will probably call for a revision of this attitude. It is not surprising that SLD, which is the most recently designed experiment, is the first one to aim at high-quality hadron calorimetry.

To date, the most stringent requirements on hadron calorimetry have to be met by the experiments being prepared for HERA. The physics programme relies to a large extent on the precision measurements of the jet momenta, *i.e.* their energy and direction.

The two experimental groups[101,159] at HERA have chosen very different calorimetry techniques, reflecting the sometimes subjective evaluation of the strengths and weaknesses of different techniques. In previous sections, we have already described the (expected) performance of these detectors. Figure 29 gives an impression of the very advanced design of the H1 calorimeter.

Looking beyond HERA towards the planned high-luminosity hadron colliders, we are witnessing an even stronger reliance on calorimetry as the principal spectroscopic tool. Conceptual experiments have been evaluated[160] , from which a consensus emerged that the known detection principles are *adequate* to conceive the necessary experiments. The technical difficulties are, however, stupendous, which is summarized aptly as: "We know how to build the accelerator, but we don't know yet how to build the experiments"[120,161] .

The technical challenge lies in the development of techniques that offer the required radiation resistance[162] , fast response in the environment of 10^9 to 10^{10}

collisions per second, signal processing from 10^6 channels with accuracies of 16 - 18 bits, and trigger capabilities approaching a selectivity of 10^9. Current thinking is summarized in the proceedings of the recent relevant workshops[160] .

3.8.3 Non-accelerator-based instruments

During the last ten years, a number of facilities have been constructed, mostly deep underground, to study some of the most fundamental questions in particle physics, such as the search for nucleon decay predicted by the Grand Unified Theories of the strong and electroweak interactions.

In the minimal SU(5) unification scheme, the proton lifetime is predicted to be in the range of 10^{30} years, with the dominant decay mode $p \rightarrow e^+ + \pi^0$. If this were true, a detector containing 10^{32} to 10^{33} protons (500 - 5000 tonnes of water) would in principle observe a few hundred to a few thousand proton decays per year[163] .

The best experimental technique is to instrument several thousand tonnes of material sensitively enough to detect a fair fraction of the expected proton decay modes: a calorimeter! One important complication is the presence of an overwhelming background due to muons produced in the atmosphere, whence the need for all these experiments to be installed deeply underground, shielded by more than a kilometer of rock.

Present nucleon-decay experiments are of two different types:

i) Calorimeters using most frequently iron as the decay mass, finely subdivided and interleaved with active elements, mostly based on wire-chamber technologies.

ii) Instruments using ultra-pure water as the decay mass, with photomultipliers detecting the Čerenkov light produced by the decay products of a possibly disintegrating nucleon.

A summary of the nucleon-decay detectors now in operation is given in Table III[164] .

Although the search for nucleon decay has been negative up to now, there are a number of very ambitious and advanced underground facilities in preparation. They address, besides more sensitive searches for nucleon decay, a wide range of topics: high-energy ν astronomy, very low-energy solar ν studies, search for magnetic monopoles, high-energy μ spectroscopy, etc.

A major new underground laboratory providing facilities for these experiments is in preparation under the Gran Sasso mountain in Italy. We mention two experiments that will use very novel detection techniques. The ICARUS detector is a 5000 t, continuously sensitive and homogeneous calorimeter, using liquid argon as the active material. Given the low event rates, ionization signals will be drifted over very large distances (typically 1 m) to reduce the overall number of readout channels.

Another experiment aims specifically at the study of very low-energy solar neutrinos. The target calorimeter is made from 30 t of $GaCl_3$, and the detection of solar neutrinos proceeds through the reaction $^{71}Ga + \nu_e \rightarrow {}^{71}Ge + e^-$, with a threshold of $E_\nu > 233$ keV.

The ultimate calorimeter in size uses more than 1000 km^3 of the earth's atmosphere. Very energetic cosmic-ray particles, incident on the upper layers of the atmosphere, will interact and initiate a hadronic cascade. The cascade particles excite the atmosphere (Čerenkov or fluorescent light), which is detected with an array of 67 light detectors (*Fly's Eye*)[165] .

Results obtained to date are a measurement of the total cross-section for pp scattering up to $\sqrt{s} = 15$ TeV and information on the shape of the cosmic-ray spectrum beyond 10^{19} eV[166] .

3.8.4 Cryogenic detectors

There is a growing interest in calorimetric methods characterized by a cryogenic operating temperature, in the few mK to $\sim$ 1 K range. Such detectors exploit either some specific properties of the superconductive phase of matter or the reduction in the thermal noise of the detecting medium (and the associated electronics). These methods promise energy measurements of considerably improved accuracy for the detection of energy deposits in the meV-eV range.

The development of these techniques is pursued because they may offer an experimental tool to answer some of the most fundamental questions in particle physics, such as

- the rest mass of neutrinos,
- the existence of weakly interacting massive particles (WIMP's), which may be a component of the *dark* matter in the Universe,

– the existence of magnetic monopoles,

– the solar neutrino flux at low threshold,

– the nuclear double β-decay.

Following earlier suggestions[167,168,169,170] , a great variety of detectors have been considered[171,172] , all of which are based on the following properties of matter at low temperatures:

i) Elementary excitations have very low energy. For example, Cooper pairs in superconductors have binding energies in the $10^{-6} - 10^{-3}$ eV range and may be broken by phonon absorption.

ii) The specific heat C for dielectric crystals ($C_{lattice} \approx a[T/\Theta_D]^3$) and superconductors ($C \approx b \exp[-1/kT]$) decreases to very low values at cryogenic temperatures.

iii) Thermal noise in the detector and the associated electronics decreases.

iv) Several cryogenic-temperature phenomena provide specific signals (e.g. change in magnetization, latent heat release, quasi-particle multiplication) which may be the basis of detectors.

In the following, we select among the many ingenious proposals three categories of detectors which are widely studied[171,173] .

Bolometers. These are the true 'calorimeters', where the energy deposition of particles in an insulating crystal at very low temperature may be measured with a resistive thermometer. The ultimate energy resolution (neglecting noise in the readout electronics) depends on the temperature T and the mass M of the crystal as $\Delta E \propto T^{5/2} M^{1/2}$, whence a sizeable increase in detector mass may be balanced by a modest decrease in temperature.

The rise-time of the signals from such devices is relatively fast (1 to 100 μs range). Energy resolutions as low as $\sigma \sim 7$ eV have been reported for 6 keV X-rays, approaching the range of interest for a measurement of the ν_e rest mass from ^{3}H decay. Relatively large devices (close to 1 g Ge as absorber) have been developed[174] ; background suppression has been achieved by measuring, in addition to the temperature rise, a complementary signal such as scintillation light. This procedure allows particle identification, i.e. differentiation between recoil nuclei and minimum-ionizing particles based on the temperature/light ratio.

The principle thrust of present-day bolometry is directed toward large devices

(100 - 1000 g) for the search of neutrinoless double β-decay, where good energy resolution is crucial for background suppression, and for dark-matter searches through the detection of nuclear recoil, where sensitivity to energy deposits below 1 keV is required.

Superconducting Tunnel Junctions (STJ). The very low excitation energy of current carriers in superconductors ($\leq 10^{-3}$ eV) has led to the development of STJs, in which the quasi-particles and -holes excited by incident radiation tunnel through a thin superconducting layer separating the two superconducting materials. For the detection of X-rays of a few keV, the energy resolutions observed to date are close to 0.1%.

Applications for ν-mass measurements and solar-ν-flux measurements might be contemplated. Such devices might also prove interesting as detectors of phonons produced in crystals, where ballistic phonons would be converted into quasi-particles.

Superheated Superconducting Granules (SSG). Type I superconductors can exhibit metastable states owing to a positive normal-superconducting interface energy. Type I samples may therefore remain superconducting in external magnetic fields in excess of the critical field H_c. This has been observed for metallic spheres with diameters in the 1 - 400 μm range.

SSG detectors are usually prepared as a colloid of metallic granules suspended in a dielectric matrix (e.g. paraffin). Heat deposited by a particle interaction would drive one or several granules normal, entailing a change of magnetic flux (disappearance of Meissner effect), which would be sensed by a macroscopic pickup coil.

Applications to the detection of solar neutrinos, based on the neutral-current process of elastic neutrino-nucleus scattering, appear attractive. Dark-matter searches, where the nuclear recoil flips only one sphere at best, require increased sensitivity, which might be achieved through a *micro-avalanche* mechanism[172].

Development of cryogenic detectors is actively pursued in a number of laboratories. They promise to open a new era in astro-particle physics. For the time being, studies of *principles* are being pursued, often involving fundamental research in solid-state physics and materials science. The feasibility of practical detectors of adequate size has yet to be shown, and their signal-processing requirements are at present far beyond the scope of the most advanced particle-physics instrumentation.

4. CONCLUSIONS AND OUTLOOK

The use of calorimetric detection methods in high-energy physics has rapidly evolved from a technique employed for some rather specialized applications (neutrino scattering) to the prime experimental tool in modern experiments.

This evolution, inspired by the physics goals of the experiments concerned, has gone hand in hand with crucial developments in the calorimeter technology itself. The sophistication of the instrumentation, the understanding of the basic principles of operation and of the limitations of the technique have all reached a very mature level, guaranteeing optimal exploitation possibilities.

Nevertheless, in view of the strongly increasing demands on calorimeter performance for future experiments, particularly at the proposed multi-TeV *pp* Colliders, further R&D is needed, which will have to focus on those calorimeter features which are likely to be essential in the next decade:

- hermeticity,
- energy resolution,
- rate capability,
- radiation resistance,
- electron/pion discrimination.

It is unlikely that one single instrument will emerge as the ultimate solution, best performing in all aspects listed above. Choosing a calorimeter technique for a particular experiment will remain a matter of evaluating (dis)advantages of different approaches.

We see two trends that are likely to shape detectors for future experiments. Firstly, *compensating* calorimeters will become the standard. As we pointed out in section 3.1, the compensation requirement does *not* necessarily imply the use of uranium absorber. When hydrogenous readout material is used (plastic scintillator, room-temperature liquids, gas) it can be achieved with a variety of absorber materials of which lead is probably the most attractive one.

Secondly, we expect a development towards *integrated* calorimetry, i.e. combining in one instrument the functions of e.m. and hadronic shower measurement, electron and muon identification; the traditional subdivision in an e.m. calorimeter and a hadron calorimeter will disappear.

Research and development and prototype studies will be an even more essential part of the experimental programme than in the present generation of experiments. The time scales involved, the size and the cost of the calorimeters simply do not permit design errors.

We hope that the information provided in this review may serve as guidance and encouragement for a continued perfecting of this very powerful and elegant experimental technique.

Acknowledgements

We are grateful to the many colleagues who have helped us in preparing this review by making their results available and discussing them with us.

REFERENCES

1. S. Iwata, Nagoya Univ., Report DPNU 3-79 (1979).
2. C.W. Fabjan, Calorimetry in High-Energy Physics, Report CERN-EP/85-54 (1985); published in: Experimental Techniques in High-Energy Physics, ed. T. Ferbel (Addison-Wesley Publishers, 1987).
3. Y.S. Tsai, Rev. Mod. Phys. **46** (1974) 815.
4. E. Storm and H.I. Israel, Nucl. Data Tables **7** (1970) 565.
5. L. Pages *et al.*, Atomic Data **4** (1972) 1.
6. W.R. Nelson, H. Hirayama and D.W.O. Rogers, The EGS4 Code System, Stanford, SLAC Report-165 (1985).
7. L. Landau and I. Pomeranchuk, Doklady Akad. Nauk. SSSR **92**, No. 3 (1953) 535.
8. A.B. Migdal, Phys. Rev. **103** (1956) 1811.
9. T. Yuda, Nucl. Instr. and Meth. **73** (1969) 301.
10. B. Rossi, High-Energy Particles (Prentice Hall, Englewood Cliffs, NJ, 1952), p. 16*ff.*
11. R. Kopp *et al.*, Z. Phys. **C28** (1985)171.
12. T. Akesson *et al.*, Nucl. Instr. Meth. **A262** (1987) 243.
13. C. Leroy *et al.*, Nucl. Instr. and Meth. **A252** (1986) 4.
14. M.G. Catanesi *et al.*, Nucl. Instr. and Meth. **A260** (1987) 43.
15. R. Wigmans, Nucl. Instr. and Meth. **A259** (1987) 389.
16. R. Wigmans, Energy Loss of Particles in Dense Matter - Calorimetry, Proc. of the ICFA School on Instrumentation in Elementary Particle Physics, Trieste, 1987, eds. C.W. Fabjan and J.E. Pilcher (World Scientific, Singapore, 1988).
17. See for example Y.K. Akimov, Scintillator Counters in High Energy Physics, Academic Press, 1965.
18. D.F. Anderson and D.C. Lamb, Nucl. Instr. and Meth. **A265** (1988) 440.
19. R.C. Munoz *et al.*, J. Chem. Phys. **85** (1986) 1104.

20. R. Wigmans, Calorimetry at the SSC, Proc. of the Workshop on Experiments, Detectors and Experimental Areas for the Supercollider, Berkeley, 1987, eds. R. Donaldson and M.G.D. Gilchriese (World Scientific, Singapore, 1988), p.608.

21. H. Brückmann *et al.*, Nucl. Instr. and Meth. **A263** (1988) 136.

22. J.E. Brau and T.A. Gabriel, Nucl. Instr. and Meth. **A238** (1985) 489.

23. R. Wigmans, Nucl. Instr. and Meth. **A265** (1988) 273.

24. H. Abramowicz *et al.*, Nucl. Instr. and Meth. **180** (1981) 429.

25. M. de Vincenzi *et al.*, Nucl. Instr. and Meth. **A243** (1986) 348.

26. C.W. Fabjan and W.J. Willis, *in:* Proc. of the Calorimeter Workshop, FNAL, Batavia, Ill., 1975, ed. M. Atač, p. 1; C.W. Fabjan *et al.*, Nucl. Instr. and Meth. **141** (1977) 61.

27. H. Tiecke (The ZEUS Calorimeter Group), Nucl. Instr. and Meth. **A277** (1989) 42.

28. R. Wigmans, Signal equalization and energy resolution for uranium/silicon hadron calorimeters, Report NIKHEF Amsterdam, NIKHEF-H/87-13 (1987).

29. E. Borchi *et al.*, Silicon sampling hadronic calorimetry: A tool for experiments at the next generation of colliders, preprint CERN-EP/89-28 (1989).

30. H1 Calorimeter Group, Performance of a Pb-Cu Liquid Argon Calorimeter with an Iron Streamer Tube Tail Catcher, preprint DESY 88-073, (1988).

31. G. d'Agostini *et al.*, Nucl. Instr. and Meth. **A274** (1989) 134.

32. M. Abolins *et al.*, Hadron and Electron Response of Uranium/Liquid Argon Calorimeter Modules for the D0 Detector, Brookhaven Report BNL-42336 (1989).

33. D. Hitlin, SLD liquid argon prototype tests, Proc. of the Workshop on Compensated Calorimetry, Pasadena, 1985, CALT-68-1305.

34. D. Gilzinger *et al.*, The HELIOS Uranium Liquid Argon Calorimeter, in preparation

35. Y. Galaktionov *et al.*, Nucl. Instr. and Meth. **A251** (1986) 258.

36. M. Pripstein (WALIC Collaboration), Requirements for the Development of Warm Liquid Calorimetry, Proc. of the Workshop on Future Directions in Detector R&D for Experiments at *pp* Colliders, Snowmass, Co., 1988, and private communication.

37. E. Radermacher (UA1 Collaboration), First results from a UA1 Uranium-TMP calorimeter module, preprint CERN-EP/89-01 (1989).

38. E. Bernardi *et al.*, Nucl. Instr. and Meth. **A262** (1987) 229.

39. E.B. Hughes *et al.*, Nucl. Instr. and Meth. **75** (1969) 130.

40. A. Benvenuti *et al.*, Nucl. Instr. and Meth. **125** (1975) 447.

41. R.M. Brown *et al.*, IEEE Trans. Nucl. Sci. **NS-32** (1985) 736; P.W. Jeffreys *et al.*, A Phototriode Instrumented Lead Glass Calorimeter for use in the Strong Magnetic Field of OPAL, Rutherford Lab report RAL-85-058 (1985).

42. U. Amaldi, Phys. Scripta **23** (1981) 409.

43. R. Wigmans, The Spaghetti Calorimeter Project at CERN, Proc. of the Workshop on Future Directions in Detector R&D for Experiments at *pp* Colliders, Snowmass, Co., 1988.

44. Y. Chan *et al.*, IEEE Trans. Nucl. Sci. **NS-25** (1978) 333.

45. H. Grassmann *et al.*, Nucl. Instr. and Meth. **228** (1985) 323.

46. J.A. Bakker *et al.*, Study of the Energy Calibration of a High Resolution EM Calorimeter, CERN-EP/89-16 (1989).

47. M. Laval *et al.*, Nucl. Instr. and Meth. **206** (1983) 169.

48. D.F. Anderson *et al.*, Nucl. Instr. and Meth. **228** (1985) 33.

49. R. Bouclier *et al.*, Nucl. Instr. and Meth. **A267** (1988) 69.

50. C.L. Woody and D.F. Anderson, Nucl. Instr. and Meth. **A265** (1988) 291.

51. K.L. Giboni *et al.*, Nucl. Instr. and Meth. **225** (1984) 579.

52. T. Doke *et al.*, Nucl. Instr. and Meth. **A237** (1985) 475.

53. E. Aprile *et al.*, Nucl. Instr. and Meth. **A261** (1987) 519.

54. V.M. Aulchenko *et al.* (KEDR Collaboration), paper submitted to the 24th Int. Conf. on High-Energy Physics, Munich, 1988; see also D.G. Hitlin, Proc. of the 24th Int. Conf. on High-Energy Physics, Munich, 1988 (Springer, Berlin, 1989), p. 1187.

55. M. Chen *et al.*, Nucl. Instr. and Meth. **A267** (1988) 43.

56. H. Burkhardt *et al.*, Nucl. Instr. and Meth. **A268** (1988) 116.

57. P. Sonderegger, Nucl. Instr. and Meth. **A257** (1987) 523, and references therein.

58. G.A. Akopdjanov *et al.*, Nucl. Instr. and Meth. **140** (1977) 441.

59. T. Kondo and K. Niwa, Electromagnetic shower size and containment at high energies, paper contributed to the Summer Study on the Design of the Superconducting Super Collider, Snowmass, Co. (1984).

60. I. Stumer and P. Yepes (HELIOS Collaboration), private communication (1989).

61. E. Gabathuler *et al.*, Nucl. Instr. and Meth. **157** (1978) 47.

62. T. Akesson *et al.*, Proc. Workshop on Physics at Future Accelerators, La Thuile and Geneva, 1987, ed. J. Mulvey, CERN 87-07, vol. I, p. 174 (1987).

63. A.L. Sessoms *et al.*, Nucl. Instr. and Meth. **161** (1979) 371.

64. Y. Muraki *et al.*, Radial and longitudinal behaviour of nuclear electromagnetic cascade showers induced by 300 GeV protons in lead and iron absorber, Univ. of Tokyo report ICR 117-84-6 (1984).

65. A.N. Diddens *et al.*, Nucl. Instr. and Meth. **178** (1980) 27.

66. T. Akesson *et al.*, Nucl. Instr. and Meth. **A241** (1985) 17.

67. F. Binon *et al.*, Nucl. Instr. and Meth. **188** (1981) 507.

68. D. Bogert *et al.*, IEEE Trans Nucl. Sci. **NS-29** (1982) 336.

69. J.P. DeWulf *et al.*, Nucl. Instr. and Meth. **A252** (1986) 443.

70. C. DeWinter *et al.*, Experimental results obtained from a low-Z fine-grained electromagnetic calorimeter, preprint CERN-EP/88-81 (1988).

71. I. Abt *et al.*, Nucl. Instr. and Meth. **217** (1983) 377.

72. A.V. Barns *et al.*, Phys. Rev. Lett. **37** (1970) 76. See also T. Ferbel *in*: Understanding the Fundamental Constituents of Matter, ed. A. Zichichi (Plenum Press, New York, NY, 1978).

73. J.A. Appel *et al.*, Nucl. Instr. and Meth. **127** (1975) 495.

74. D. Hitlin *et al.*, Nucl. Instr. and Meth. **137** (1976) 225.

75. R. Engelmann *et al.*, Nucl. Instr. and Meth. **216** (1983) 45.

76. U. Micke *et al.*, Nucl. Instr. and Meth. **221** (1984) 495.

77. C. DeWinter *et al.*, An Electron-Hadron Separator for Digital Sampling Calorimeters, preprint CERN-EP/88-87 (1988).

78. J. Cobb *et al.*, Nucl. Instr. and Meth. **158** (1979) 93.

79. R. Desalvo *et al.*, A Novel Way of Electron Identification in Calorimeters, to be published in Nucl. Instr. and Meth.

80. J. Krüger (ed.), The ZEUS Detector, Status Report 1987, Report PRC 87-02, DESY (1987).

81. C. Gössling, Large Area Silicon Detectors, Proc. 24th Int. Conf. on High-Energy Physics, Munich, 1988 (Springer, Berlin, 1989), p. 1208.

82. L. Baum *et al.*, Proc. Calorimeter Workshop, FNAL, Batavia, Ill., 1975, ed. M. Atač, p. 295.

83. A. Grant, Nucl. Instr. and Meth. **131** (1975) 167.

84. M. Holder *et al.*, Nucl. Instr. and Meth. **151** (1978) 69.

85. R. Leuchs, Messung des hadronischen Untergrundes bei der Identifizierung von Myonen, Tech. Univ. Aachen, 1982; K. Eggert (UA1 Collaboration), private communication.

86. F.S. Merritt *et al.*, Hadron Shower Punch Through for Incident Hadrons of Momentum 15, 25, 50, 100, 200 and 300 GeV/c, preprint Enrico Fermi Institute, ER 13065-41 (1985).

87. K. Eggert *et al.*, Nucl. Instr. and Meth. **176** (1980) 217.

88. F. Abe *et al.*, Nucl. Instr. and Meth. **271** (1988) 387.

89. Technical Proposal of the L3 Collaboration, CERN/LEPC/83-05 (1983).

90. W.J. Willis and K. Winter, *in* Physics with very high energy e^+e^- colliding beams, CERN 76-18 (1976), p. 131.

91. G. Arnison *et al.* (UA1 Collab.), Phys. Lett. **139B** (1984) 115.

92. P. Bagnaia *et al.* (UA2 Collab.), Z. Phys. **C24** (1984) 1.

93. P. Jenni (UA2 Collab.), Nucl. Phys. **B3** (Proc. Suppl.) (1988) 341.

94. L. Mandelli (UA2 Collab.), UA2 Results for the 1987 Run, preprint CERN-EP/88-182 (1988).

95. G. Alverson *et al.*, Detecting W/Z Pairs and Higgs at High Energy pp Colliders: Main Experimental Issues, Proc. of the Conf. on Physics of the Superconducting Super Collider, Snowmass, Co., 1986, eds. R. Donaldson and J. Marx (Amer. Phys. Soc., New York, 1987), p. 114.

96. D. Froidevaux, Experimental Studies, Proc. of the Workshop on Physics at Future Accelerators, La Thuile and CERN, 1987, ed. J.H. Mulvey (CERN 87-07, Geneva, 1987), vol. I, p. 61; J. Ellis and F. Pauss, *ibid.* p. 80.

97. T. Akesson *et al.*, Proc. ECFA-CERN Workshop on a Large Hadron Collider in the LEP Tunnel, Lausanne and Geneva, 1984, ed. M. Jacob (CERN 84-10, Geneva, 1984), p. 165.

98. J. Engler *et al.*, Phys. Lett. **29B** (1969) 321.

99. W. Selove *et al.*, Nucl. Instr. and Meth. **161** (1979) 233.

100. C.W. Fabjan, Nucl. Instr. and Meth. **A252** (1986) 145.

101. The ZEUS Detector, Technical Proposal, DESY, March 1986.

102. R. Klanner, Nucl. Instr. and Meth. **A265** (1988) 200.

103. A. Beer *et al.*, Nucl. Instr. and Meth. **224** (1984) 360.

104. J.A. Bakker *et al.*, High Energy Cosmic Muons and the Calibration of the L3 Electromagnetic Calorimeter, preprint CERN-EP/88-79 (1988).

105. S.R. Hahn *et al.*, Nucl. Instr. and Meth. **A267** (1988) 351.

106. M. Bonesini *et al.*, Nucl. Instr. and Meth. **A261** (1987) 471.

107. R. Batley *et al.*, Nucl. Instr. and Meth. **A242** (1985) 75.

108. D.R. Winn, IEEE Trans Nucl. Sci., **NS-33** (1986) 213.

109. H. Ma *et al.*, Calibration of the L3 BGO Electromagnetic Calorimeter with a Radiofrequent Quadrupole Accelerator, preprint Caltech CALT-68-1497 (1988).

110. A. Areviev *et al.*, Proportional Chambers for the Barrel Hadron Calorimeter of the L3 Experiment, preprint CERN-EP/88-76 (1988).

111. F. Camporesi *et al.*, Calibration of the Pad Readout Wire Proportional Chambers for the HPC Calorimeter, talk given at the IEEE Symposium on Nuclear Science, Orlando, 1988.

112. S. Cihangir *et al.*, Nucl. Instr. and Meth. **A267** (1988) 249.

113. J.P. De Wulf *et al.* (CHARM II Collab.), A detector for the study of neutrino and antineutrino scattering off electrons, to be published.

114. M.E.B. Franklin, Performance of the Gas Calorimetry at CDF, presented at the Topical Workshop on Proton-Antiproton Physics, FNAL, Batavia, Ill., 1988.

115. W. Sippach *et al.*, Development of the Front End Electronics for the ZEUS High Resolution Calorimeter, in preparation.

116. W.J. Willis and V. Radeka, Nucl. Instr. and Meth. **120** (1974) 221.

117. V. Radeka, Ann. Rev. Nucl. Part. Sci. **38** (1988) 217.

118. SLD Design Report, SLAC-Report 273 (1984).

119. H1 Collaboration: Technical Progress Report, DESY, October 1987.

120. C. Rubbia, Proc. Int. Symposium on Lepton and Photon Interactions at High Energies, Hamburg, Nucl. Phys. **B3** (Proc. Suppl.) (1988) 813.

121. A. Yamashita and K. Kondo, Physics Noise to Calorimetry at SSC, Proc. DPF Summer Study on the Physics of the Superconducting Supercollider, Snowmass, Co., 1986 (AIP, New York, 1987), p. 365; G.O. Alverson and J. Huston, Estimating background noise in LAr detectors due to pile-up, *ibid.*, p. 368.

122. C.W. Fabjan, Calorimetric Spectroscopy at Ultra-high Luminosities, *in* The Feasibility of Experiments at High Luminosity at the Large Hadron Collider, ed. J. Mulvey (CERN 88-02, Geneva, 1988), p. 19; P.T. Cox, *ibid.*, p. 25.

123. A. Gonidec *et al.*, Ionization Chambers with Room-temperature Liquids for Calorimetry, preprint CERN-EP/88-36 (1988).

124. V. Radeka and S. Rescia, Nucl. Instr. and Meth. **A265** (1988) 228.

125. T.J. Devlin *et al.*, Electronics, Triggering and Data Acquisition for the SSC, Proc. Workshop on Physics at the Superconducting Supercollider, Snowmass, Co., 1986, eds. R. Donaldson and J. Marx Amer. Phys. Soc, New York, 1987), p.439.

126. Proc. of the Workshop on Triggering and Data Acquisition for Experiments at the Superconducting Supercollider, Toronto (1989), eds. R. Donaldson and M.G.M. Gilchriese, to be published by World Scientific, Singapore.

127. F. Dydak *et al.*, Proc. of the Meeting on Fast Triggers, Silicon Detectors and VLSI, CERN, Nov. 1988, ed. B. Dobinson.

128. R.K. Bock, How can we get intelligent systems close to experiments, preprint CERN-EP/88-122 (1988).

129. E. Eisenhandler, The New UA1 Calorimeter Trigger, Rutherford Lab. report RAL-88-026 (1988).

130. T. Kondo, Proc. Summer Study on the Design and Utilization of the Superconducting Supercollider, Snowmass, Co., 1984, eds. R. Donaldson and J.G. Morfin.

131. T.A. Gabriel *et al.*, Nucl. Instr. and Meth. **134** (1976) 271.

132. T.A. Gabriel, Nucl. Instr. and Meth. **150** (1978) 145.

133. H. Fesefeldt, GEISHA: The simulation of hadronic showers, Aachen Univ. report PITHA 85/02 (1985).

134. T.A. Gabriel *et al.*, Nucl. Instr. and Meth. **195** (1982) 461.

135. J.E. Brau, Theoretical studies of hadron calorimetry for high-luminosity, high-energy colliders, talk given at the Int. Conf. on Advanced Technology and Particle Physics, Villa Olmo, Lake Como, June 1988. Univ. of Tennessee report UTHEP-88-0701 (1988).

136. R.K. Bock *et al.*, Nucl. Instr. and Meth. **A186** (1981) 533.

137. P. Pessoro, Etude de calorimétrie et simulation rapide des gerbes hadroniques. Thèse Ecole Polytechnique, Palaiseau, 1988 (unpublished).

138. D. Filges and P. Cloth (eds.), Proc. of the Int. Workshop on Calorimeter Simulation, Jülich, 1988 (JÜL-CONF 760, Jlich, 1988).

139. C. Busi *et al.*, Proposal to study neutrino-electron scattering at the SPS, CERN-SPSC/83-24 (1983).

140. F. Lobkowicz *et al.*, Nucl. Instr. and Meth. **A235** (1985) 332.

141. J. Huston *et al.*, paper presented at the 24th International Conference on High Energy Physics, Munich, July 1988.

142. H. Gordon *et al.*, CERN-SPSC/83-51 (1983).

143. E. Akes *et al.*, The Crystal Barrel: Meson Spectroscopy at LEAR with a 4π Neutral and Charged Detector, CERN-PSCC/85-56 (1985).

144. A. Astbury *et al.*, Nucl. Instr. and Meth. **A238** (1985) 288.

145. UA1 Collaboration, Design Report of a U-TMP Calorimeter for the UA1 Experiment with ACOL, CERN UA1-TN/86-112 (1986).

146. S. Bertolucci *et al.*, Nucl. Instr. and Meth. **A267** (1988) 301.

147. D0 Design Report: An Experiment at D0 to Study Antiproton-Proton Collisions at 2 TeV, 1983.

148. C. Bebek (CLEO Collab.), Nucl. Instr. and Meth. **A265** (1988) 258.

149. F. Kajino *et al.*, Nucl. Instr. and Meth. **A245** (1986) 507; A. Abashian *et al.*, Submitted to Nucl. Instr. and Meth.

150. K. Fujii *et al.*, Nucl. Instr. and Meth. **A236** (1985) 55.

151. S. Kawabata *et al.*, Nucl. Instr. and Meth. **A270** (1988) 11.

152. Y. Fukushima *et al.*, New Readout Electronics for the VENUS Liquid Argon Calorimeter at TRISTAN, KEK preprint 88-84 (1988).

153. T. Sumiyoshi *et al.*, Nucl. Instr. and Meth. **A271** (1988) 432.

154. A. Lankford, The Status of the SLAC Linear Collider and of the MARK II Detector, SLAC-PUB-4450 (1987).

155. SLD Design Report, SLAC-273 (1984).

156. M. Edwards, The ALEPH Electromagnetic Calorimeter, Rutherford Lab. report RAL-86-007 (1986); D. Schlatter, ALEPH note 88-10 (1988).

157. H.G. Fischer, Nucl. Instr. and Meth. **A265** (1988) 218.

158. R. Sumner, Nucl. Instr. and Meth. **A265** (1988) 252.

159. H1 Collaboration, Technical Proposal for the H1 Detector, DESY, (1986).

160. A wealth of information is found in: Proc. of the Workshop on Experiments, Detectors and Experimental Areas for the Supercollider, Berkeley,

1987, eds. R. Donaldson and M.G.D. Gilchriese (World Scientific, Singapore, 1988); Proc. of the Workshop on Future Accelerators, La Thuile and CERN, CERN 87-07 (1987); Proc. of the Workshop on Future Directions in Detector R&D for Experiments at *pp* Colliders, Snowmass, Co., 1988.

161. U. Amaldi, An Experimentalist's Overview on the Parallel Development of Accelerators and Detectors, Proc. of the ICFA School on Instrumentation in Elementary Particle Physics, Trieste, 1987, eds. C.W. Fabjan and J.E. Pilcher (World Scientific, Singapore, 1988).

162. M.G.D. Gilchriese (ed.), Radiation Effects at the SSC, SSC Central Design Group, Berkeley, report SSC-SR-1035 (1988).

163. D.H. Perkins, Ann. Rev. Nucl. Part. Sci. **34** (1984) 1.

164. J.L. Stone, Proc. of the ICFA School on Instrumentation in Elementary Particle Physics, Trieste, 1987, eds. C.W. Fabjan and J.E. Pilcher (World Scientific, Singapore, 1988).

165. G.L. Cassiday, Ann. Rev. Nucl. Part. Sci. **35** (1985) 321.

166. G.B. Yodh, Proc. of the ICFA School on Instrumentation in Elementary Particle Physics, Trieste, 1987, eds. C.W. Fabjan and J.E. Pilcher (World Scientific Singapore, 1988).

167. T.O. Niinikoski and F. Udo, Cryogenic Detection of Neutrinos, CERN-NP Internal Report 74-6 (1974).

168. E. Fiorini and T.O. Niinikoski, Nucl. Instr. and Meth. **224** (1984) 83.

169. A.K. Drukier and L. Stodolski, Phys. Rev. **D30** (1984) 2295.

170. B. Cabrera *et al.*, Phys. Rev. Lett. **55** (1985) 25.

171. K. Pretzl, N. Schmitz and L. Stodolsky (eds.), Low-Temperature Detectors for Neutrinos and Dark Matter (Springer Verlag, Berlin, 1987).

172. L. Gonzales-Mestres and D. Perret-Gallix, Cryogenic Detectors for Particle Physics, Annecy preprint LAPP-EXP-88-18 (1988).

173. L. Gonzales-Mestres *et al.*, Proc. of the 24th Int. Conf. on High-Energy Physics, Munich, eds. R. Kotthaus and J.H. Kühn (Springer Verlag, Berlin, 1989), p. 1222.

174. A. Alessandrello *et al.*, Phys. Lett. **202** (1988) 64.

Table I
Particle identification with calorimeters

Particle produced	Calorimeter technique	Comment
Electron, e	Charged particle initiating electromagnetic shower	Background from charge exchange $\pi^{\pm}N \rightarrow \pi^0 + X$ in calorimeter; π discrimination of $\sim$ 10–1000 possible
Photon, γ	Neutral particle initiating electromagnetic shower	Background from photons from meson decays
$\pi^0, \eta, \ldots \rightarrow \gamma\gamma$ $\varrho, \phi, J/\psi, \Upsilon, \ldots$ $\rightarrow e^+e^-$	Invariant mass obtained from measurement of energy and angle	Classical application for electromagnetic calorimeters;
Protons, deuterons, tritons..., and their antiparticles	Visible energy E_{vis} in calorimeter compared with momentum of particle	$E_{vis}^{b(\bar{b})} = (\vec{p}_b^{\,2} + m_b^2)^{1/2} - (+)m_b$ Protons (antiprotons) identified up to 4(5) GeV/c; deuterons (antideuterons) correspondingly higher
(Anti)neutrino	Visible energy E_{vis} in calorimeter compared with missing momentum	Important tool for $e^+e^- \rightarrow \nu(\bar{\nu}) + X$ and at CERN Collider (FNAL $p\bar{p}$ collider), $pp(p\bar{p}) \rightarrow \nu(\bar{\nu}) + X$
Muon	Particle interacting only electromagnetically (range). E_{vis} compared to $\vec{p}$.	Background from non-interacting pions or π and K decays
Neutron or $K_L^0(\bar{n}, \bar{K}_L^0)$	Neutral particle initiating hadronic shower	Some discrimination perhaps possible based on detailed (longitudinal) shower information

Table II

Construction and performance parameters of large calorimeter facilities

Accelerator	Facility	Principal physics goals	Calorimeter techniques Active	Calorimeter techniques Passive	Granularity	Performance	Comments	Refs.
CERN SPS	CHARM II	$\overset{(-)}{\nu_\mu}e \to \overset{(-)}{\nu_\mu}e$; $\sin^2\theta_w$ measurement	Plastic streamer tubes of ~ 10 mm spacing; orthogonal pick-up strips ~ 30 mm wide	0.5X_0 thick glass plates; ~ 700 t.	150000 dig. chan. (streamers); ~ 9000 analogue pick-up strips	$\sigma_{em} = 3\% + 28\%\sqrt{E}$; $\sigma_{em}(\theta) \approx 18\ \text{mrad}/\sqrt{E}$; $\sigma_{had} = 7\% + 40\%\sqrt{E}$	Optimized for angular resolution of e.m. showers.	139
	HELIOS	pp → leptons; E^{miss}; Study of ^{32}S-nucleus coll.	2.5 mm LAr gaps	e.m.: 1.7 mm ^{238}U; had: 3.4 mm ^{238}U;	e.m.: ~ 2000 tower segments; had: ~ 700 strips	$\sigma_{em} = 19\%\sqrt{E}$; $\sigma_{had} = 50\%\sqrt{E}$	Optimized for E_{tot} measurement at high rates (~ $10^6\ s^{-1}$); electron/hadron separation	34, 142
			2 mm scintillator	3 mm ^{238}U; Total ~ 300 t.	e.m.: 1200 towers; had: 1200 towers	$\sigma_{em} = 17\%\sqrt{E}$; $\sigma_{had} = 36\%\sqrt{E}$		
FNAL	E-706	(p, π, K)Be → high-$p_T\gamma$ + X → high-p_T jets + X	2.5 mm LAr gaps (total 40 m^3)	e.m.: 2 mm Pb; had: 2.54 cm stainless steel	e.m.: r-ϕ strips (6600 channels); had: triang. towers (2400 channels)	$\sigma_{em} \sim 15\%\sqrt{E}$	High granularity; high-rate operation; sub-cm spatial resolution of showers.	140, 141
CERN LEAR	Crystal Barrel	Meson spectroscopy	e.m. homogeneous CsI; 16X_0 deep vacuum-photodiode readout		e.m.: ~ 3 × 3 cm^2 cross-section; 1400 crystals.	$\sigma_{em} \approx 2\%\sqrt{E}$	Optimized for angular and energy resolution of cm showers	143

Table II (cont.)

Accelerator	Facility	Principal physics goals	Calorimeter techniques Active	Passive	Granularity	Performance	Comments	Refs.
CERN $p\bar{p}$ Collider	UA1	Top-quark search; m_W, m_Z; physics beyond SM; QCD tests.	3 mm TMP	e.m.: 2 mm U had: 5 mm U Total: 280 t	Tower structure; ~ 25000 analogue channels.	$\sigma_{em} = 13.3\% \sqrt{E} + 0.5\% E$ $\sigma_{had} = 47.5\% \sqrt{E} + 7\% E$	Very advanced design; technique prime candidate for calorimetry at future high-lumin. colliders.	145
	UA2	Same as UA1	4 mm acrylic scintillator for upgrade: somewhat finer sampling for central calorimeters	e.m.: 3 mm Pb had: 25 mm Fe	Tower structure 2-fold or 3-fold longitudinal segmentation ~ 3000 PM chan.	$\sigma_{em} \approx 16\% \sqrt{E}$ $\sigma_{had} \approx 30\% E^{3/4}$	Good hermeticity; good e/π separation; high long-term stability	103
FNAL Tevatron Collider	CDF	t-quark search; (beyond) SM and QCD tests.	Central: $30° < \theta < 150°$ 1 cm scintil.	2.5 cm steel 5.0 cm steel	Towers of $\Delta\phi \times \Delta\eta = 15° \times 0.11$; ~ 1350 PMs.	$\sigma_{had} \approx 80\% \sqrt{E}$ $\sigma_{em} \approx 24\% \sqrt{E}$ $\sigma_{had} \approx 110\% \sqrt{E}$	Essentially 4π covered with calorimetry	112 146
			Forward: $1.3 < \eta < 4.2$ Plastic tubes in proport. mode	e.m.: 2.3 mm Pb (first $21X_0$) had: 5.0 cm Fe (last $58X_0$)				
	D0	Same as CDF	2 × 2.3 mm LAr	e.m.: 3 mm U had: 6 mm U	Tower structure; 8-fold longitudinal segmentation ~ 50000 analogue channels.	$\sigma_{em} \approx 15\% \sqrt{E}$ $\sigma_{had} \approx 50\% \sqrt{E}$	Three-cryostat solution (1 central, 2 end-caps) reducing hermeticity	32 147
Cornell	CLEO	γ-spectroscopy B-meson decays	e.m. calorimeter only CsI(Tl) crystals ~ $16X_0$ long		~ 7000 crystals of 5 × 5 cm^2 cross-section	$\sigma_{em} \sim 1.6\% \sqrt{E}$ (single crystals) $> 3.5\% \sqrt{E}$ (full array)	Optimized for angular and energy resolution of e.m. showers	148

Table II (cont.)

Accelerator	Facility	Principal physics goals	Calorimeter techniques Active	Passive	Granularity	Performance	Comments	Refs.
KEK TRISTAN	AMY	Physics with e^+e^- collisions; test of QCD and SM	Plastic tubes total thickness 10.3 mm, cathode pads	3.5 mm Pb (first $9.4X_0$) 7 mm Pb (last $5X_0$)	~ 10000 channels 5-fold longitud. segmentation	$\sigma_{em} \simeq 20\% \sqrt{E}$ (B = 0 T) $\sigma_{em} \sim 15\% \sqrt{E}$ (B = 3 T)	Optimized for e/π discrimination	149
	TOPAZ	Same as AMY	End-caps (e.m. calorimeter only): Plastic tubes 10×15 mm^2 Pb 2 mm (first $3X_0$) Pb 3 mm (subsequent $15.5X_0$) $30° \leq \theta \leq 150°$ (e.m. calorimeter only) Pb-glass blocks (behind $1X_0$ thick superconducting coil)		3-fold longitud. segmentation, 2×1024 pads 4300 blocks, $\approx 122 \times 113$ mm^2	$\sigma_{em} = 19\% \sqrt{E}$ $\sigma_{em} \gtrsim 8\% \sqrt{E}$		150 151
	VENUS	Same as AMY	End-caps: 3 mm LAr	1.7 mm Pb Barrel: $37° < \theta < 143°$ Pb-glass blocks	Tower structure ~ 3800 analogue channels 5160 channels	$\sigma_{em} = 1.4\% E_T + 11.3\% \sqrt{E}$ $\sigma_{em} = 0.7\% E_T + 5.2\% \sqrt{e}$	Optimized for energy resolution of e.m. showers	152 153
Stanford SLC $\sqrt{s} \lesssim$ 100 GeV	Mark II	Precision tests of SM; t-quark, Higgs search.	e.m. calorimeter only 3 mm LAr	2 mm Pb	Projective strip readout 6-fold longitudinal segmentation	$\sigma_{em} = 12\% \sqrt{E}$		154
	SLD	Same as Mark II	2.75 mm LAr gaps	e.m.: 2 mm Pb had.: 6 mm Pb	Tower structure 4-fold longitudinal segmentation, $\approx$ 32500 channels	$\sigma_{em} \approx 8\% \sqrt{E}$ $\sigma_{had} \approx 45\% \sqrt{E}$	Optimized for good E resolution, aiming for good hermeticity in 'barrel' calorim.	155

Table II (cont.)

Accelerator	Facility	Principal physics goals	Calorimeter techniques Active	Passive	Granularity	Performance	Comments	Refs.
CERN LEP $\sqrt{s} \leqslant$ 200 GeV (reached in several improvement programmes)	ALEPH	Precision tests of SM; t-quark and Higgs search	e.m.: pad readout of Al tubes had: plastic tubes	e.m.: 2 mm Pb (first $12X_0$); 4 mm Pb (last $10X_0$); had: 5 cm Fe.	~ 70000 towers 3-fold longit. segmentation (210000 chan.) 4800 towers	$\sigma_{em} \approx 18\% \sqrt{E}$ $\sigma_{had} \approx 80\% \sqrt{E}$	Very high uniformity, achieved through very good control of mechanical tolerances	156
	DELPHI		e.m.: TPC readout had: plastic tubes	e.m.: 3 mm Pb; had: 5 cm Fe	e.m.: O(1 cm^3)!	$\sigma_{em} \approx 16\% \sqrt{E}$ $\sigma_{had} \approx 100\% \sqrt{E}$	Extremely high granularity, through TPC-like readout in e.m. calorimeter	157
	L3		e.m.: BGO with photodiodes had: brass tubes	had: 5 mm ^{238}U	e.m.: ~ 12000 towers had: ~ 22000 segments	$\sigma_{em} \approx 25\% E + 2\% \sqrt{E}$ $\sigma_{had} \approx 55\% \sqrt{E} + 0.05$	Very good E resolution for isolated γ and e	158
	OPAL		e.m.: Pb-glass with phototriodes had: proportion. chambers with pads; strip system	had: 8 cm Fe	~ 11700 towers had: ~ 20 × 20 cm^2 towers; 10000 strips for μ identifation	$\sigma_{em} \approx 6\% \sqrt{E} + 0.2\% E$ $\sigma_{had} \approx 120\% \sqrt{E}$	Good granularity and energy resolution	41

Table II (cont.)

Accelerator	Facility	Principal physics goals	Calorimeter techniques Active	Passive	Granularity	Performance	Comments	Refs.
HERA	H1	Properties of electroweak currents; proton structure function; exotic particle searches	3 mm LAr	2.8 mm Pb 12 mm stainless steel	Pseudo projective towers e.m.: 3- or 4-fold longit. segment. had: 4- or 6-fold longit. segment. Total of 42000 e.m., 18000 hadronic channels	Expected $\sigma_{em} \sim 10\% \sqrt{E}$ $\sigma_{had} \lesssim 65\% \sqrt{E}$ 'e/π' ≈ 1 (off-line)	Extremely high granularity; high longitudinal permits off-line energy weighting for 'e/π' $\approx$ tuning	159
	ZEUS	Same as above	3 mm scintil.	e.m. and hadronic: 3.2 mm ^{238}U	e.m.: 5×20 cm^2 had: 20×20 cm^2 Total: 13000 PM channels	Expected $\sigma_{em} \sim 18\% \sqrt{E}$ $\sigma_{had} \sim 35\% \sqrt{E} + 2\%$	Very good uniformity achieved through tight control of mechanical and opt. tolerances: silicon pixel detect. at 3 and $6X_0$ for e/π discrimination	101
High-lumin. hadron colliders		Physics of the 1 TeV scale [e.g. massive Higgs, SUSY particles]	Need for compensation at $e/\pi \lesssim 1.1$ level. Different techniques may be viable		Typical granularity $\Delta\phi \times \Delta\eta \lesssim 0.05 \times 0.05$ several longitudinal segmentations	Reference design $\sigma_{em} \sim 15\% \sqrt{E}$ $\sigma_{had} \lesssim 50\% \sqrt{E}$	Choice of calorimetry technique strongly influenced by radiation-hardness considerations (including readout electronics)	160

Table III
Properties of the nucleon decay detectors

Experiment	Total mass (t)	Detector granularity	Depth (mwe)	Detector elements	Lifetime sensitivity (years)
KGF	140	Iron 3 mm	7600	1700 proport.	10^{31}
Soudan I	30	Taconite 2 cm	1800	3456 proport.	10^{30}
NUSEX	150	Iron 1 cm	5000	47000 streamer	10^{31}
Fréjus	900	Iron 3 mm	4200	10^6 flash tubes	10^{32}
HPW	800	Water	1600	704 PMTs	10^{33}
Kamioka	3000	Water	2700	1044 PMTs	10^{33}
IMB	8000	Water	1600	2048 PMTs	10^{33}

FIGURE CAPTIONS

1. Shower development induced by few-MeV nuclear γ's. In diagramme *a*), one possible sequence of absorption processes is shown, with the energies of the e^+, the e^-'s, and the γ's given in keV. The γ-spectrum measured with a Ge(Li) crystal that only partly contains the showers initiated by (among others) the 3370 keV γ is shown in diagrammes *b*). The total-containment peak (3369.9 keV), the single-(2858.9 keV) and double-escape peak (2347.8 keV), and the continuum background reflect the different degrees of absorption that may occur in this crystal (see text).

2. The cross-sections for pair production, Compton scattering and photoelectric effect, as a function of the photon energy in carbon (a), iron (b), and uranium (c). The fractional energy loss by radiation and ionization, as a function of the electron energy in carbon (d), iron (e), and uranium (f).

3. The energy deposit as a function of depth, for a 10 GeV electron shower developing in aluminium, iron, and lead, showing approximate scaling of the longitudinal shower profile, when expressed in units of radiation length, X_0. Results of EGS4 calculations.

4. The lateral distribution of the energy deposited by a 1 GeV e.m. shower in lead, at various depths. Results of EGS4 calculations.

5. The energy loss distributions, ΔE_μ, for 8 - 200 GeV muons, measured in a 8.5 nuclear interaction lengths deep uranium/plastic-scintillator calorimeter. The dashed line, drawn to guide the eye, corresponds to the most probable energy loss, measured for 200 GeV muons. Data from ref. 12.

6. Longitudinal (top diagramme) and lateral (lower diagramme) shower profiles for 300 GeV π^- interactions in a block of uranium, measured from the induced radioactivity. The ordinates indicate the number of radioactive decays of a particular nuclide, produced in the absorption process of the high-energy pion. Since the different nuclides are produced by different types of shower particles, such experimental data may yield valuable information on details of the shower development process (from ref. 13).

7. The leakage as a function of the detector depth, for pions of 5 - 210 GeV, measured in a uranium/plastic-scintillator calorimeter. Data from ref. 25.

8. The fraction of the ionization energy deposited in the active layers by non-interacting protons, in various calorimeter configurations. From ref. 16.

9. Experimental observation of the consequences of $e/h \neq 1$. Results of measurements on pion absorption in undercompensating[24], compensating[12], and overcompensating[25] calorimeters. In diagramme *a*), the energy resolution $\sigma/E.\sqrt{E}$ is given as a function of the pion energy, showing deviations from scaling for non-compensating devices. In diagramme *b*), the signal per GeV is plotted as a function of the pion energy, showing signal non-linearity for non-compensating detectors. The signal distribution for monoenergetic pions (the line shape, diagramme c) is only Gaussian for the compensating calorimeter.

10. The signal ratio e/h for uranium calorimeters employing different readout materials, as a function of the ratio of the thicknesses of absorber and readout layers. Results of experimental measurements are included. From ref. 15.

11. The e/h signal ratio as a function of Birk's constant k_B, for TMP calorimeters with uranium (a) and lead (b) absorber. The liquid gaps are 2.5 mm wide. From ref. 20.

12. The HELIOS calorimeter as a high-resolution spectrometer. Total energy measured in the calorimeter for minimum-bias events, showing the composition of the CERN heavy-ion beam. Data taken from ref. 12.

13. The ratio of the e.m. to hadronic response as a function of energy, for various calorimeter configurations, showing the non-linearity for hadron detection at low energy.

14. The ratio of the nuclear interaction length and the radiation length as a function of Z.

15. Time distribution of the full width at half maximum for 150 GeV electron and pion pulses from a lead/scintillation-fibre calorimeter. Data from ref. 79.

16. Two-jet mass resolution as a function of the two-jet mass and for various assumptions on the detector performance. See ref. 97 for more details.

17. Two-jet invariant-mass distribution from UA2. The smooth curves are the results of the best fits to the QCD background alone (curve *a*) or including two Gaussians describing W and Z decays (curve *b*). The measured width is 8 GeV, of which 5 GeV can be attributed to non-ideal calorimeter performance[93] .

18. Jet resolution for an infinitely thick 4π calorimeter, assuming a Feynman-Field-like fragmentation function. The advantage of a (nearly) compensated calorimeter is particularly evident at very large jet energies. From ref. 97.

19. Schematic arrangement of the light flasher calibration system being built for the ZEUS calorimeter facility. One N_2 laser is the source of light, which is distributed in two stages to all of the approximately 13000 photomultipliers. Provision is made for linearity measurements, using remotely controlled neutral-density filters, absolute light level monitoring [with vacuum photodiodes, NaI(^{241}Am) light sources and Si photodiodes] and pulsing with LEDs for timing and triggering purposes (from ref. 80).

20. Long-term stability of a number of UA2 calorimeter modules. After several years of operation, remeasurement in a test beam demonstrated the validity of the energy scale within $\sigma \sim 2\%$.

21. Analog readout architecture for the photomultiplier signals of the ZEUS calorimeter. The signals are split, shaped, sampled and delayed in a custom VLSI chip, and subsequently multiplexed[115] .

22. Transformer matching of an ion-chamber calorimeter with capacitance C_D to the input of a preamplifier.

23. Block diagram of a single channel for a liquid-argon calorimeter, showing the preamplifier, the shaper, and the data-acquisition section.

24. Estimates (solid lines) of pile-up noise (left ordinate) as a function of the product of the shaping time λ and the collision rate n (bottom abscissa) for two different sensitive areas. It is compared with the typical electronic noise, as realized in the HELIOS U/LAr calorimeter (dashed lines), as a function of the signal shaping time λ (right-hand ordinate and top abscissa).

25. Decision flow in the UA1 trigger processor.

26. Flow-chart of one of the hadronic cascade codes[134] .

27. The calculated variation of e/h and $\sigma/\sqrt{E}$ with the thickness of a fibreglass sheet placed between the 2 mm uranium plates in a U-Si calorimeter and the silicon detectors. Without Si a slight overcompensation is expected, which can be tuned by changing the thickness of G10[135] .

28. Overview of the CHARM II detector. One of the inserts shows the use of several techniques (scintillator counters, streamer tubes, cathode pick-up strips) for the energy and direction measurement of the showers. The detector is combined with modules of the CDHS ν-detector (no longer operational), which are used for muon momentum analysis.

29. Partial cross-section through the H1 liquid-argon calorimeter, which has rotational symmetry about the beam axis. Shown is the transverse and longitudinal segmentation, which permits a quasi-projective tower geometry, pointing to the interaction point IP.

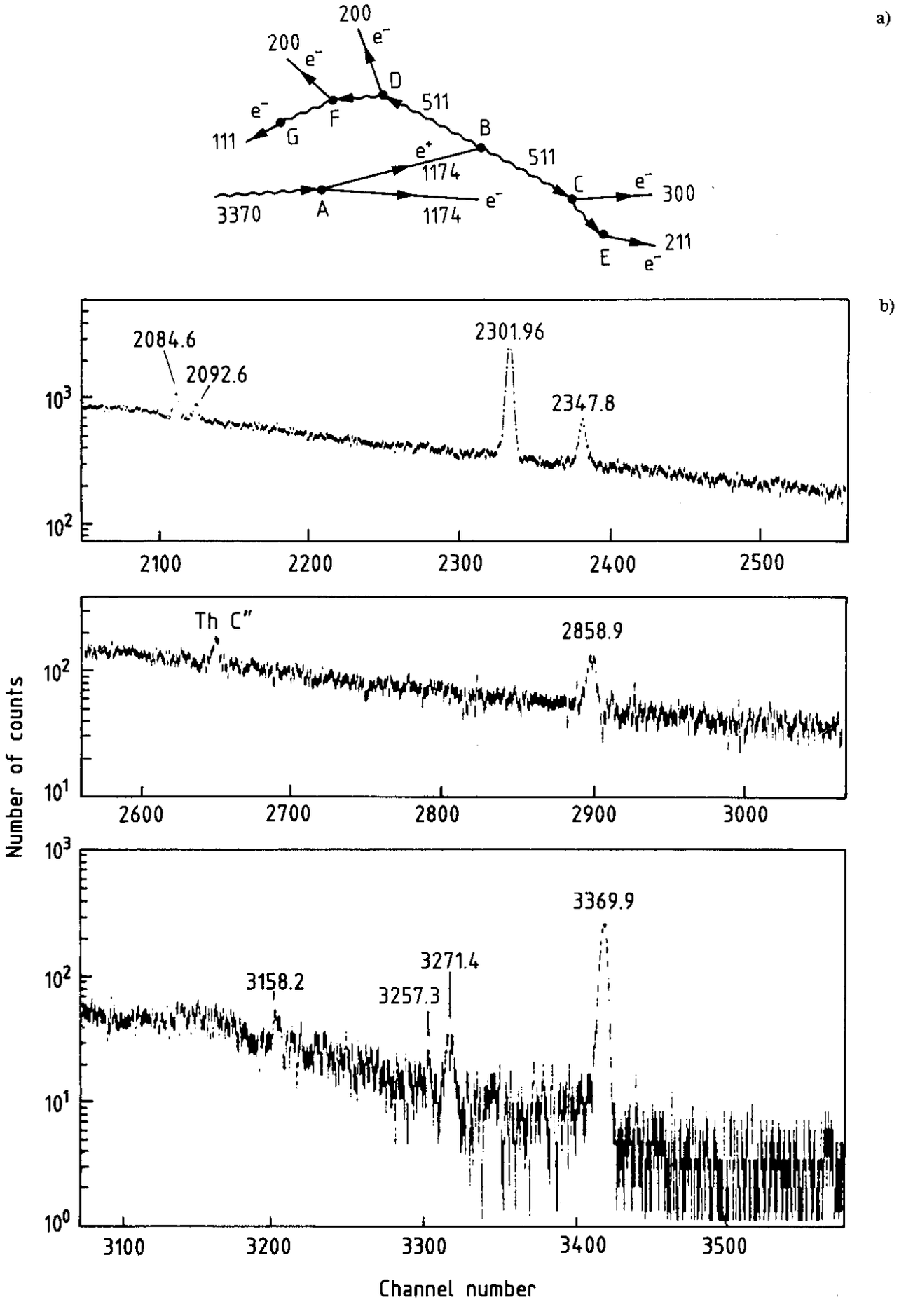
a)
200
e⁻
200
e⁻
D
511
e⁻
F
111
G
B
511
e⁺
1174
C
e⁻
300
3370
A
e⁻
1174
211
E
e⁻
b)
2084.6
2092.6
2301.96
2347.8
Th C″
2858.9
3369.9
3271.4
3158.2
3257.3
Number of counts
Channel number

Fig. 1

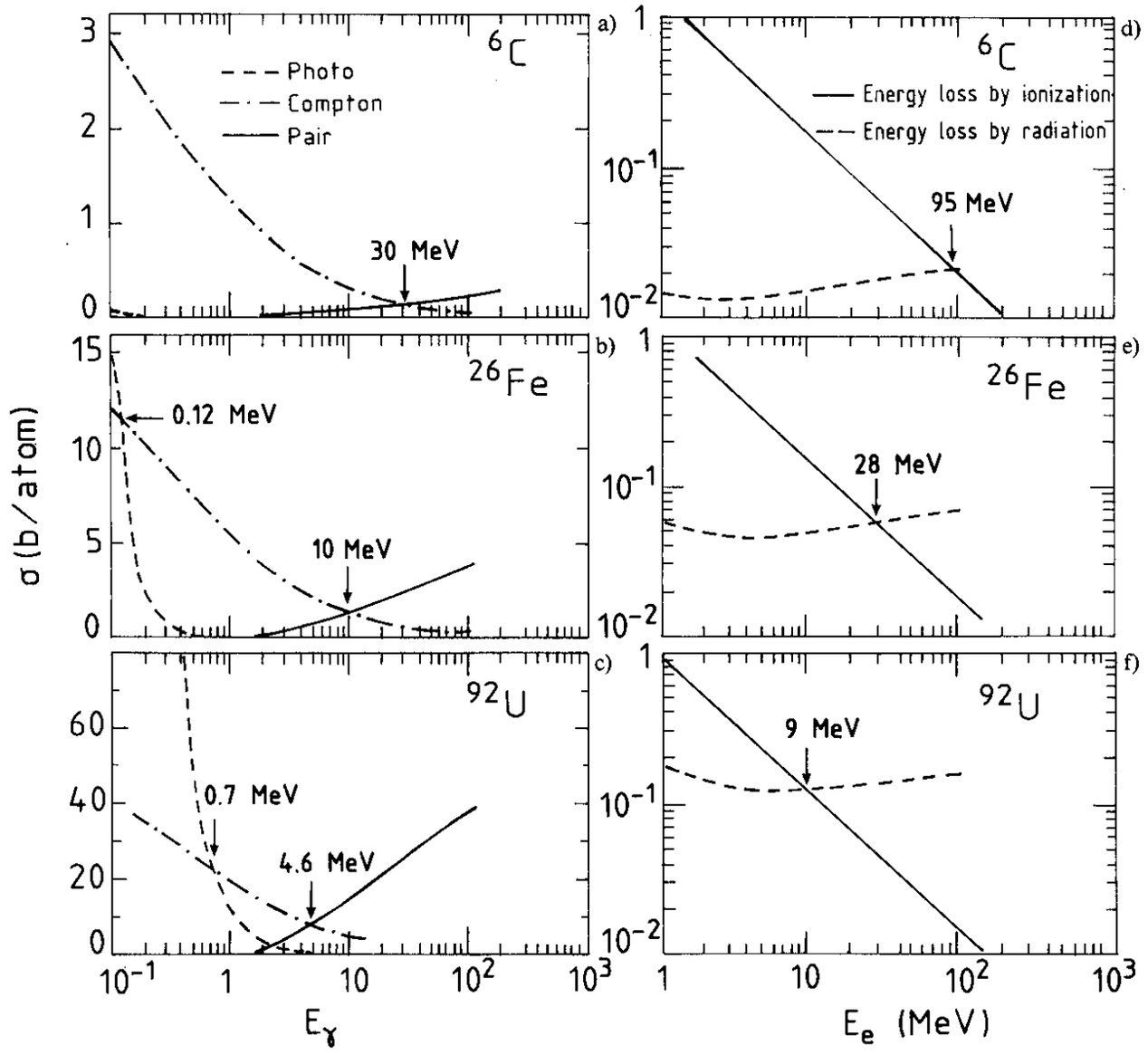
a)
b)
c)
d)
e)
f)
^{6}C
^{26}Fe
^{92}U
Photo
Compton
Pair
Energy loss by ionization
Energy loss by radiation
30 MeV
95 MeV
0.12 MeV
10 MeV
28 MeV
0.7 MeV
4.6 MeV
9 MeV
σ (b/atom)
E_γ
E_e (MeV)

Fig. 2

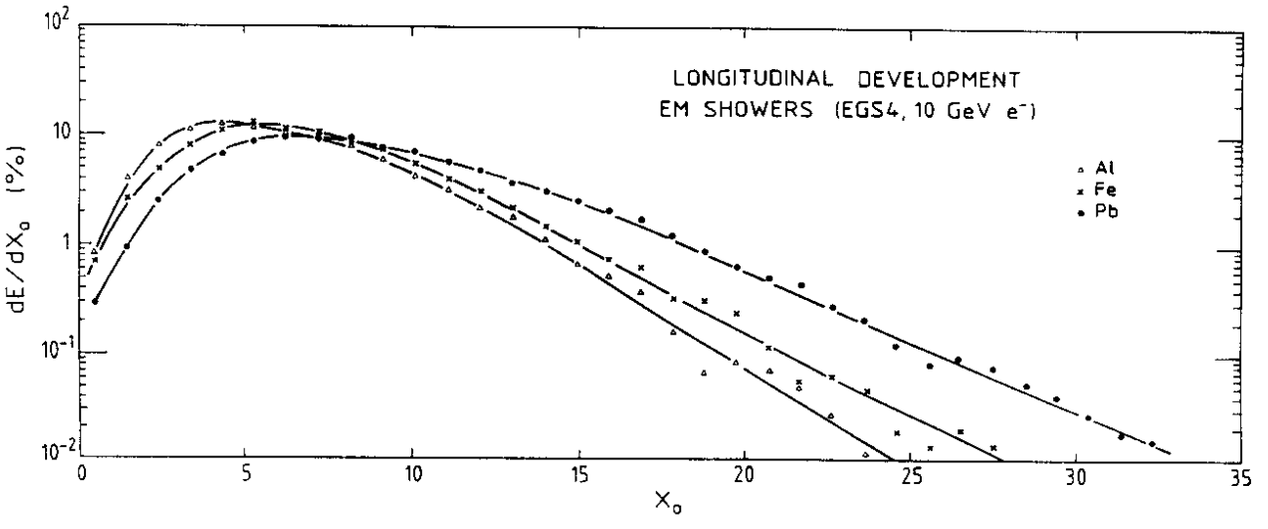
LONGITUDINAL DEVELOPMENT
EM SHOWERS (EGS4, 10 GeV e⁻)
Al
Fe
Pb
dE/dX₀ (%)
X₀

Fig. 3

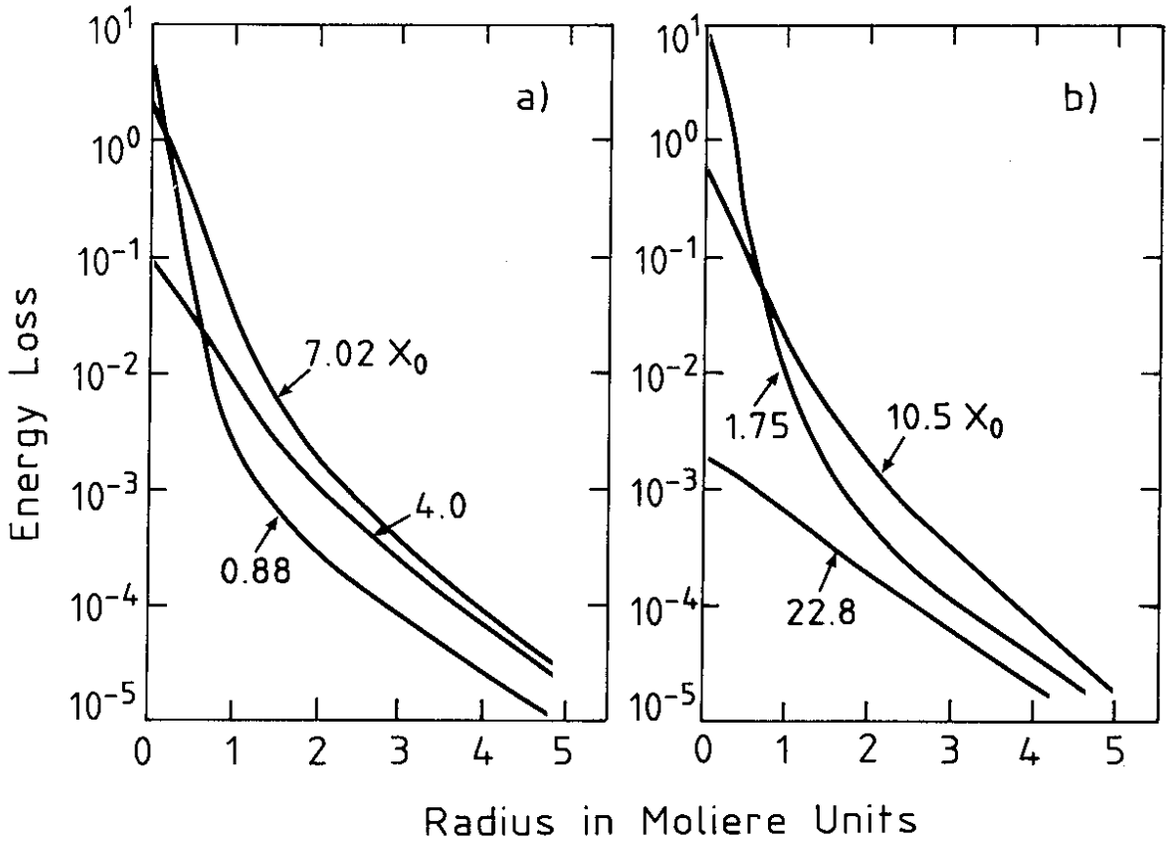
a)
b)
Energy Loss
7.02 X0
4.0
0.88
1.75
10.5 X0
22.8
Radius in Moliere Units

Fig. 4

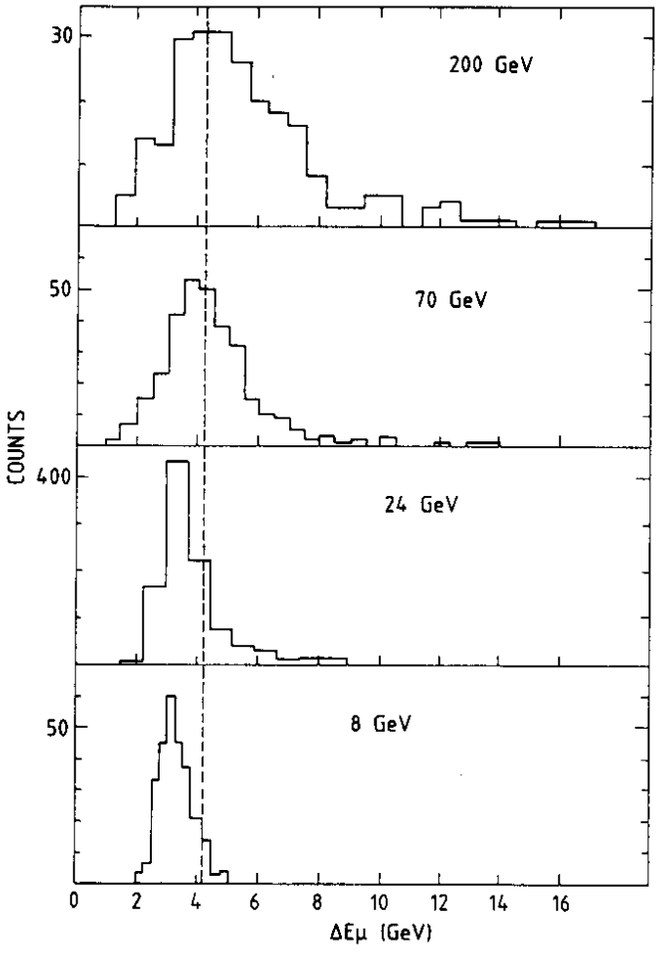
200 GeV
70 GeV
24 GeV
8 GeV
COUNTS
ΔEμ (GeV)

Fig. 5

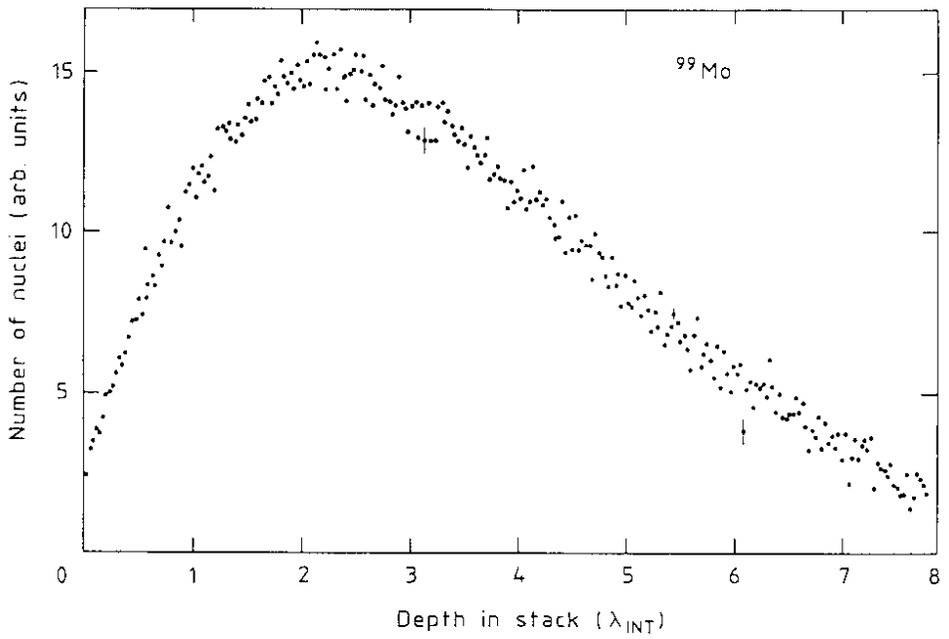
^{99}Mo
Number of nuclei (arb. units)
Depth in stack (λ_{INT})

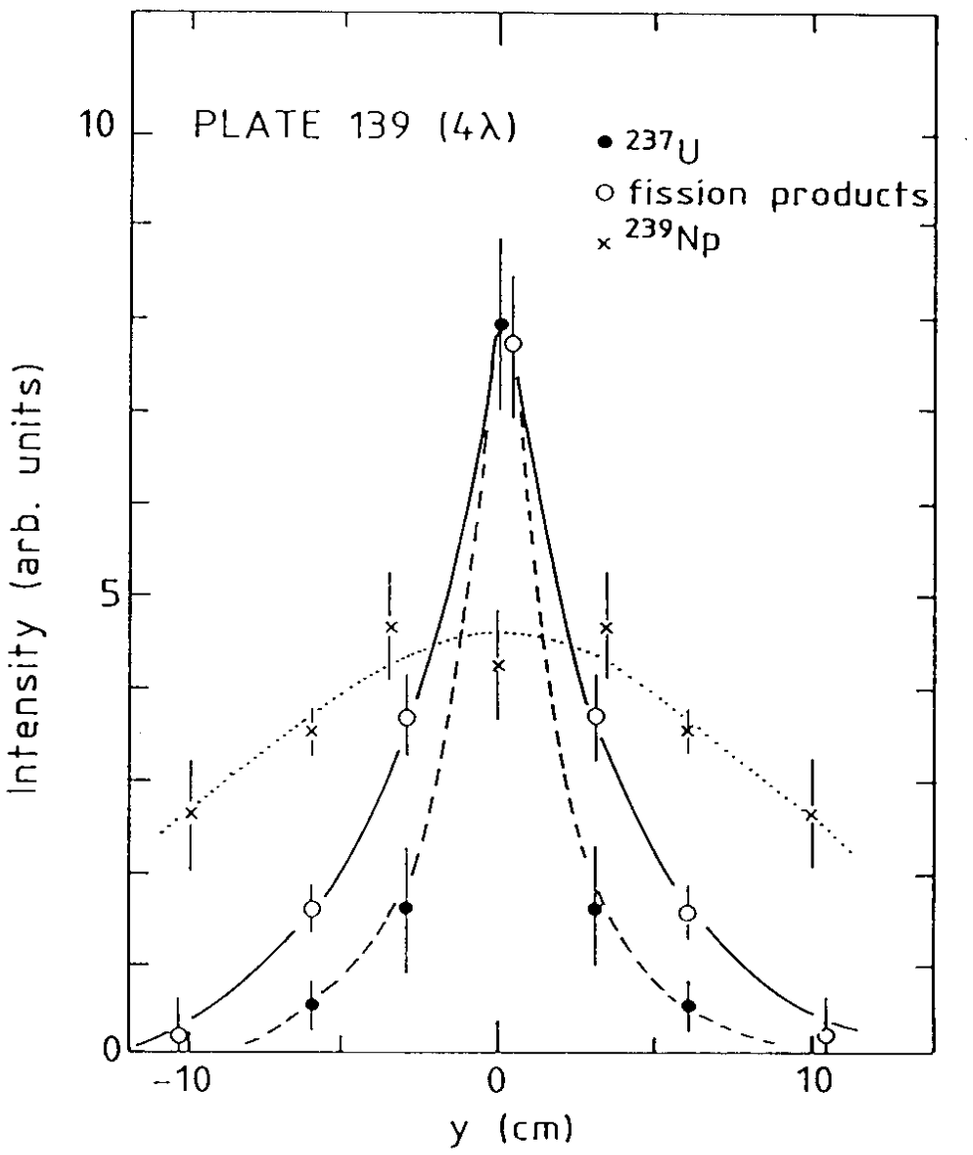
PLATE 139 (4λ)
• ^{237}U
○ fission products
× ^{239}Np
Intensity (arb. units)
y (cm)

Fig. 6

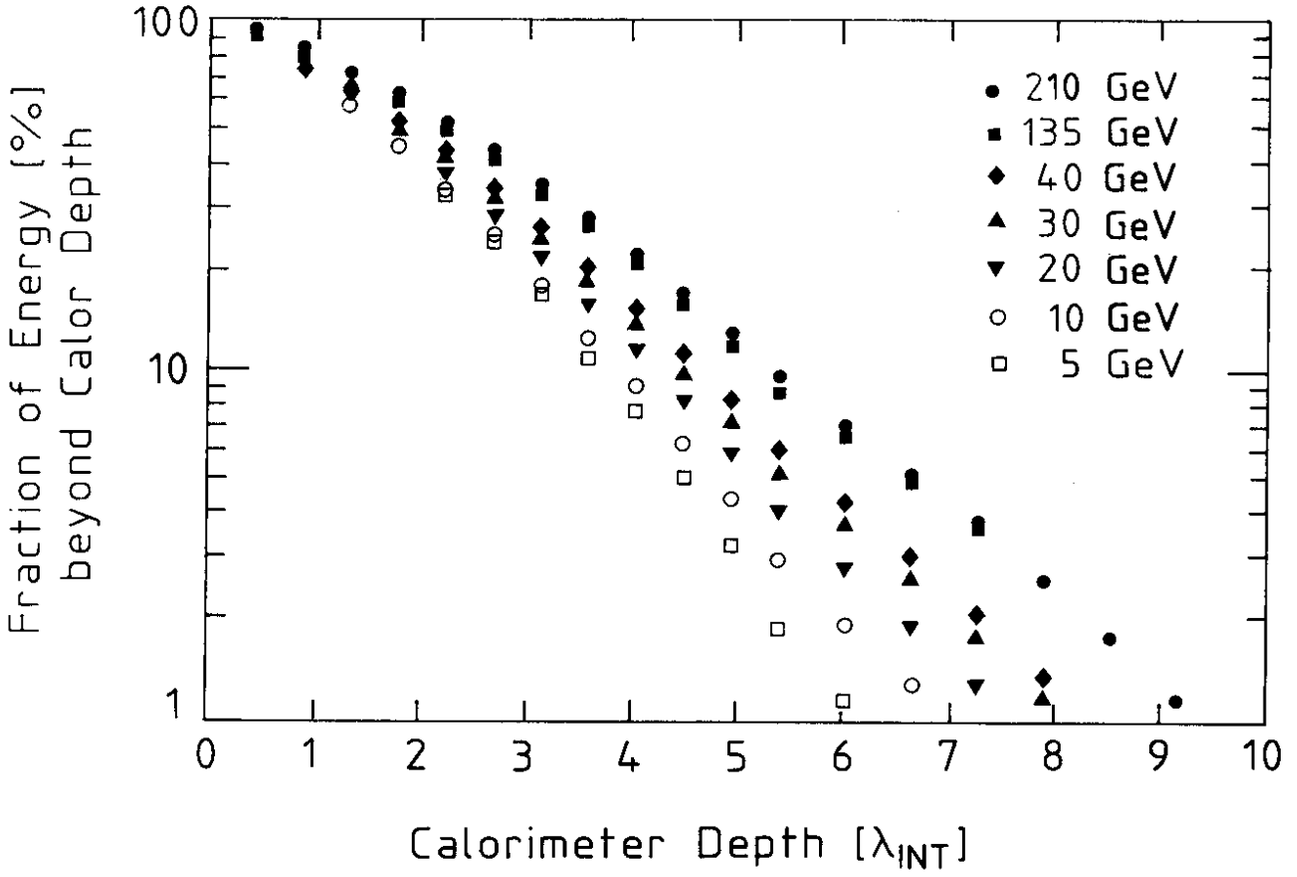
100
10
1
Fraction of Energy [%]
beyond Calor Depth
210 GeV
135 GeV
40 GeV
30 GeV
20 GeV
10 GeV
5 GeV
0 1 2 3 4 5 6 7 8 9 10
Calorimeter Depth [λINT]

Fig. 7

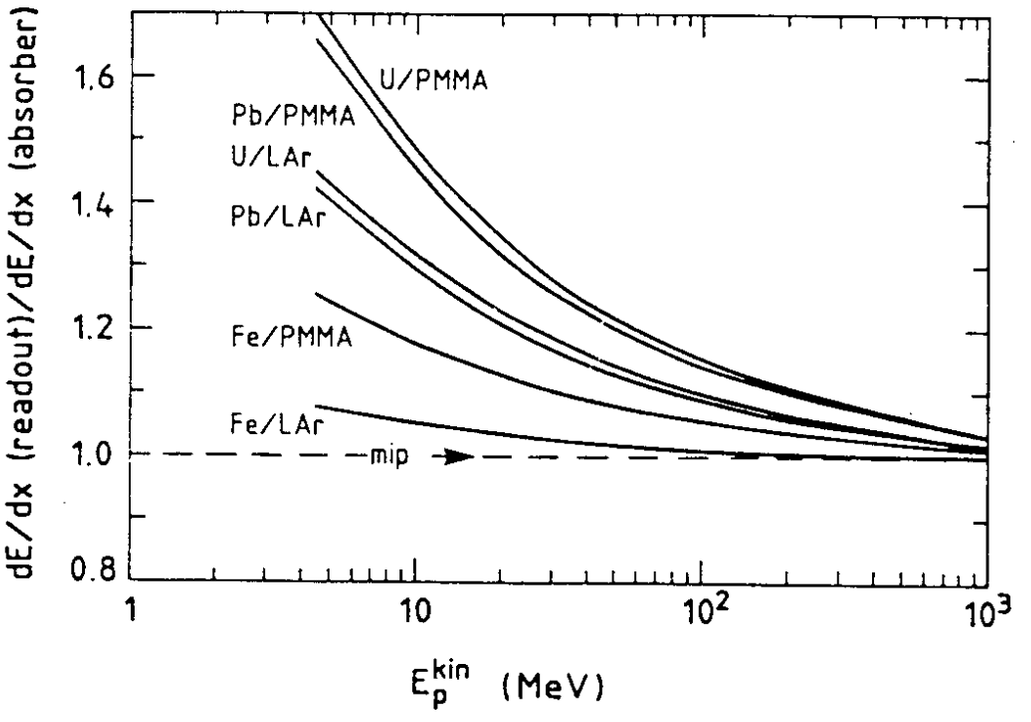
dE/dx (readout)/dE/dx (absorber)
1.6
1.4
1.2
1.0
0.8
U/PMMA
Pb/PMMA
U/LAr
Pb/LAr
Fe/PMMA
Fe/LAr
mip
1
10
10²
10³
E_p^kin (MeV)

Fig. 8

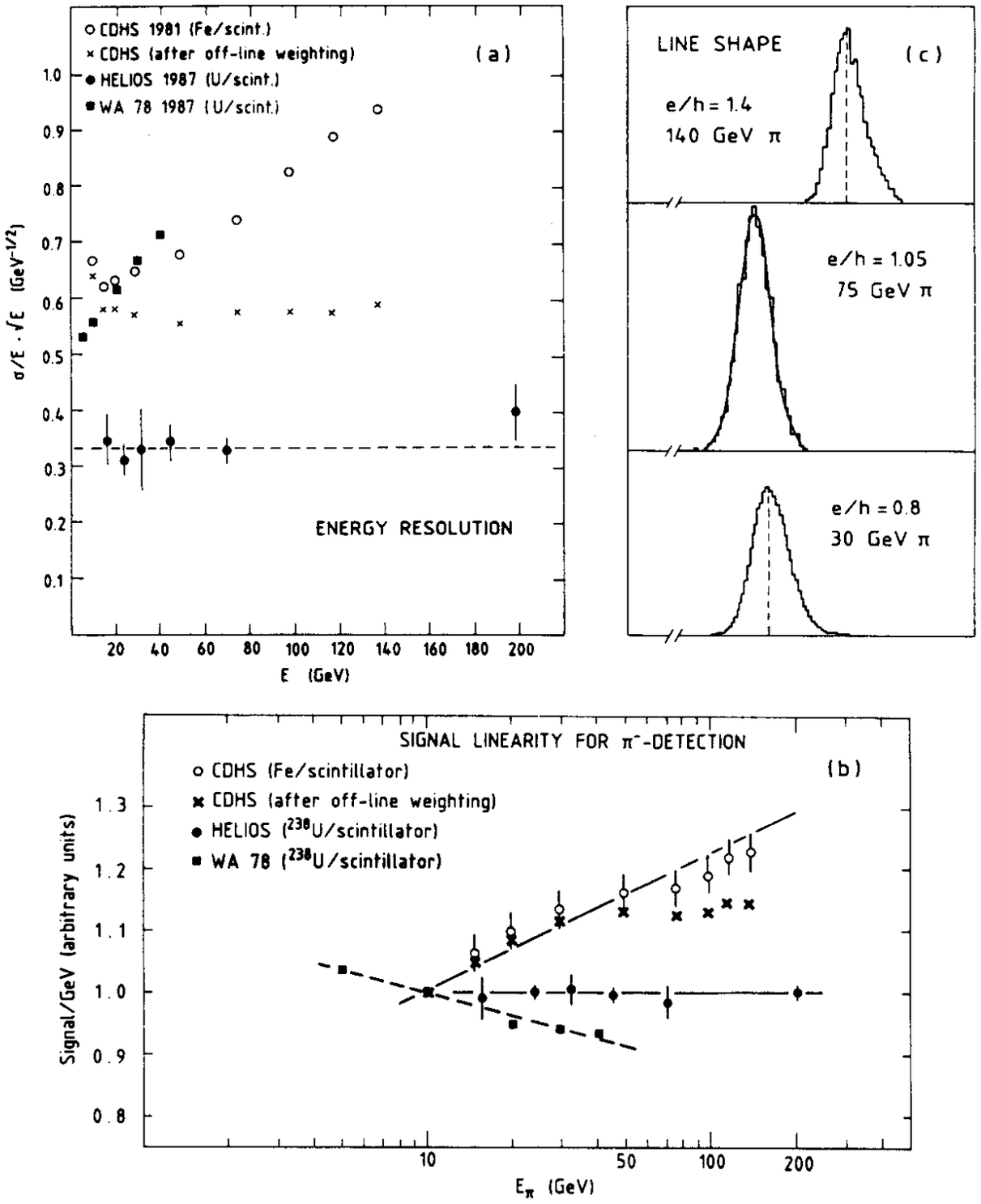
CDHS 1981 (Fe/scint.)
CDHS (after off-line weighting)
HELIOS 1987 (U/scint.)
WA 78 1987 (U/scint.)
(a)
ENERGY RESOLUTION
σ/E · √E (GeV^-1/2)
E (GeV)
LINE SHAPE
(c)
e/h = 1.4
140 GeV π
e/h = 1.05
75 GeV π
e/h = 0.8
30 GeV π
SIGNAL LINEARITY FOR π⁻-DETECTION
(b)
CDHS (Fe/scintillator)
CDHS (after off-line weighting)
HELIOS (238U/scintillator)
WA 78 (238U/scintillator)
Signal/GeV (arbitrary units)
Eπ (GeV)

Fig. 9

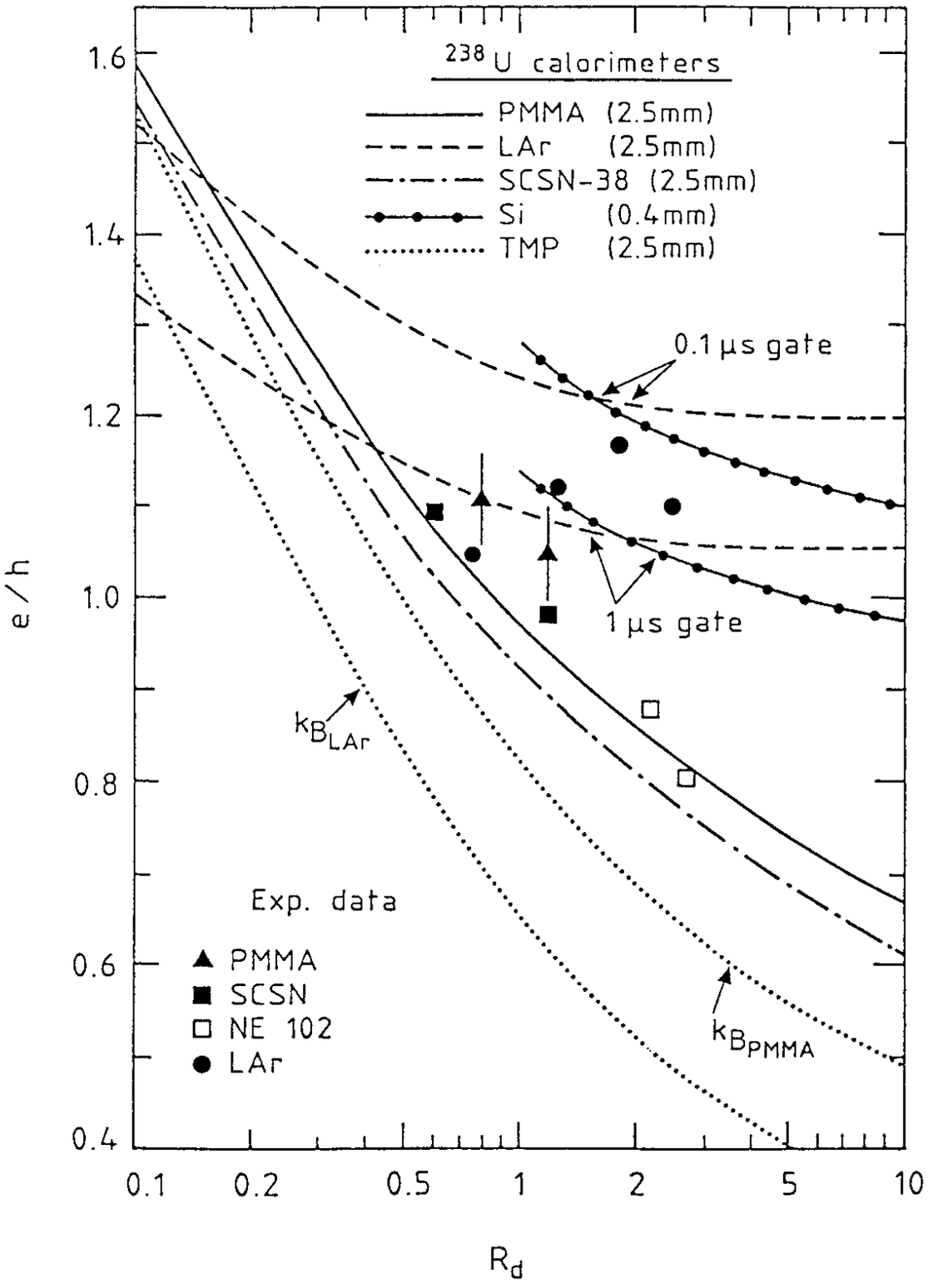
^{238}U calorimeters
PMMA (2.5mm)
LAr (2.5mm)
SCSN-38 (2.5mm)
Si (0.4mm)
TMP (2.5mm)
0.1 µs gate
1 µs gate
kB_{LAr}
kB_{PMMA}
Exp. data
PMMA
SCSN
NE 102
LAr
e / h
R_d
1.6
1.4
1.2
1.0
0.8
0.6
0.4
0.1
0.2
0.5
1
2
5
10

Fig. 10

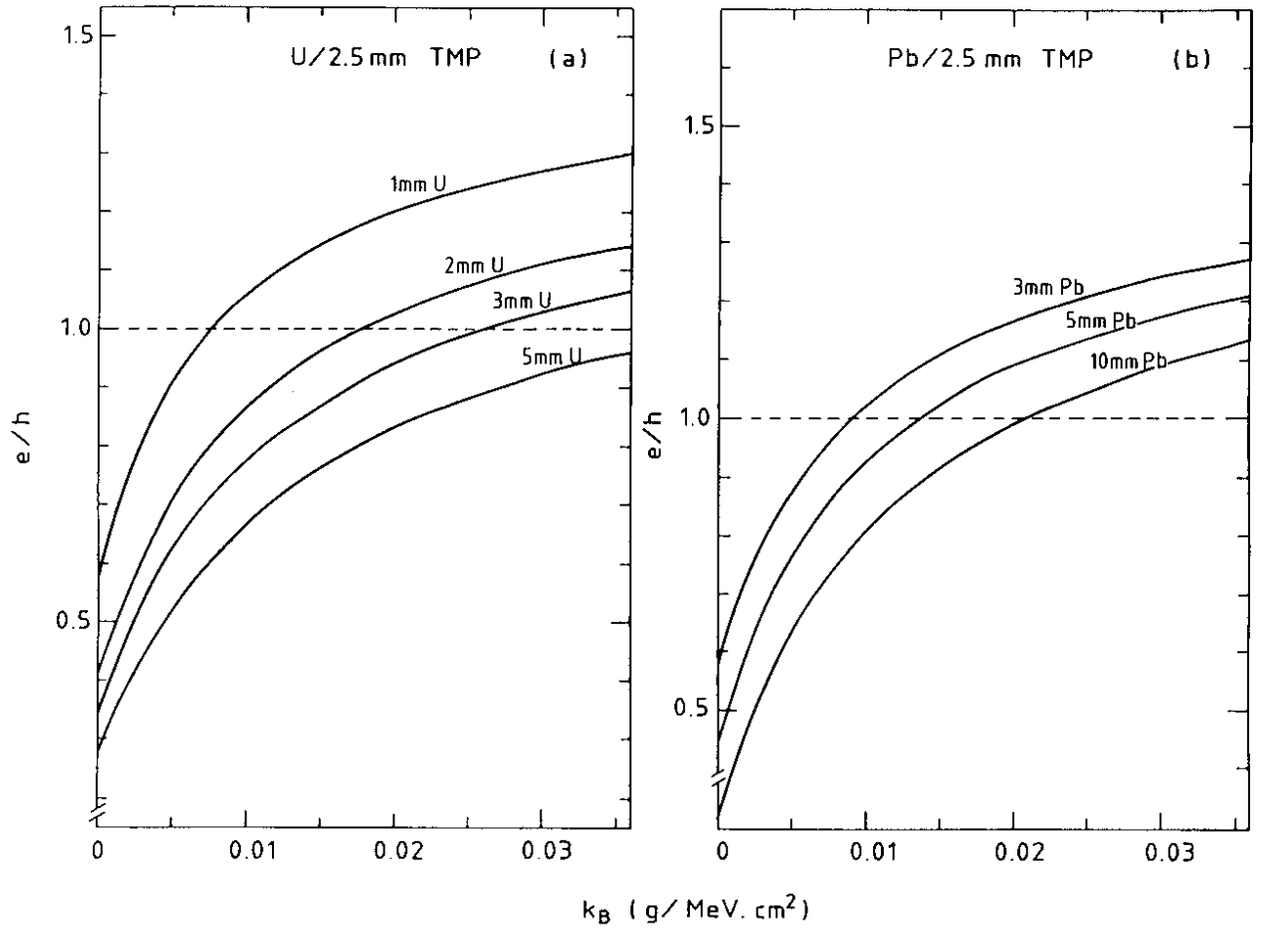
U/2.5mm TMP (a)
Pb/2.5 mm TMP (b)
1mm U
2mm U
3mm U
5mm U
3mm Pb
5mm Pb
10mm Pb
e/h
1.5
1.0
0.5
0
0.01
0.02
0.03
k_B (g/ MeV. cm^2)

Fig. 11

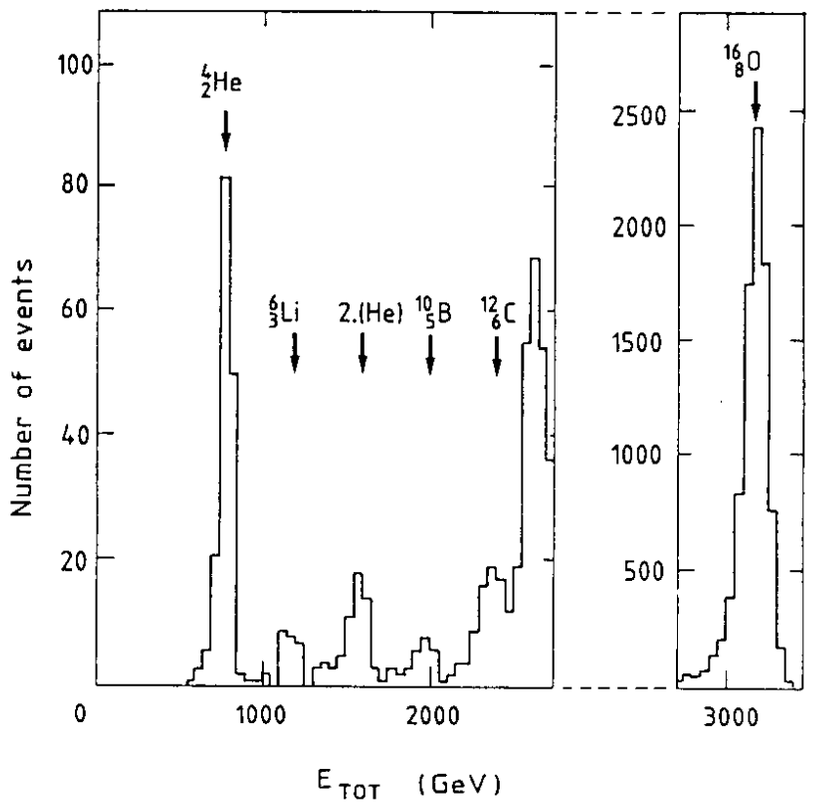
$^4_2$He
$^6_3$Li
2.(He)
$^{10}_5$B
$^{12}_6$C
$^{16}_8$O
Number of events
100
80
60
40
20
2500
2000
1500
1000
500
0
1000
2000
3000
E_{TOT} (GeV)

Fig. 12

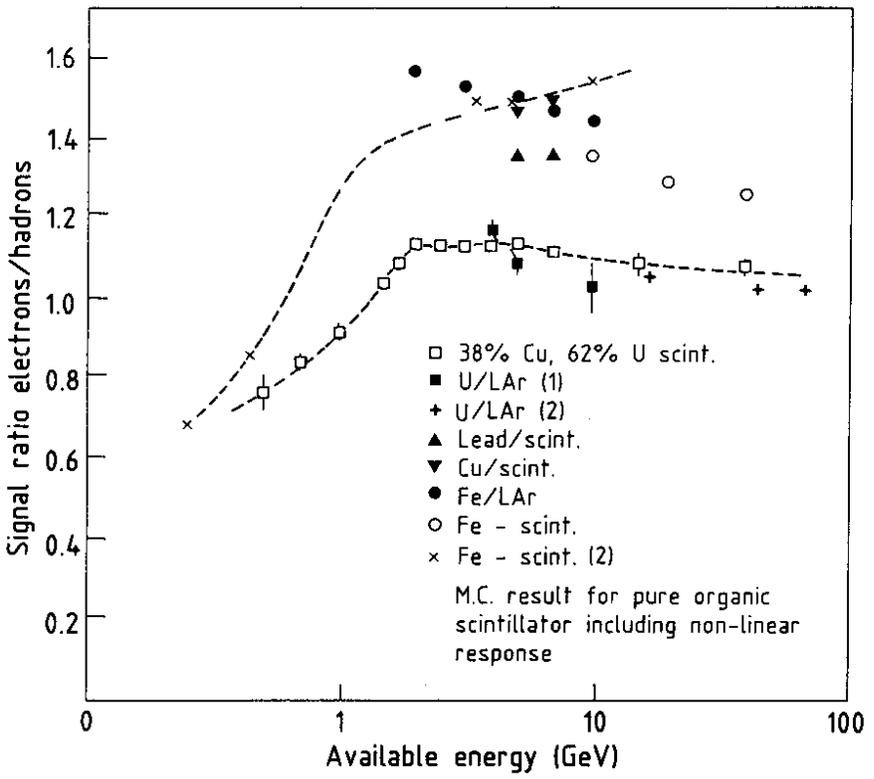
Signal ratio electrons/hadrons
1.6
1.4
1.2
1.0
0.8
0.6
0.4
0.2
0
1
10
100
Available energy (GeV)
38% Cu, 62% U scint.
U/LAr (1)
U/LAr (2)
Lead/scint.
Cu/scint.
Fe/LAr
Fe - scint.
Fe - scint. (2)
M.C. result for pure organic scintillator including non-linear response

Fig. 13

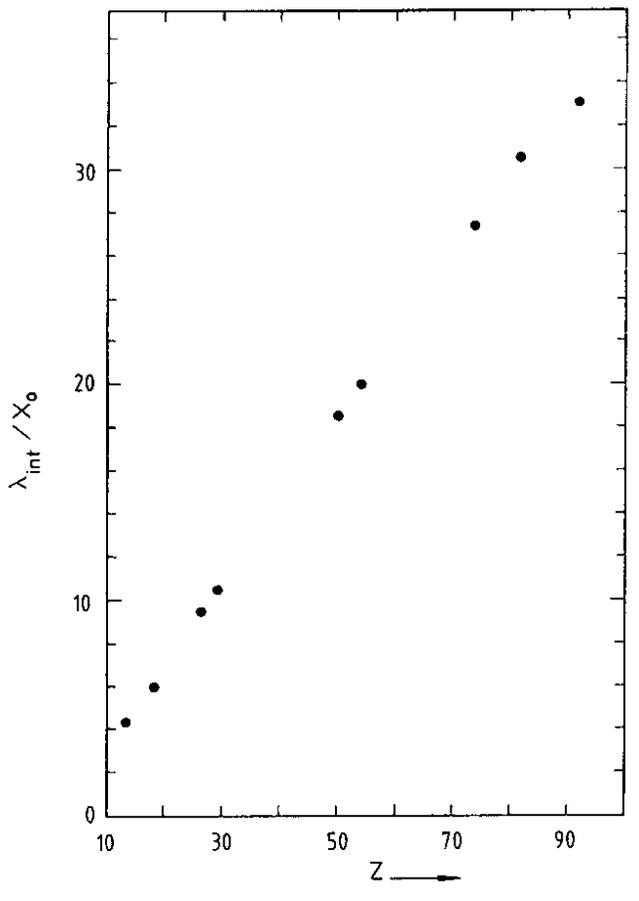
λ_{int} / X_o
30
20
10
0
10
30
50
70
90
Z

Fig. 14

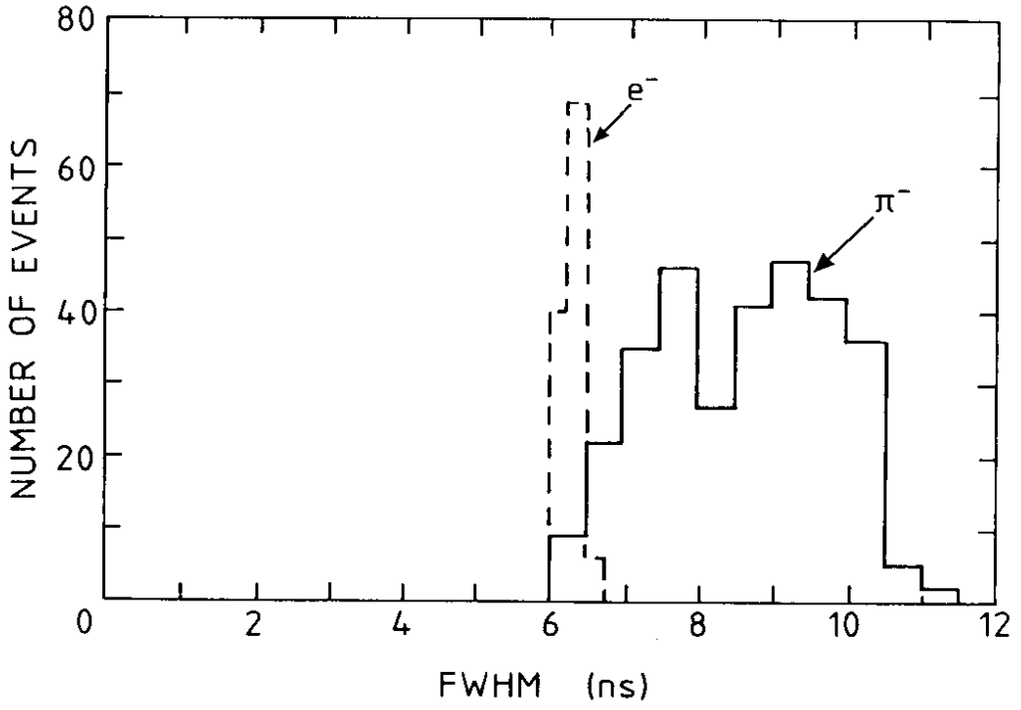
NUMBER OF EVENTS
80
60
40
20
0
2
4
6
8
10
12
FWHM (ns)
e⁻
π⁻

Fig. 15

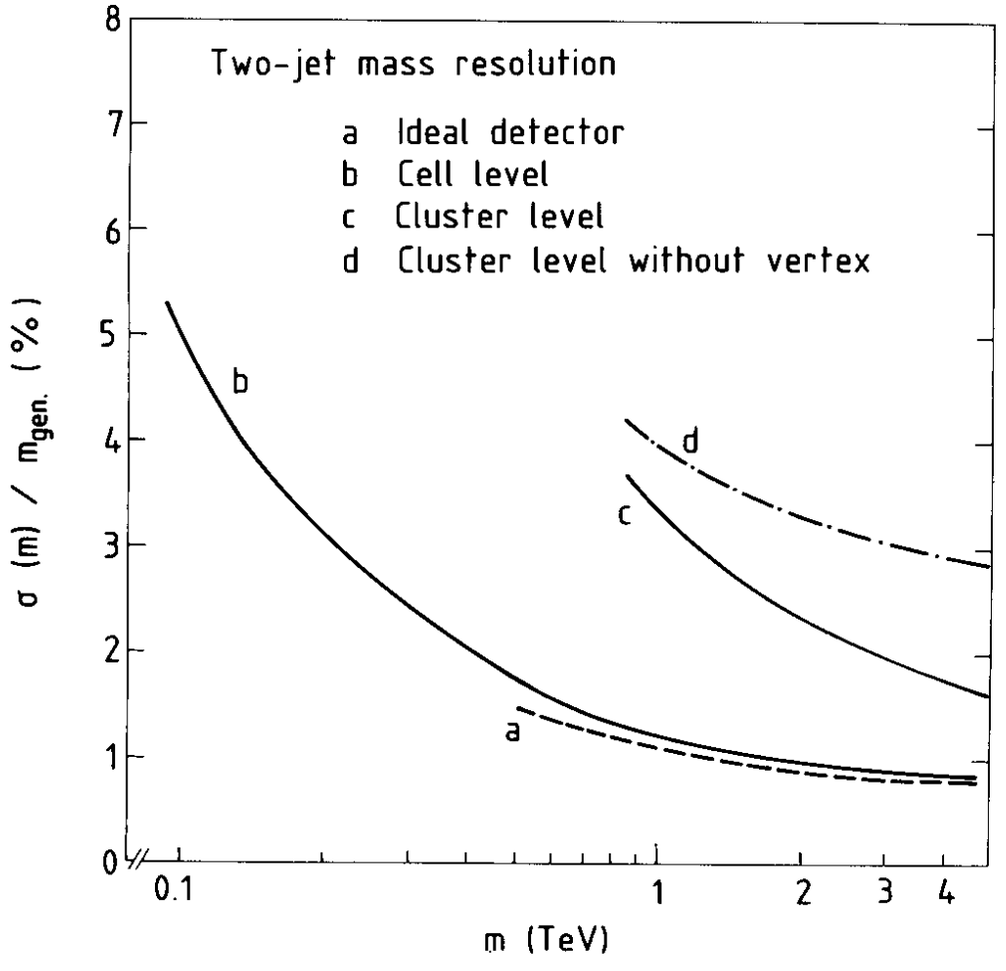
Two-jet mass resolution
a Ideal detector
b Cell level
c Cluster level
d Cluster level without vertex
σ (m) / m_gen. (%)
8
7
6
5
4
3
2
1
0
0.1
1
2
3
4
m (TeV)
a
b
c
d

Fig. 16

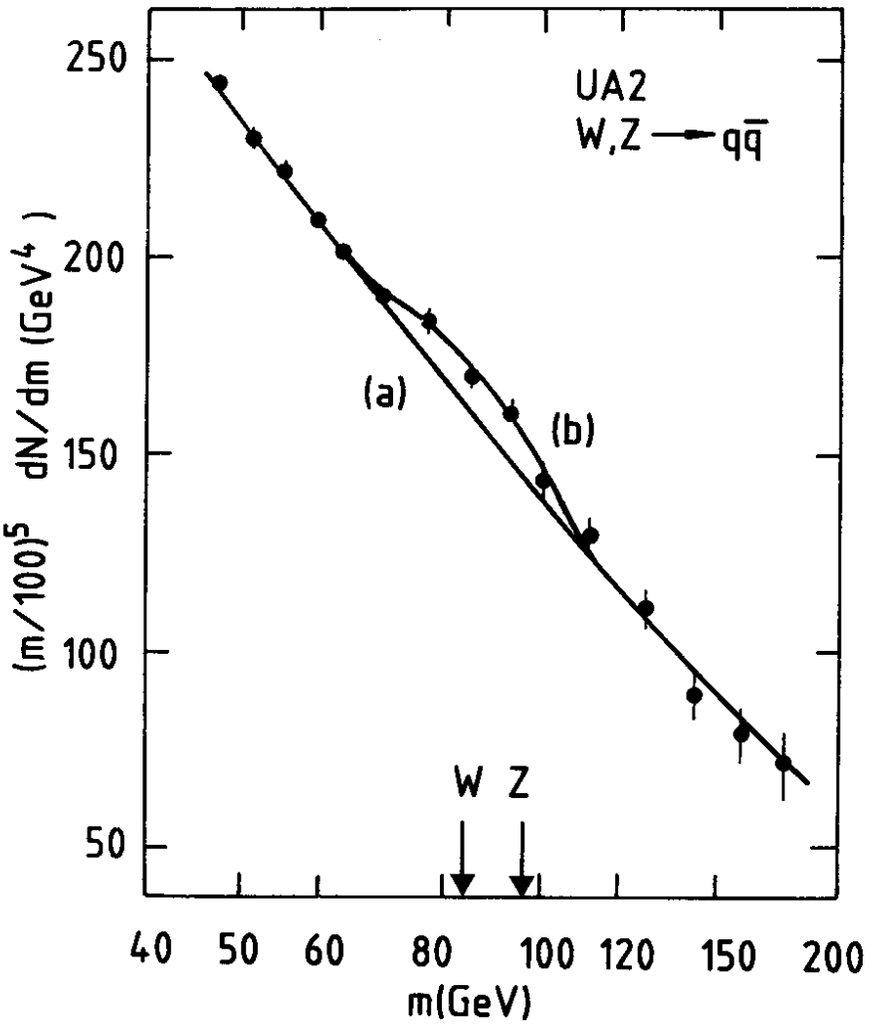
UA2
W,Z → qq̄
(a)
(b)
W Z
250
200
150
100
50
40 50 60 80 100 120 150 200
m(GeV)
(m/100)^5 dN/dm (GeV^4)

Fig. 17

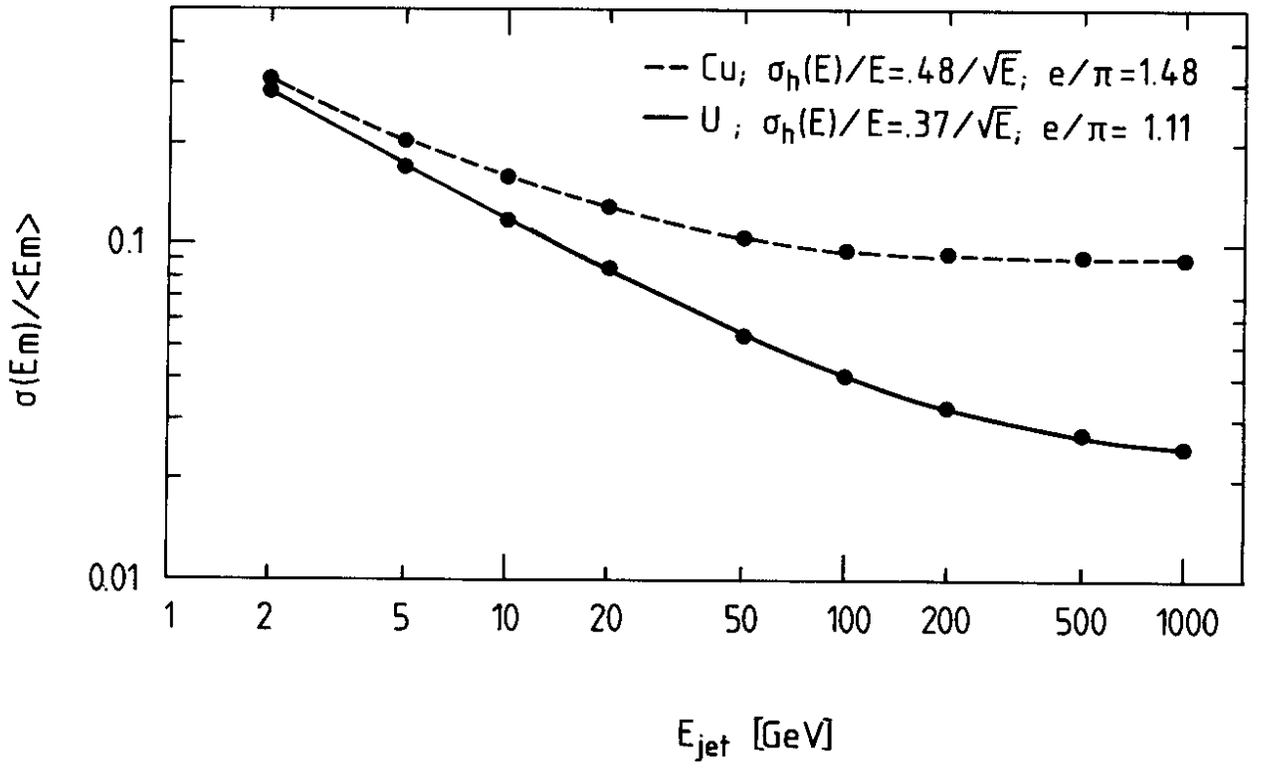
Cu; σh(E)/E=.48/√E; e/π=1.48
U ; σh(E)/E=.37/√E; e/π= 1.11
0.1
0.01
1 2 5 10 20 50 100 200 500 1000
σ(Em)/<Em>
Ejet [GeV]

Fig. 18

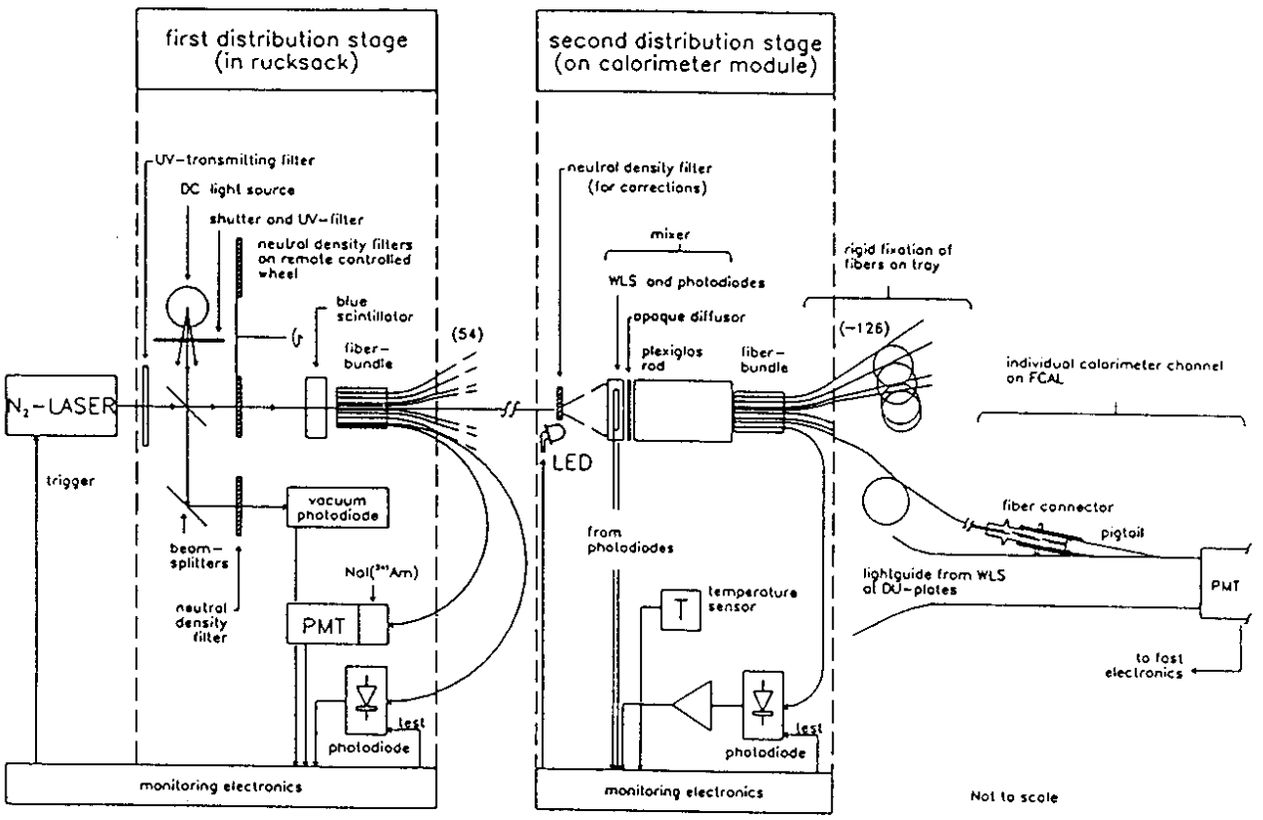
first distribution stage
(in rucksack)
second distribution stage
(on calorimeter module)
UV-transmitting filter
DC light source
shutter and UV-filter
neutral density filters
on remote controlled
wheel
blue
scintillator
fiber-
bundle
(54)
N2-LASER
trigger
vacuum
photodiode
beam-
splitters
neutral
density
filter
NaI(241Am)
PMT
test
photodiode
monitoring electronics
neutral density filter
(for corrections)
mixer
WLS and photodiodes
opaque diffusor
plexiglas
rod
fiber-
bundle
LED
from
photodiodes
temperature
sensor
test
photodiode
monitoring electronics
rigid fixation of
fibers on tray
(-126)
individual calorimeter channel
on FCAL
fiber connector
pigtail
lightguide from WLS
of DU-plates
PMT
to fast
electronics
Not to scale

Fig. 19

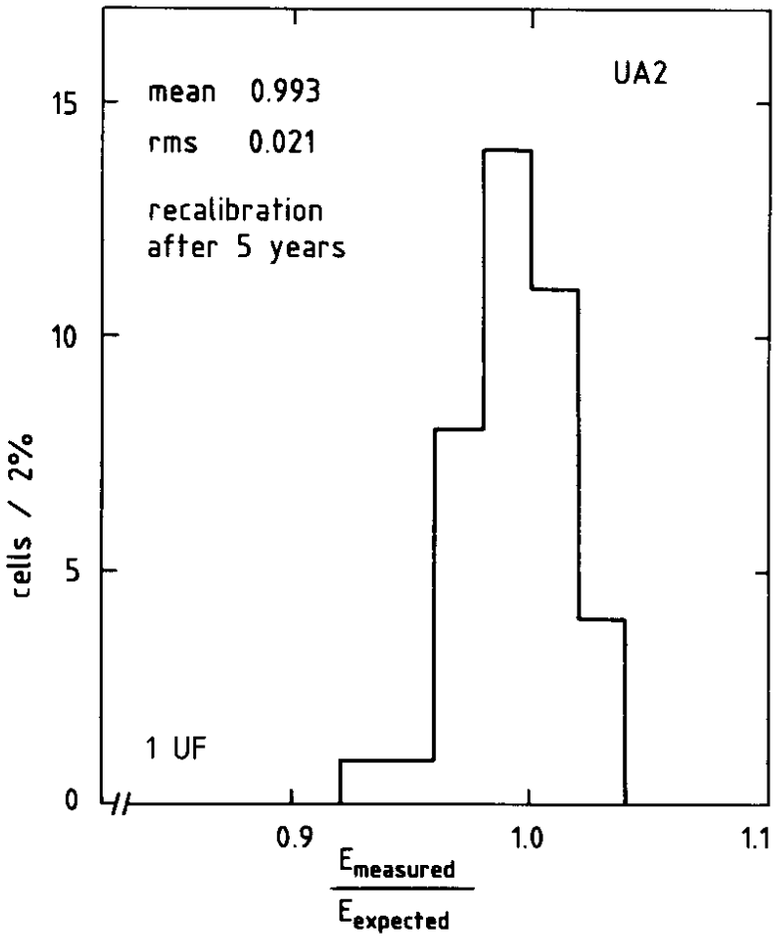
UA2
mean 0.993
rms 0.021
recalibration
after 5 years
1 UF
cells / 2%
15
10
5
0
0.9
1.0
1.1
Emeasured
Eexpected

Fig. 20

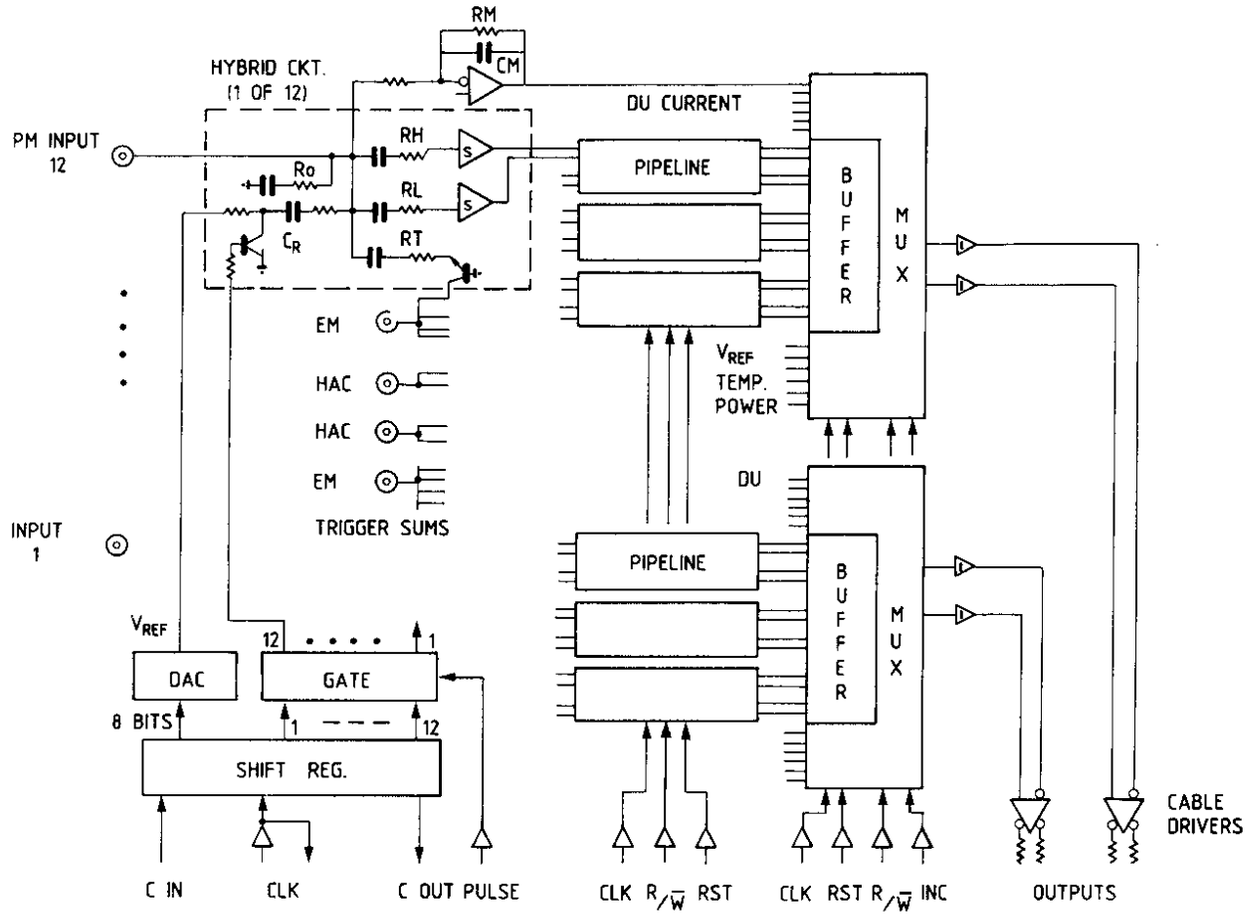
RM
CM
HYBRID CKT.
(1 OF 12)
DU CURRENT
PM INPUT
12
RH
RL
RT
Ro
C_R
PIPELINE
BUFFER
MUX
EM
HAC
HAC
EM
TRIGGER SUMS
V_{REF}
TEMP.
POWER
DU
INPUT
1
PIPELINE
BUFFER
MUX
V_{REF}
12
1
DAC
GATE
8 BITS
1
12
SHIFT REG.
CABLE
DRIVERS
C IN
CLK
C OUT PULSE
CLK $R/\overline{W}$ RST
CLK RST $R/\overline{W}$ INC
OUTPUTS

Fig. 21

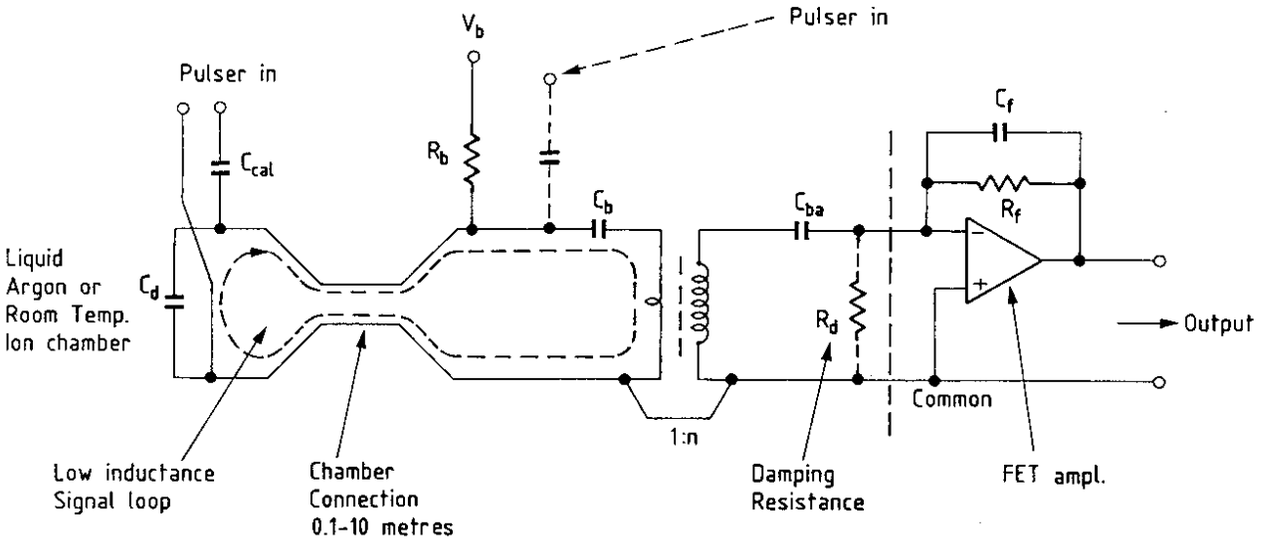
V_b
Pulser in
Pulser in
C_{cal}
R_b
C_b
C_{ba}
C_f
R_f
Liquid
Argon or
Room Temp.
Ion chamber
C_d
R_d
Output
Common
1:n
Low inductance
Signal loop
Chamber
Connection
0.1-10 metres
Damping
Resistance
FET ampl.

Fig. 22

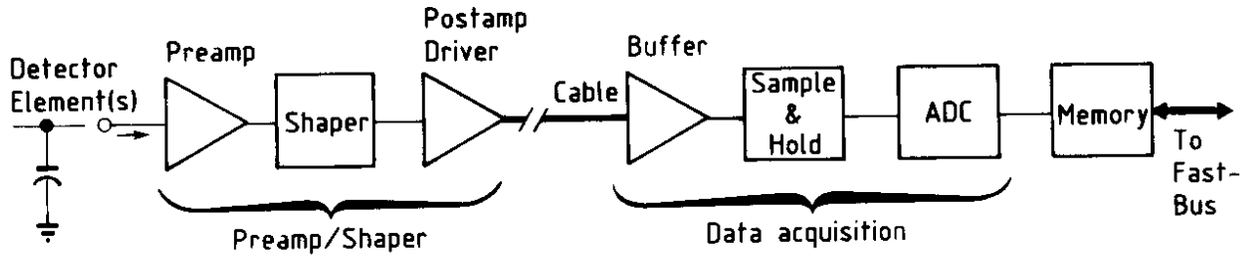
Detector
Element(s)
Preamp
Shaper
Postamp
Driver
Cable
Buffer
Sample
&
Hold
ADC
Memory
To
Fast-
Bus
Preamp/Shaper
Data acquisition

Fig. 23

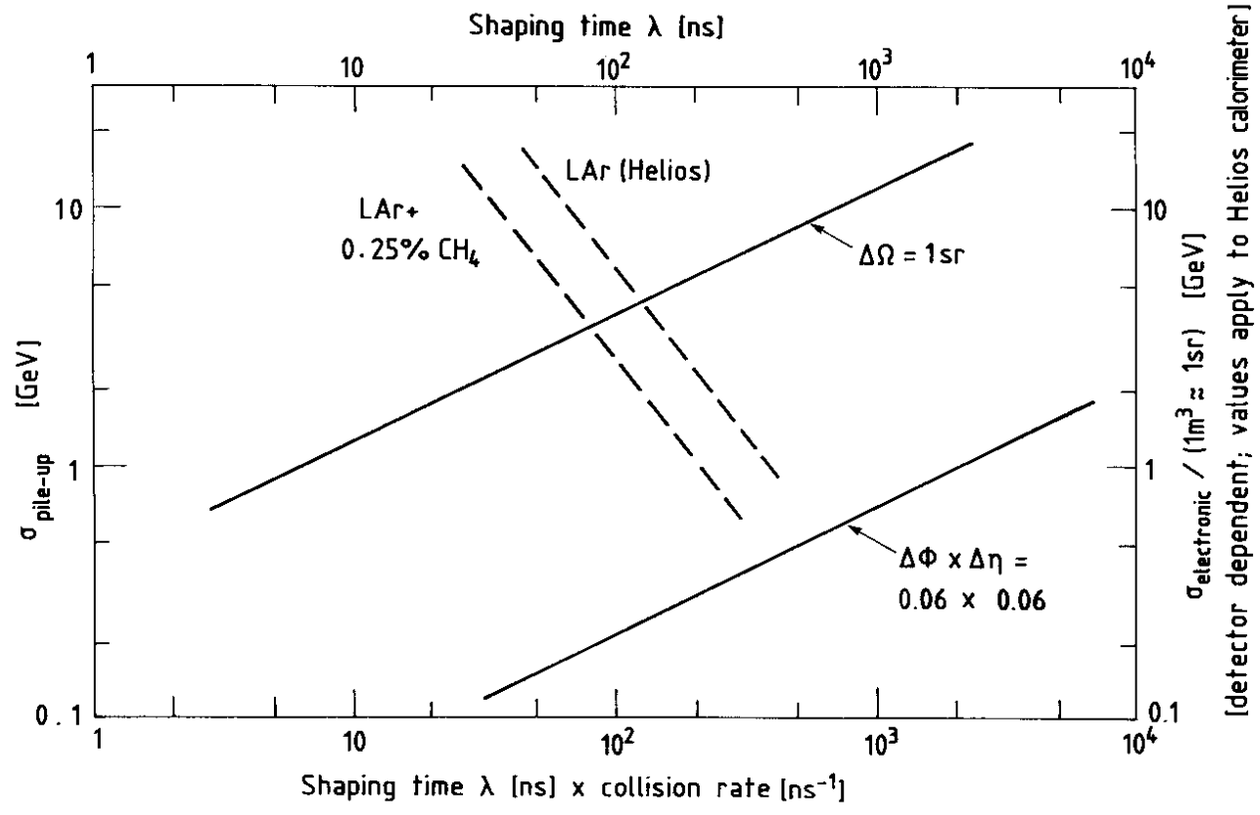
Shaping time λ [ns]
1
10
10²
10³
10⁴
LAr (Helios)
LAr+
0.25% CH₄
ΔΩ = 1sr
ΔΦ x Δη =
0.06 x 0.06
σ pile-up [GeV]
σ electronic / (1m³ ≈ 1sr) [GeV]
[detector dependent; values apply to Helios calorimeter]
0.1
Shaping time λ [ns] x collision rate [ns⁻¹]

Fig. 24

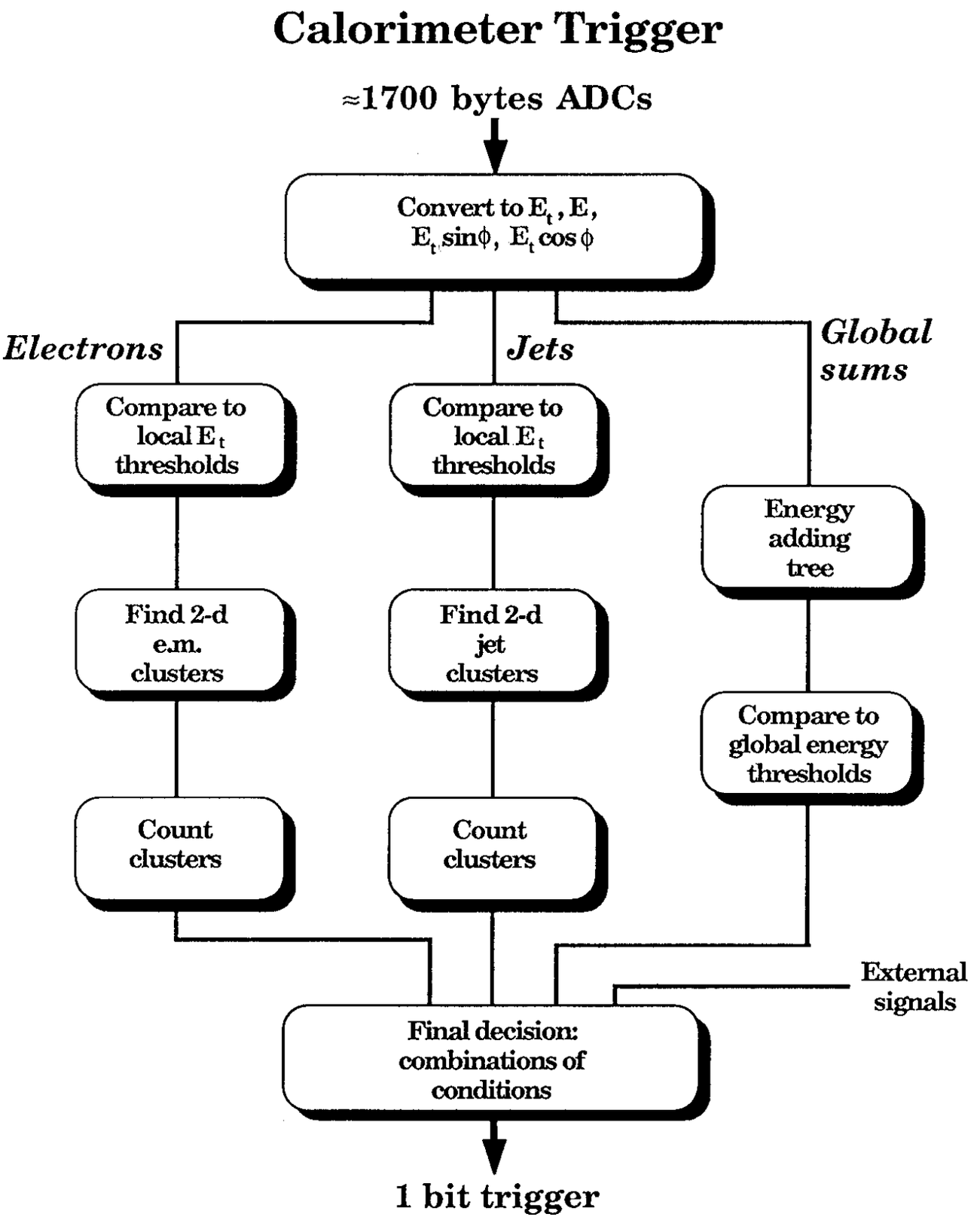
Calorimeter Trigger
≈1700 bytes ADCs
Convert to E_t, E, $E_t \sin\phi$, $E_t \cos\phi$
Electrons
Jets
Global sums
Compare to local E_t thresholds
Compare to local E_t thresholds
Energy adding tree
Find 2-d e.m. clusters
Find 2-d jet clusters
Compare to global energy thresholds
Count clusters
Count clusters
External signals
Final decision: combinations of conditions
1 bit trigger

Fig. 25

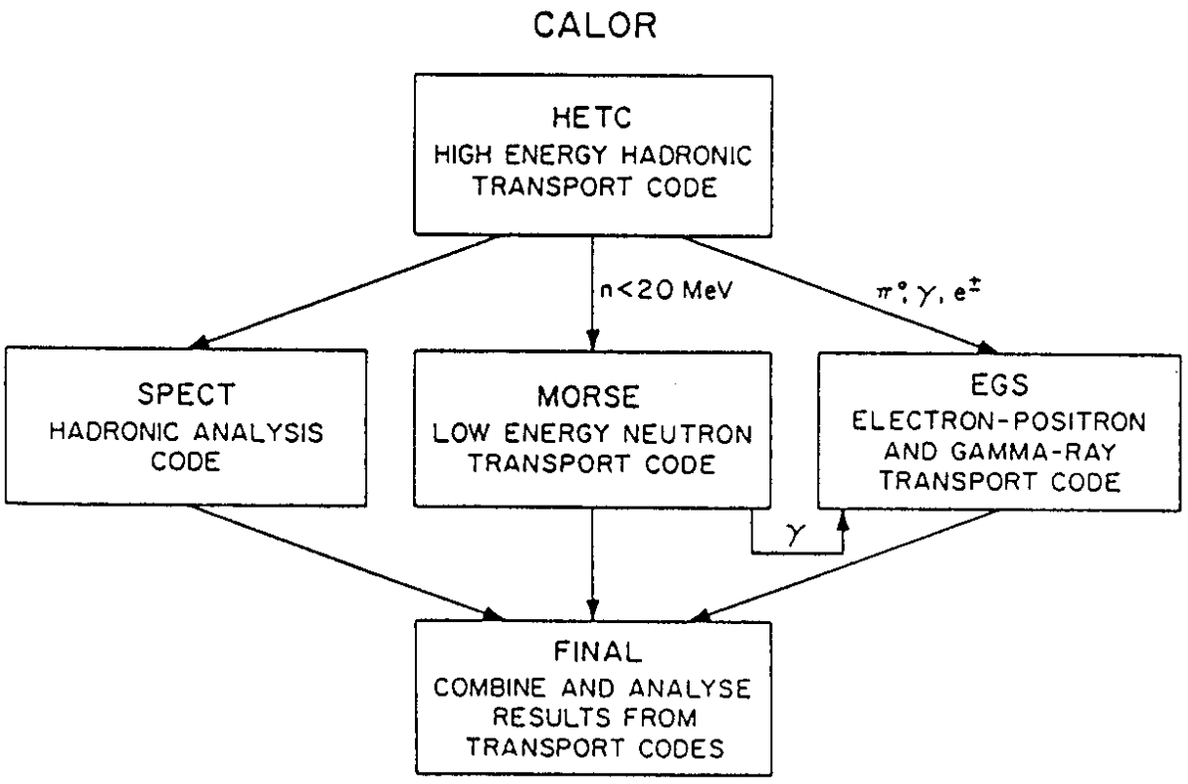
CALOR
HETC
HIGH ENERGY HADRONIC TRANSPORT CODE
n<20 MeV
π°, γ, e±
SPECT
HADRONIC ANALYSIS CODE
MORSE
LOW ENERGY NEUTRON TRANSPORT CODE
EGS
ELECTRON-POSITRON AND GAMMA-RAY TRANSPORT CODE
γ
FINAL
COMBINE AND ANALYSE RESULTS FROM TRANSPORT CODES

Fig. 26

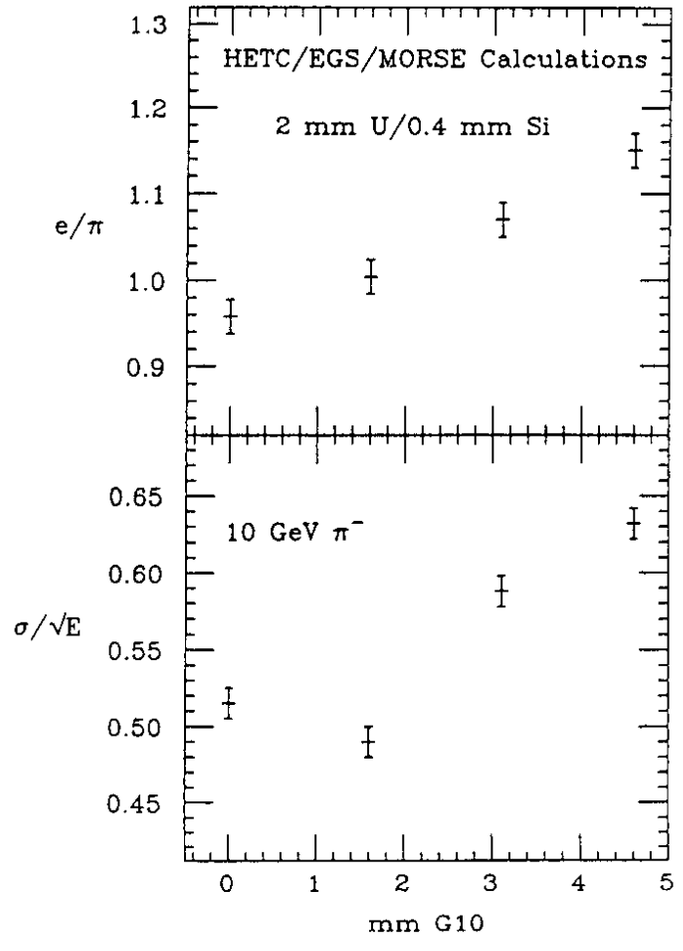
HETC/EGS/MORSE Calculations
2 mm U/0.4 mm Si
e/π
1.3
1.2
1.1
1.0
0.9
10 GeV π⁻
σ/√E
0.65
0.60
0.55
0.50
0.45
0
1
2
3
4
5
mm G10

Fig. 27

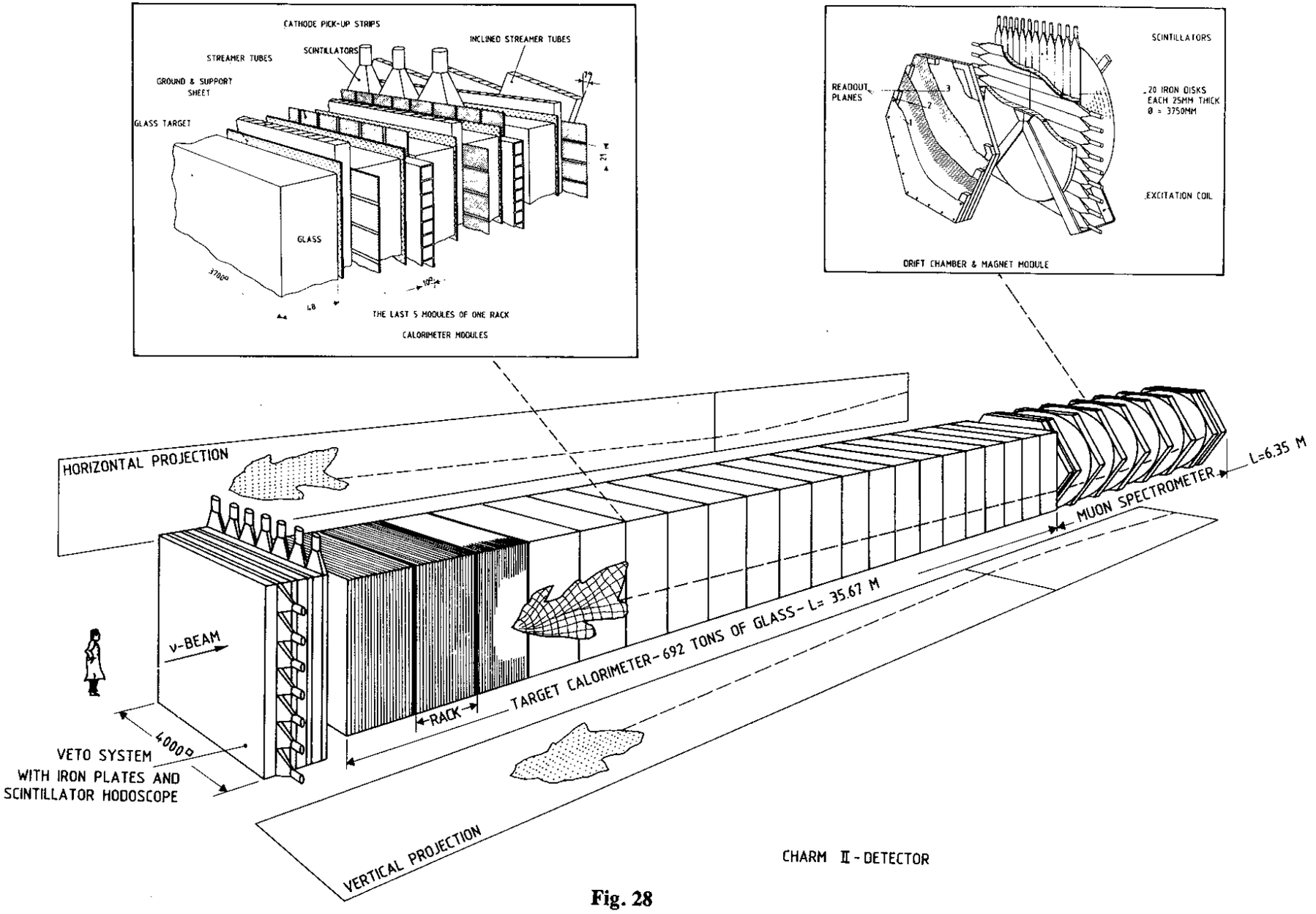
CATHODE PICK-UP STRIPS
INCLINED STREAMER TUBES
SCINTILLATORS
STREAMER TUBES
GROUND & SUPPORT SHEET
GLASS TARGET
GLASS
THE LAST 5 MODULES OF ONE RACK
CALORIMETER MODULES
SCINTILLATORS
READOUT PLANES
20 IRON DISKS EACH 25MM THICK
EXCITATION COIL
DRIFT CHAMBER & MAGNET MODULE
HORIZONTAL PROJECTION
L=6.35 M
MUON SPECTROMETER
TARGET CALORIMETER - 692 TONS OF GLASS - L= 35.67 M
RACK
ν-BEAM
VETO SYSTEM WITH IRON PLATES AND SCINTILLATOR HODOSCOPE
VERTICAL PROJECTION
CHARM II - DETECTOR

Fig. 28

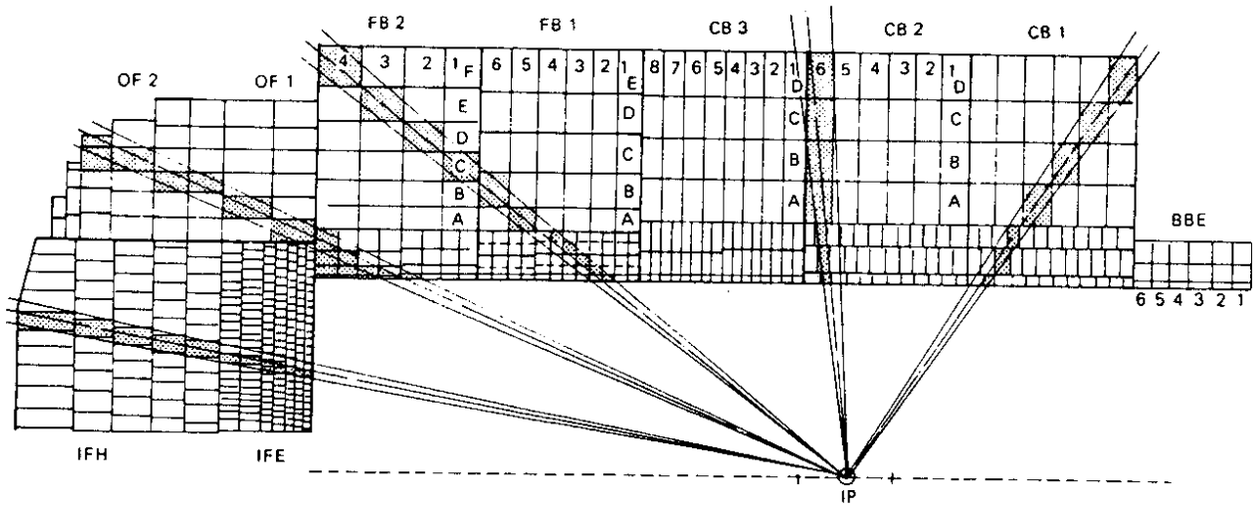

Fig. 29